Search for CP Violation in τ Decays at *BABAR*

by

Hervé Hiu Fai Choi
B.Sc., University of Toronto, 2005

A Dissertation Submitted in Partial Fulfillment of the
Requirements for the Degree of

DOCTOR OF PHILOSOPHY

in the Department of Physics and Astronomy

Search for CP Violation in τ Decays at *BABAR*

by

Hervé Hiu Fai Choi
B.Sc., University of Toronto, 2005

Supervisory Committee

Dr. R. Sobie, Supervisor
(Department of Physics and Astronomy)

Dr. M. Lefebvre, Departmental Member
(Department of Physics and Astronomy)

Dr. R. Kowalewski, Departmental Member
(Department of Physics and Astronomy)

Dr. A. Weaver, Outside Member
(School of Earth and Ocean Sciences)

Supervisory Committee

Dr. R. Sobie, Supervisor
(Department of Physics and Astronomy)

Dr. M. Lefebvre, Departmental Member
(Department of Physics and Astronomy)

Dr. R. Kowalewski, Departmental Member
(Department of Physics and Astronomy)

Dr. A. Weaver, Outside Member
(School of Earth and Ocean Sciences)

ABSTRACT

According to the Big Bang Theory, matter and antimatter were produced in equal amounts at the beginning. Over time the antimatter disappeared, leaving galactic structures composed only of matter. Therefore, there is some process in nature that proceeds at different rates for matter and antimatter due to the violation of the *CP* symmetry. *CP* violation has been observed in strange and bottom quark meson decays. However, a direct *CP* violation is predicted in the τ lepton sector. Specifically, the charge asymmetry due to *CP* violation in the decay $\tau^- \to \pi^- K^0_S (\geq 0\pi^0)\, \nu_\tau$ is predicted to be $(+0.33 \pm 0.01)\%$. In this work the charge asymmetry of the decay $\tau^- \to \pi^- K^0_S (\geq 0\pi^0)\, \nu_\tau$ is measured using a dataset of 437 million τ lepton pairs collected by the *BABAR* experiment at the SLAC National Accelerator Laboratory. The charge asymmetry induced by *CP* violation is found to be $A_Q = (-0.45 \pm 0.24 \pm 0.11)\,\%$, consistent with prediction.

Contents

List of Tables

List of Figures

ACKNOWLEDGEMENTS

Firstly, I would like to thank my supervisor, Prof. Randall Sobie, for his seemingly unlimited patience with me. It appears that no question can be too stupid, and I can always knock on his door to ask for guidance. Randy always seems to be able to explain the most complicated problem in the clearest way, and for multiple times if necessary. His experience comes through when we need to foresee the challenges and the most direct way of surmounting them. I am forever grateful for his laid-back yet effective mentorship.

I would also like to thank the fellow graduate students with whom I have had the fortune of working alongside, as our rapport makes my life as a graduate student much more enjoyable than otherwise. We have worked together in different capacities, be it course work or research, but they all have always been able to give me valuable advice as peers. In addition to the peers, the faculty members here in the Department are all ready to give advice and let me benefit from their experience and wisdom. They have nurtured great minds in the past, and I hope to continue that tradition, to be able to make them proud as I embark upon a new stage in my life. A special thank-you goes to Prof. Michel Lefebvre, Prof. Robert Kowalewski, Prof. Michael Roney and Prof. Andrew Weaver for their guidance.

Further, I would like to thank my friends and my family for their encouragement, support and understanding. The studies have not always been easy, but their kind words have given me the motivation I need to keep going. Mabel has been waiting for me on the other side of the planet, and today I can finally say that we can be on the same continent and spend some time together!

Lastly, I would like to give my thanks to God for His providence and for the opportunity to carry on my studies. I have always found it fascinating of how nature works. Even though what I have learned is merely scratching the surface, I have had a brief glimpse of the marvel of His creation.

"When I consider Your heavens,
the work of Your fingers,
the moon and the stars,
which you have set in place,
what is man that You are mindful of him,
the son of man that You care for him?"
Psalm 8:3-4 (NIV)

DEDICATION

Dedicated to my parents and Mabel
for their continuous support

你們無間的關懷、勗厲、代禱
是我孜孜不倦的原動力

Chapter 1

Introduction

1.1 Antimatter and CP Violation

At the time of the Big Bang, the Universe was filled with energy. The energy converted into equal amounts of matter and antimatter[1] in a process known as pair production. The highly energetic matter and antimatter particles either interacted with other particles or decayed to produce particles with lower mass. As the Universe expanded, the energy of the individual photons in the Universe decreased[2]. At some point in time they were no longer energetic enough to produce any new particle-antiparticle pairs, as limited by Einstein's mass-energy equivalence relation $E = mc^2$. After this "freeze-out" point, the number of unstable, higher-mass particles could only decrease as they decayed to stable particles – the protons, neutrons and electrons we observe today.

Fig. 1.1 shows the evolution of the Universe after the Big Bang. Photons can only convert into particle-antiparticle pairs, so matter and antimatter were created in equal amounts at the beginning. The subsequent decays, however, somehow differentiated between matter and antimatter, resulting in an excess of matter over antimatter. The antimatter then annihilated with the surrounding matter, resulting in its disappearance at $\sim$1 second after the Big Bang. Presently, there is no evidence for any galactic structures composed of antimatter (see, for example, [2]), and understanding the fundamental differences between matter and antimatter

[1] Antimatter is the *doppelgänger* of matter: an anti-particle has the same mass and spin as its corresponding particle, but its charge and other internal quantum numbers are the opposite.

[2] The wavelength of the photon was stretched along with the expansion of spacetime in the Universe. See, for example, [2].

is crucial in deriving a complete picture of the evolution of the Universe.

The vast majority of the visible matter today is composed of baryons, which are particles composed of three quarks (see Sec. 1.2 for a brief description of quarks). Protons and neutrons are examples of baryons. It is important we understand the generation of baryons (baryogenesis) from the photons in the radiation-dominated epoch of the Universe as it can help explain the existence of the observed stellar structures. Sakharov proposed three conditions necessary for baryogenesis [3]:

1. **Baryon number non-conservation:** There must be processes that do not conserve baryon number. At the beginning, there was no matter in the Universe, and the total baryon number was zero. However, the total baryon number is no longer zero in the present-day Universe, as shown by galaxies and stellar structures that are formed by baryons.

2. **Matter-antimatter asymmetric processes:** There must be processes in nature that proceed at a different rate for matter and antimatter; otherwise, there should be equal amounts of matter and antimatter in the current Universe. Alternatively, matter and antimatter could have annihilated with each other, leaving no matter to form galactic structures.

   A mechanism that explains the difference between matter and antimatter on a fundamental level lies in *CP* violation. *CP* violation will be described in greater detail in Sec. 1.3 as well as in Chapter 2.

3. **Non-equilibrium thermal conditions:** There must be a time in the early Universe when it was not in thermal equilibrium. If baryogenesis had occurred under conditions of thermal equilibrium, then it would have been equally likely to proceed backwards. More specifically, any process that creates a net baryon number will be cancelled out by the corresponding reverse process. An inflationary expansion stage of the Universe, for example, can provide the environment where non-equilibrium thermal conditions can be found. (see, for example, [4]).

This work focuses on the fundamental mechanism that gives rise to the matter-antimatter asymmetry, as outlined in the second Sakharov condition.

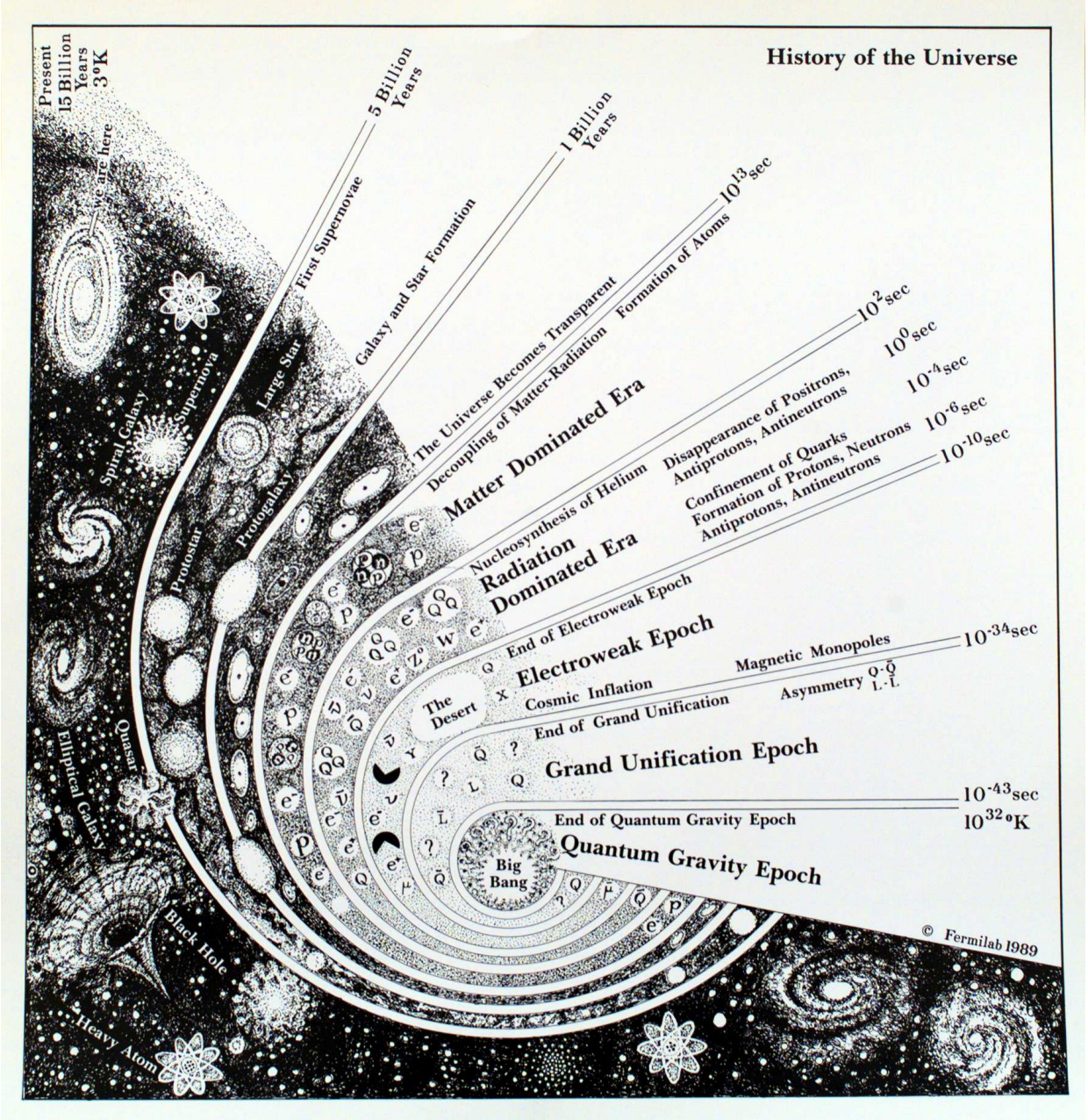

Figure 1.1: Evolution of the Universe after the Big Bang. The figure shows the different epochs in the history of the Universe. The Universe changes from radiation-dominated to matter-dominated at $\sim 100s$. Image source: `http://www-visualmedia.fnal.gov/VMS_Site/gallery/stillphotos/1999/1100/99-1145D.hr.jpg`

1.2 Standard Model

The fundamental particles and forces (except gravity) are described by the Standard Model. The forces are mediated by the exchange of particles of integer spins known as bosons. Fermions, which are particles of half-integer spins, are divided into two types: quarks and leptons. Quarks are confined in composite particles such as the proton and the neutron whereas leptons are observed independently[3]. Furthermore, quarks can only be found in specific combinations: they can either be clustered together in groups of three ("baryons") or in a quark-antiquark pair ("mesons"). Quarks and leptons are further classified into three generations, as shown in Fig. 1.2.

The main constituents of visible matter in the Universe today are baryons. An even larger fraction of the matter in the Universe is invisible, but its existence is inferred from observations. Known as "dark matter", it has generated much interest in the particle physics community regarding its origin; however, this is beyond the scope of the discussion here.

1.3 *CP* Violation

The *CP* symmetry is composed of two discrete symmetries in the Standard Model. The first symmetry, C (for charge conjugation[4]), is the operator that takes a particle state ψ to its antiparticle state $\bar{\psi}$:

$$C|\psi\rangle = |\bar{\psi}\rangle$$

One would expect this to be sufficient in providing a natural link between matter and antimatter at a fundamental level. However, neutrinos seem to violate this symmetry as they are observed to be all left-handed[5] while all anti-neutrinos are observed to be right-handed. If one applies the operator C to a (left-handed) neutrino state $|\nu_L\rangle$, one would result in a left-handed anti-neutrino $|\bar{\nu}_L\rangle$, which would not interact in the same way in the Standard Model. As a remedy, the P (parity) operator can be applied in addition. The P operator flips all external coordinates, so it also flips the "handedness" in our neutrino example:

[3] One notable exception to quark confinement is the top quark, which decays before it can form hadrons due to its mass

[4] More specifically, C flips all internal quantum numbers of a particle.

[5] The spin of a neutrino is anti-parallel with its direction of flight.

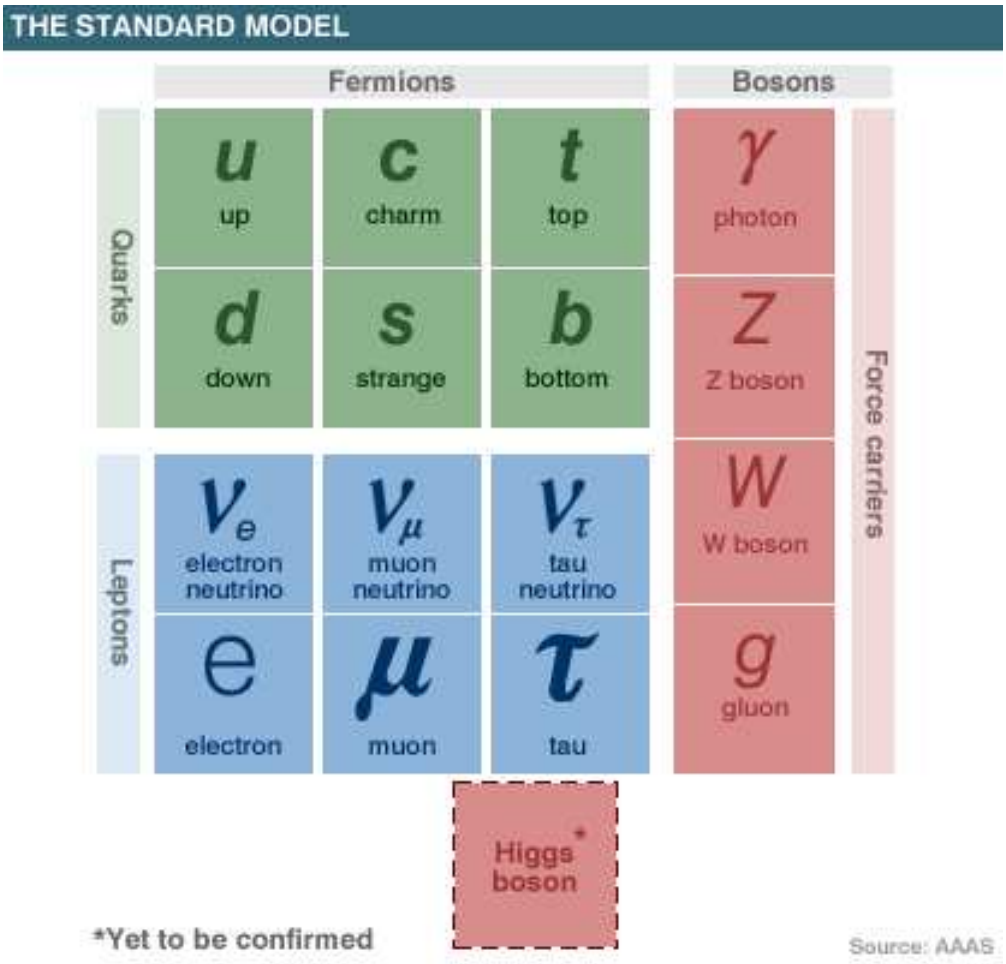

Figure 1.2: The fundamental particles in the Standard Model of particle physics. The quarks and leptons, which are both fermions, are divided into three generations, as represented by the three columns in the diagram. There are four force carriers: the photon is responsible for electromagnetic interactions, W and Z bosons for weak interactions and gluon for strong interactions. The Higgs boson arises from the Higgs field, which is postulated to explain the origin of mass. So far the Higgs boson has not been observed. Image source: `http://www.physorg.com`

$$CP|\nu_L\rangle = |\bar{\nu}_R\rangle$$

Systems that remain unchanged under a *CP* transformation are known as "*CP* symmetric". Conversely, systems that break this symmetry are said to display "*CP* violation", often labelled as CPV.

If our understanding of *CP* violation and *CP*-violating dynamics is complete, then one can predict the matter-antimatter asymmetry in the Universe. Since particles and anti-particles must be annihilated in pairs, the matter we observe today must be the remnant of the excess of matter over antimatter when both could still be found in the Universe. This excess can be calculated from the magnitude of *CP* violation that has been observed. Further, the number of photons in the Universe indicates how many pairs of particles and anti-particles have been annihilated. *CP* violation has indeed been observed in the quark sector, specifically in K and B meson decays and oscillations[6]. If the current observed values for *CP* violation in the Standard Model are used, then it is predicted that the baryon-to-photon ratio in the Universe is $n_B/n_\gamma \sim 10^{-20}$ [5]. This, however, differs from current cosmological observations by many orders of magnitude, where the baryon-to-photon ratio is $\sim 10^{-9}$ [6], which indicates that there are unobserved sources of *CP* violation.

Another possible source of *CP* violation in the Standard Model that has yet to be observed is from neutrino oscillations. Neutrinos come in three different flavours: ν_e, ν_μ and ν_τ. They are produced in decays associated with the three charged leptons. However, neutrinos are found to be able to transform from one flavour to another [7, 8], and such flavour oscillations can be *CP*-violating.

1.3.1 *CP* Violation from New Physics

Despite its successes, the Standard Model also has its shortcomings. For example, the Standard Model does not incorporate gravity in its descriptions and displays a "fine-tuning" problem[7]. A complete theory of fundamental particles must be able to provide answers to these problems; therefore, there must be extensions to the Standard Model that provide

[6] Oscillations are the processes where the particle changes flavour, e.g. a B^0 transforming into a $\overline{B}^0$.

[7] In the Higgs boson case, there exist quantum corrections that are much bigger than the mass of the Higgs boson. Such corrections must be cancelled precisely with other corrections, which is deemed unnatural. This is known as the "fine-tuning" problem.

a more complete description of fundamental particles. Such proposed extensions to the Standard Model can give rise to additional *CP* violation.

One possible extension to Standard Model is supersymmetry (SUSY) (see, for example, [9] and [10]). SUSY is the theory proposing the existence of a symmetry between fermions and bosons. Namely, all fermions in the Standard Model will have a corresponding supersymmetric bosonic partner, and vice versa. SUSY was initially proposed so that divergent terms in the interaction probability calculation due to SM dynamics can be cancelled out with those associated with SUSY dynamics; namely, the one-loop quantum correction due to a Dirac fermion can be cancelled with the corresponding correction due to a scalar boson. In the case of *CP* violation, SUSY can provide additional decay channels that do not appear in the Standard Model. Such decay channels can also be *CP*-violating, thus enhancing or cancelling the *CP* violation postulated to occur under the Standard Model.

Some models of extra dimensions can also give rise to additional *CP* violation [11]. However, most of the theory literature explores the *CP* violation arising from SUSY.

1.4 *CP* Violation Study in τ Decays

Currently, there is no direct evidence suggesting that leptons will undergo *CP*-violating processes. Searching for *CP*-violating decays in the lepton sector may help identify the missing portion of the matter-antimatter asymmetry in the Universe. Among the three charged leptons, the τ lepton is most likely to yield *CP* violation. It is more massive than the electron and the muon (μ), making it kinematically possible to decay into many different final states. The higher mass of the τ lepton can enhance some new physics effects. For example, the coupling to the charged Higgs boson in SUSY is larger for higher mass particles.

The decay channel studied in this work is $\tau^- \to \pi^- K_S^0 \left(\geq 0\pi^0\right) \nu_\tau$, where $K_S^0 \to \pi^+ \pi^-$ and $\pi^0 \to \gamma\gamma$. The *CP* violation is predicted to manifest itself in the form of a decay rate asymmetry[8] of $(0.33 \pm 0.01)\%$ [12]. Deviations from the Standard Model value would be evidence of new physics effects.

The τ leptons used in this study are produced in pairs via the collisions of positrons and electrons ($e^+e^- \to \tau^+\tau^-$) at the SLAC National Accelerator Laboratory in Palo Alto,

[8]Decay rate asymmetry here means the difference in the decay rates for $\tau^- \to \pi^- K_S^0 \left(\geq 0\pi^0\right) \nu_\tau$ and the corresponding anti-particle process divided by the sum of the decay rates. It will henceforth be referred to simply as "asymmetry".

California. The collisions are recorded by the *BABAR* detector. The accelerator and detector will be described in Chapter 3. The selection of the events will be outlined in Chapter 4, and the results will be presented in Chapter 5.

Chapter 2

Theory

2.1 Standard Model Overview

The Standard Model [13, 14, 15] describes the interactions between fundamental particles in nature. It is deemed to be highly successful, as all experimental results are in good agreement with predictions from the Standard Model. In this section a brief overview of the Standard Model is presented, with aspects relevant to the analysis highlighted.

In the Standard Model, the particles are divided into bosons and fermions. They possess integer and half-integer spins respectively, where spin is the intrinsic angular momentum of the particle. Bosons are the force carriers, so all forces or interactions between elementary particles are mediated by bosons. Fermions are the particles that form the basis of matter, and they can be divided further into leptons and quarks.

Table 2.1 lists the bosons in the Standard Model. Electromagnetic interactions involve the exchange of photons (γ) between two charged particles. Quarks are bound by the strong force through an exchange of gluons (g). The $W^{\pm}$ and Z^0 bosons are responsible for the weak interaction. The Higgs boson (H) is a consequence of the spontaneous symmetry breaking of the Higgs potential, which gives an explanation to the origin of mass [16]. The Higgs boson is the only fundamental particle in the Standard Model that remains to be discovered.

All quarks take part in strong, weak and electromagnetic interaction. Electromagnetic forces affect quarks because all quarks are charged: either $+2/3e$ or $-1/3e$. The coupling of strong force is stronger at small momenta and large distances, preventing quarks from being

Boson	Mass (GeV/c^2)	Spin	Charge	Force
γ	0	1	0	Electromagnetic
$W^{\pm}$	80.399±0.023	1	±1	Weak
Z	91.1876±0.0021	1	0	Weak
g	0	1	0	Strong
H	115< m_H <185 (95% C.L.)	0	0	

Table 2.1: Bosons in the Standard Model [1]

torn from bound state. As a result, no solitary quarks have been observed in experiments[1]. Rather, what can be observed is either a quark-antiquark pair called a meson, or a quark triplet called a baryon.

Leptons are further divided to the charged leptons (e, μ and τ) and the neutral leptons known as neutrinos (ν_e, ν_μ and ν_τ). While the charged leptons can interact electromagnetically, neutrinos cannot. However, all quarks and leptons can take part in weak interactions.

Weak interactions in leptons can only couple leptons belonging in the same generation. Recall that there are three generations:

$$\begin{pmatrix} \nu_e \\ e \end{pmatrix} \quad \begin{pmatrix} \nu_\mu \\ \mu \end{pmatrix} \quad \begin{pmatrix} \nu_\tau \\ \tau \end{pmatrix} \tag{2.1}$$

This means that while $e^- \to \nu_e W^-$ and $\mu^- \to \nu_\mu W^-$ can occur, $e^- \to \nu_\mu W^-$ is not observed. (ignoring any effects from neutrino oscillations).

The charged weak carriers $W^{\pm}$ can only couple to left-handed chiral fermion states. The left-handed chiral states are defined mathematically by the projection operator $\frac{1-\gamma^5}{2}$:

$$u_L = \frac{1}{2}\left(1-\gamma^5\right) u \tag{2.2}$$

where u_L is the left-handed chiral fermion state, and u is the particle spinor. The Z^0 boson, on the other hand, can couple to both left-handed and right-handed chiral states. The other aspects of the weak couplings are very similar to those in the electromagnetic case, so the electromagnetic force and the weak force are unified under the electroweak interaction, as

[1]The notable exception, as mentioned previously, is the top quark.

proposed by Salam, Glashow and Weinberg. The underlying symmetry of the electroweak force is described by the $SU(2)_L \times U(1)$ group [13, 14, 15]. As a consequence, leptons can be divided into left-handed doublets and right-handed singlets:

$$\begin{pmatrix} \nu_e \\ e_L \end{pmatrix} \quad \begin{pmatrix} \nu_\mu \\ \mu_L \end{pmatrix} \quad \begin{pmatrix} \nu_\tau \\ \tau_L \end{pmatrix} \qquad \begin{pmatrix} e_R \end{pmatrix} \quad \begin{pmatrix} \mu_R \end{pmatrix} \quad \begin{pmatrix} \tau_R \end{pmatrix} \tag{2.3}$$

Note that the right-handed singlets only contain the charged leptons because no right-handed neutrinos are observed[2].

2.1.1 Quark Mixing

The generations in the quark sector are not divided in a manner as straightforward as the case in the lepton sector. The quark generations in mass eigenstates are:

$$\begin{pmatrix} u \\ d \end{pmatrix} \quad \begin{pmatrix} c \\ s \end{pmatrix} \quad \begin{pmatrix} t \\ b \end{pmatrix} \tag{2.4}$$

but both $d \to uW^-$ and $s \to uW^-$ have been observed, showing that the weak interaction can mix quarks across generations. For the case of three quark generations, the weak interaction couples the quarks according to the weak eigenstates instead of the mass eigenstates. The weak eigenstates are:

$$\begin{pmatrix} u \\ d' \end{pmatrix} \quad \begin{pmatrix} c \\ s' \end{pmatrix} \quad \begin{pmatrix} t \\ b' \end{pmatrix} \tag{2.5}$$

where (d', s', b') and (d, s, b) are related via a complex-valued matrix called the Cabibbo-Kobayashi-Muskawa (CKM) matrix V_{ij} [18, 19]:

[2]Right-handed neutrinos may exist, but they do not interact in the Standard Model. The masslessness of the neutrinos is the consequence of the fact that the Yukawa coupling requires both left-handed and right-handed chiral states. This Yukawa coupling is essential in the generation of Dirac masses in the Standard Model Higgs-lepton Yukawa Lagrangian (see, for example, [17]). With the discovery of massive neutrinos, this whole description can change. However, this is beyond the scope of the discussion here and the description on the Standard Model here will assume that the neutrinos are massless.

$$\begin{bmatrix} d' \\ s' \\ b' \end{bmatrix} = \begin{bmatrix} V_{ud} & V_{us} & V_{ub} \\ V_{cd} & V_{cs} & V_{cb} \\ V_{td} & V_{ts} & V_{tb} \end{bmatrix} \begin{bmatrix} d \\ s \\ b \end{bmatrix} \tag{2.6}$$

where V_{ij} are complex numbers. The CKM matrix is unitary, and can be rewritten as:

$$\begin{bmatrix} c_{12}c_{13} & s_{12}c_{13} & s_{13}e^{-i\delta} \\ -s_{12}c_{23} - c_{12}s_{23}s_{13}e^{i\delta} & c_{12}c_{23} - s_{12}s_{23}s_{13}e^{i\delta} & s_{23}c_{13} \\ s_{12}s_{23} - c_{12}c_{23}s_{13}e^{i\delta} & -c_{12}s_{23} - s_{12}c_{23}s_{13}e^{i\delta} & c_{23}c_{13} \end{bmatrix} \tag{2.7}$$

where $s_{ij} = \sin(\theta_{ij})$ and $c_{ij} = \cos(\theta_{ij})$ are trigonometric expressions with rotation angles θ_{ij} and δ is the complex phase. It can be further shown that a 3×3 unitary matrix is the smallest matrix where there exists a complex phase which cannot be reduced by a rotation of the quark fields. This complex phase gives rise to *CP* violation[3].

Empirically, the magnitudes of all nine elements in the CKM matrix are as follows:

$$\begin{bmatrix} 0.97428 \pm 0.00015 & 0.2253 \pm 0.0007 & 0.00347^{+0.00016}_{-0.00012} \\ 0.2252 \pm 0.0007 & 0.97345^{+0.00015}_{-0.00016} & 0.0410^{+0.0011}_{-0.0007} \\ 0.00862^{+0.00026}_{-0.00020} & 0.0403^{+0.0011}_{-0.0007} & 0.999152^{+0.000030}_{-0.000045} \end{bmatrix} \tag{2.8}$$

and $\delta = (59 \pm 15)^\circ$ (for a summary of the measurements of the CKM matrix, see [1]). Currently, *CP* violation has only been observed in weak interactions, and the CKM matrix provides the only mechanism for generating *CP* violation in the Standard Model.

[3]In fact, the 3×3 CKM matrix was proposed to explain *CP* violation in the quark mixing matrix after the discovery of *CP* violation in the kaon sector. When the CKM matrix was proposed, only three quarks were known.

2.2 *CP* Violation Measurements

2.2.1 Neutral Kaon Mesons

There are two neutral K meson flavour eigenstates in nature: the K^0 and the $\overline{K}^0$. They can be taken from one state to another by the charge parity operator CP[4]:

$$CP|K^0\rangle = -|\overline{K}^0\rangle \tag{2.9}$$
$$CP|\overline{K}^0\rangle = -|K^0\rangle \tag{2.10}$$

The normalized CP eigenstates are:

$$|K_1\rangle \equiv \frac{1}{\sqrt{2}}\left(|K^0\rangle - |\overline{K}^0\rangle\right) \tag{2.11}$$
$$|K_2\rangle \equiv \frac{1}{\sqrt{2}}\left(|K^0\rangle + |\overline{K}^0\rangle\right) \tag{2.12}$$

The CP eigenvalues are +1 and -1 for the two eigenstates:

$$CP|K_1\rangle = |K_1\rangle \tag{2.13}$$
$$CP|K_2\rangle = -|K_2\rangle \tag{2.14}$$

If CP is conserved, then the CP operator commutes with the Hamiltonian of the system. Since $|K_1\rangle$ and $|K_2\rangle$ form a non-degenerate basis for CP in the K meson sector, they should also be non-degenerate eigenstates for $\mathcal{H}$. In other words, K_1 and K_2 will not mix and will decay independently. Neutral K mesons can decay into two or three pions. Since a $\pi^-\ \pi^+$ system has CP eigenvalue of 1 and $\pi^-\ \pi^+\ \pi^0$ has eigenvalue -1, K_1 will only decay into two pions whereas K_2 will only decay into three pions. Furthermore, K_2 will have a longer lifetime because the available phase space for the two-particle decay is greater than that for the three-particle decay. Therefore, for a sufficiently long time after the production of the neutral K mesons, one would expect only $\pi^-\ \pi^+\ \pi^0$ decays and no $\pi^-\ \pi^+$ decays if CP symmetry is valid.

[4]Some literature will not have the minus sign in Eqs. 2.9 and 2.10; however, the point is that both signs should be the same. The sign will only change an overall phase to the two CP eigenstates and will leave the physics unaltered.

In 1964 Cronin and Fitch carried out an experiment investigating the decays of neutral K mesons as described above [20]. In the experiment, evidence of neutral K mesons decaying into $\pi^+ \pi^-$ was found even after a time much longer than the K_2 lifetime. This was the first evidence of *CP* violation. In other words, the *CP* eigenstates $|K_1\rangle$ and $|K_2\rangle$ are not exact eigenstates for the Hamiltonian. The two energy eigenstates, commonly called $|K_L^0\rangle$ and $|K_S^0\rangle$ respectively for their long and short lifetimes, are admixtures of K^0 and $\overline{K}^0$ with different mixing amplitudes from those in K_1 and K_2. The lifetimes for K_L^0 and K_S^0 are [1]:

$$\tau\left(K_L^0\right) = (5.116 \pm 0.020) \times 10^{-8}\,\mathrm{s} \qquad \tau\left(\mathrm{K_S^0}\right) = (8.953 \pm 0.005) \times 10^{-11}\,\mathrm{s}$$

Physically, the two flavour eigenstates can change from one to another by an exchange of two W bosons, as depicted in Fig. 2.1. The oscillation between K^0 and $\overline{K}^0$ depends on the mass difference ($\Delta m = (5.290 \pm 0.015) \times 10^9 c^{-2}\hbar\,\mathrm{s}^{-1}$ [1]) between the two flavour eigenstates. The period of oscillation T is approximately 0.2×10^{-9} s or $cT \approx 6$ cm. The impact of neutral kaon oscillation on the measurement in this study will be further explored in Chapter 5 and in Appendix E.

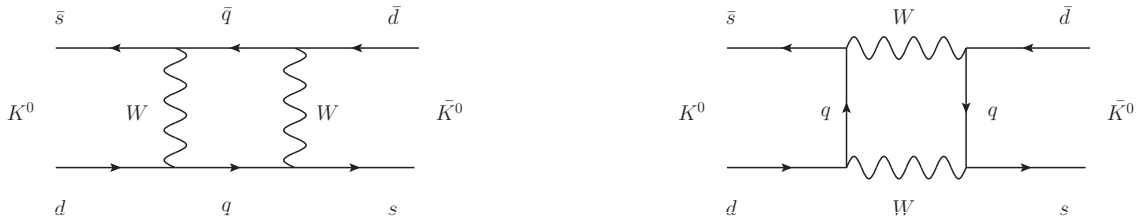

Figure 2.1: Feynman diagrams showing how a K^0 ($\overline{s}\ d$) transforms into a $\overline{K}^0$ ($s\ \overline{d}$), where q represents a u, c or t quark.

2.2.2 *CP* Violation in the Kaon Sector

If one takes the generalization that *CP* symmetry may not hold but still assumes *CPT* invariance, the two energy eigenstates can be derived as follows:

$$|K_S^0\rangle = p|K^0\rangle + q|\bar{K^0}\rangle \tag{2.15}$$

$$|K_L^0\rangle = p|K^0\rangle - q|\bar{K^0}\rangle \tag{2.16}$$

where p and q are complex numbers and $|p|^2 + |q|^2 = 1$. The derivation is outlined in [4] and is presented in Appendix A. An asymmetry parameter ϵ can be defined:

$$\epsilon = \frac{p-q}{p+q} \tag{2.17}$$

Note that $\epsilon = 0$ when there is no *CP* violation. Furthermore, the two eigenstates are no longer orthogonal; rather, the inner product of the two eigenstates is proportional to the real part of ϵ to first order of ϵ:

$$\langle K_L^0 | K_S^0 \rangle = |p|^2 - |q|^2 \approx 2\Re e(\epsilon) \tag{2.18}$$

The parameter ϵ is related to the processes as represented by the Feynman diagrams in Fig. 2.1. The matrix element (M_{fi}) for the transition of K^0 to $\overline{K}^0$ by an exchange of quarks q and q' is proportional to $G_F^2 V_{qd} V_{qs}^* V_{q'd} V_{q's}^*$. Conversely, the matrix element for the transition of $\overline{K}^0$ to K^0 is proportional to the complex conjugate M_{fi}^*. The difference in transition rates between $K^0 \to \overline{K}^0$ and $\overline{K}^0 \to K^0$ is then proportional to the imaginary part of M_{fi}:

$$\Gamma\left(K^0 \to \overline{K}^0\right) - \Gamma\left(\overline{K}^0 \to K^0\right) \propto \Im m(M_{fi}) \tag{2.19}$$

In other words, the non-zero complex phase in the CKM matrix is a necessary condition for a non-zero ϵ, which represents the mixture of different *CP* eigenstates in K_L^0 and K_S^0.

In the next section we will show that the asymmetry measured in this work is proportional to the real part of ϵ ($\Re e(\epsilon)$). One can measure $\Re e(\epsilon)$ by noting that only the K_L^0 component remains at a time sufficiently long after production of the neutral kaon:

$$|K_L^0\rangle = \frac{1}{\sqrt{2}\sqrt{1+|\epsilon|^2}} \left[(1+\epsilon)|K^0\rangle + (1-\epsilon)|\overline{K}^0\rangle\right] \tag{2.20}$$

Due to the $\Delta Q = \Delta S$ rule[5], the semileptonic decay $K_L^0 \to \pi^+ \ell^- \overline{\nu}_\ell$ primarily comes from the $\overline{K}^0$ component of the K_L^0 [4]. Fig. 2.2 shows that as $\overline{K}^0$ meson decays to a π^+ meson, the strangeness changes from -1 to 0, and the charge increases by 1. Similarly, $K_L^0 \to \pi^- \ell^+ \nu_\ell$ primarily comes from the K^0 component. The semileptonic decay rates for the K_L^0 are

[5]The $\Delta Q = \Delta S$ rule [21] states that processes where strangeness and charge change by the same amount are favoured. Processes such as $\Delta Q = -\Delta S$ also occurs, but it is a second-order process in the Standard Model. Its rate is proportional to G_F^2 [22].

proportional to the components of the K^0 and the $\overline{K}^0$:

$$\Gamma\left(K_L^0 \to \pi^+\ell^-\overline{\nu}_\ell\right) \propto |\langle\overline{K}^0|K_L^0\rangle|^2 \propto |1-\epsilon|^2 \approx 1 - 2\Re e(\epsilon) \quad (2.21)$$

$$\Gamma\left(K_L^0 \to \pi^-\ell^+\nu_\ell\right) \propto |\langle K^0|K_L^0\rangle|^2 \propto |1+\epsilon|^2 \approx 1 + 2\Re e(\epsilon) \quad (2.22)$$

where the approximations are good to the first order of ϵ. Thus, by comparing the decay rates for $K_L^0 \to \pi^+\ \ell^-\ \overline{\nu}_\ell$ and $K_L^0 \to \pi^-\ \ell^+\ \nu_\ell$, one can measure $\Re e(\epsilon)$[6],

$$\frac{\Gamma\left(K_L^0 \to \pi^-\ell^+\nu_\ell\right) - \Gamma\left(K_L^0 \to \pi^+\ell^-\overline{\nu}_\ell\right)}{\Gamma\left(K_L^0 \to \pi^-\ell^+\nu_\ell\right) + \Gamma\left(K_L^0 \to \pi^+\ell^-\overline{\nu}_\ell\right)} \approx 2\Re e(\epsilon) \quad (2.23)$$

(the approximation is accurate to the first order of ϵ). Experimental results find $2\Re e(\epsilon) = (3.27 \pm 0.12) \times 10^{-3}$ [12].

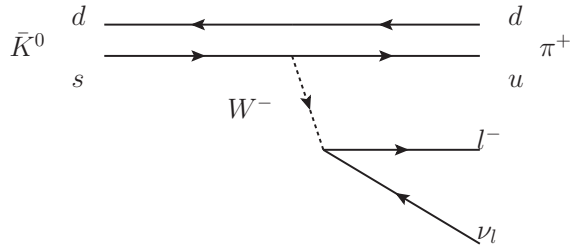

Figure 2.2: Feynman diagram for $\overline{K}^0 \to \pi^+\ \ell^-\ \overline{\nu}_\ell$. The strangeness changes from -1 ($\overline{K}^0$) to 0 (π^+) during the process, so the charge changes from 0 ($\overline{K}^0$) to 1 (π^+).

CP violation can also be observed in B meson decays, and this is the motivation behind the experiments at the B factories such as *BABAR*. The decays of B_d mesons, for example, help constrain some of the parameters in the CKM matrix [4]. *CP* violation can also be observed in precision measurements of the B^0-$\overline{B}^0$ mixing as a time-dependent asymmetry [4].

[6]Results for $\ell^- = e^-$ are reported by the Princeton group [23] and the CERN-Heidelberg group [24]. The mode $\ell^- = \mu^-$ is measured by the CERN-Heidelberg group [24], the Stanford group [25] and the Brookhaven-Yale group [26].

2.2.3 *CP* Violation in the τ Lepton Sector

CP violation has only been observed in the quark sector. However, Bigi and Sanda have proposed that there can be *CP* violation in τ decays under the Standard Model [12].

According to Standard Model, the following transition amplitudes are equal:

$$T\left(\tau^- \to \bar{K^0}\pi^-\nu\right) = T\left(\tau^+ \to K^0\pi^+\nu\right) \tag{2.24}$$

However, observations are made with the mass eigenstates K_L^0 and K_S^0, not the flavour eigenstates K_0 and $\bar{K_0}$. The mixing of the eigenstates is exactly the same as what is presented in the previous section.

Since K_L^0 and K_S^0 are not orthogonal, both $K_L^0 \to 2\pi$ and $K_S^0 \to 2\pi$ are possible. The asymmetry for the $\tau^- \to K_S^0\pi^-\nu_\tau$ is then [12]:

$$A = \frac{\Gamma\left(\tau^+ \to \text{“}\mathrm{K_S^{0\prime\prime}}\pi^+\bar{\nu_\tau}\right) - \Gamma\left(\tau^- \to \text{“}\mathrm{K_S^{0\prime\prime}}\pi^-\nu_\tau\right)}{\Gamma\left(\tau^+ \to \text{“}\mathrm{K_S^{0\prime\prime}}\pi^+\bar{\nu_\tau}\right) + \Gamma\left(\tau^- \to \text{“}\mathrm{K_S^{0\prime\prime}}\pi^-\nu_\tau\right)} = |p|^2 - |q|^2 \approx 2\Re e(\epsilon) \tag{2.25}$$

where “K_S^0” (in quotation marks) represents both K_S^0 and K_L^0 decays to the $\pi^+\pi^-$ final state. The approximation is accurate to the first order of ϵ. The description given above does not specify the dynamics that generate $|q| \neq |p|$; rather, it only relies on the assumption that the τ decay is described by SM dynamics [12].

If the asymmetry is measured to deviate from the SM predicted value, then there is indication that dynamics from other physics processes are at play. One possible new physics effect is *CP* violation arising from the interference of amplitudes, one of which involving an exchange of SUSY particles. In Fig. 2.3, for example, the SM amplitude (left) and the amplitude of a charged Higgs exchange (right) can interfere. Namely, the charged Higgs diagram will contribute to the *s*-wave state of the hadronic system whereas the SM W boson diagram will contribute to both *s*- and *p*-wave states [27]. However, while this effect is apparent in an angular distribution analysis, a study on the overall asymmetry should not be affected barring any detector-induced effects. There are, however, no explicit predictions of the impact of new physics effects on *CP* violation in τ decays.

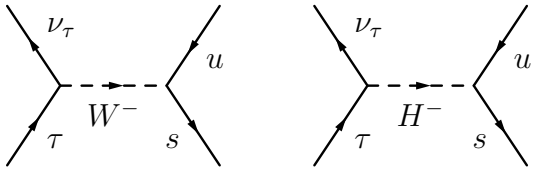

Figure 2.3: τ decaying via a W boson and a charged Higgs boson.

2.3 Goal of the Study

The goal of the study is to measure the asymmetry presented by Bigi and Sanda in τ lepton decays. τ lepton decays provide a clean laboratory for studies, which is desirable in the investigations of new physics effects. Namely, hadronic backgrounds will be low, and detector inefficiencies arising from a high number of charged tracks in the detector can be avoided. If the *CP* asymmetry is found to deviate from the SM prediction, then it is a signal for new physics. The measured *CP* asymmetry may also be used as a constraint to rule out some new physics models.

The number of decays observed is proportional to the decay rate. By counting the numbers of decays for the modes $\tau^- \to \pi^- K_S^0 (\geq 0\pi^0)\, \nu_\tau$ and $\tau^+ \to \pi^+ K_S^0 (\geq 0\pi^0)\, \overline{\nu}_\tau$ separately, one can then compute the asymmetry:

$$A_Q = \frac{N\left(\tau^+ \to \pi^+ K_S^0 (\geq 0\pi^0)\, \overline{\nu}_\tau\right) - N\left(\tau^- \to \pi^- K_S^0 (\geq 0\pi^0)\, \nu_\tau\right)}{N\left(\tau^+ \to \pi^+ K_S^0 (\geq 0\pi^0)\, \overline{\nu}_\tau\right) + N\left(\tau^- \to \pi^- K_S^0 (\geq 0\pi^0)\, \nu_\tau\right)} \tag{2.26}$$

The *BABAR* experiment provides a large sample of τ lepton decays, which is instrumental in reducing the statistical uncertainty in the final result and in turn can increase the sensitivity to new physics effects, should there be any. The *BABAR* particle detector as well as strategy of selecting the dataset will be described in subsequent chapters.

Chapter 3

The *BABAR* Experiment

The τ leptons needed for this analysis were produced at the SLAC National Accelerator Laboratory in Stanford, California, and recorded by the *BABAR* Experiment. The main focus of the facility is to study *CP* violation in the B meson sector. However, it also provides an opportunity to study τ physics because the $e^+e^- \to \tau^+\tau^-$ cross section is comparable to that for the $e^+e^- \to b\overline{b}$ at the energy scale that *BABAR* is run (see Table 3.1 for the cross sections of various processes). In this chapter, details of the SLAC accelerator and the *BABAR* Experiment will be described.

$e^+e^- \to$	Cross section (nb)
$b\overline{b}$	1.05
$c\overline{c}$	1.30
$s\overline{s}$	0.35
$u\overline{u}$	1.39
$d\overline{d}$	0.35
$\tau^+\tau^-$	0.92
$\mu^+\mu^-$	1.16
e^+e^-	~ 40

Table 3.1: Cross sections for different processes at $\sqrt{s} = 10.58\,\text{GeV}$. The $e^+e^- \to e^+e^-$ cross section is the effective cross section within experimental acceptance [28].

3.1 SLAC and PEP-II

The *BABAR* experiment uses two accelerators to generate the e^+ and e^- beam : the SLAC linear accelerator and the PEP-II storage rings. The SLAC linear accelerator (linac) is 3.2 km long and injects high-energy electrons and positrons into the PEP-II's storage rings. PEP-II consists of the High Energy Ring (HER) and the Low Energy Ring (LER) for the 9.0 GeV and 3.1 GeV electron and positron beams, respectively (see Fig. 3.1). The typical currents in the HER and the LER are 0.7 and 1.3 A, respectively [29]. The two beams collide at the interaction point, which is surrounded by the *BABAR* detector. A total luminosity of $557\,\mathrm{fb}^{-1}$ had been delivered, of which $531\,\mathrm{fb}^{-1}$ was recorded by *BABAR*. In this work only the data collected at the $\Upsilon(4S)$ resonance ($\sqrt{s} = 10.58\,\mathrm{GeV}$) is used, corresponding to a total luminosity of $476\,\mathrm{fb}^{-1}$.

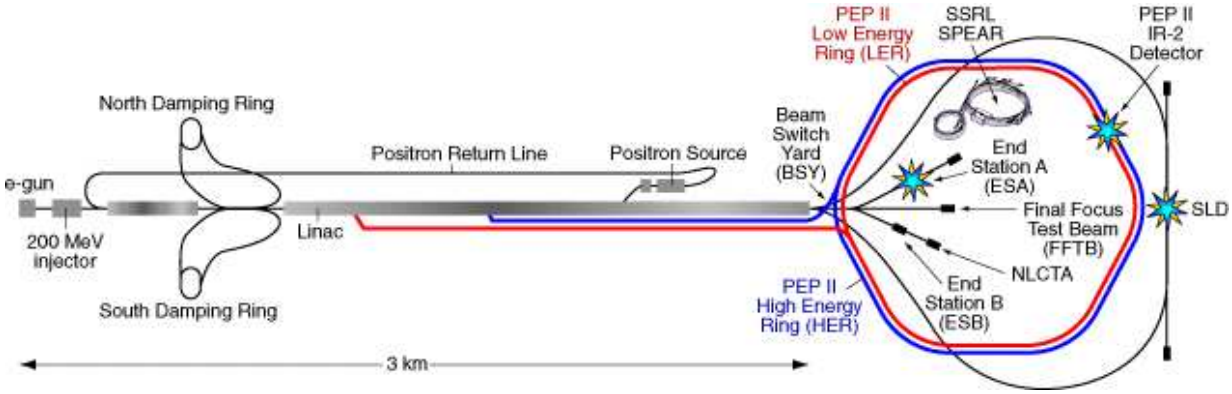

Figure 3.1: The SLAC linear accelerator. The e^+ and e^- beams collide at the site of the *BABAR* detector, labelled as PEP-II IR-2 detector in the diagram. Image source: `http://www.slac.stanford.edu/BFROOT/www/Detector/Images/Images.html`

3.2 The *BABAR* Detector

The schematic of the *BABAR* detector is given in Fig. 3.2[1]. The detector consists of a silicon vertex tracker measuring the trajectory of charged particles close to the e^+e^- collision vertex,

[1]The standard coordinate system defined for the *BABAR* detector is a right-handed coordinate system such that the positive z-axis is the e^- beam axis while the x-axis points upwards. The angles ϕ and θ are defined as in the usual spherical coordinate case. The origin of the coordinate system is at the e^+e^- interaction point.

a gas drift chamber measuring the trajectory of charged particles up to a radius of 80 cm, a Cherenkov light detector distinguishing between the different particles, a caesium iodide calorimeter measuring the energy of electrons and photons, and an instrumented iron return flux system for identifying muons. Fig. 3.3 shows an event in the detector with signals detected in different components of the detector. The main subsystems of the detector are:

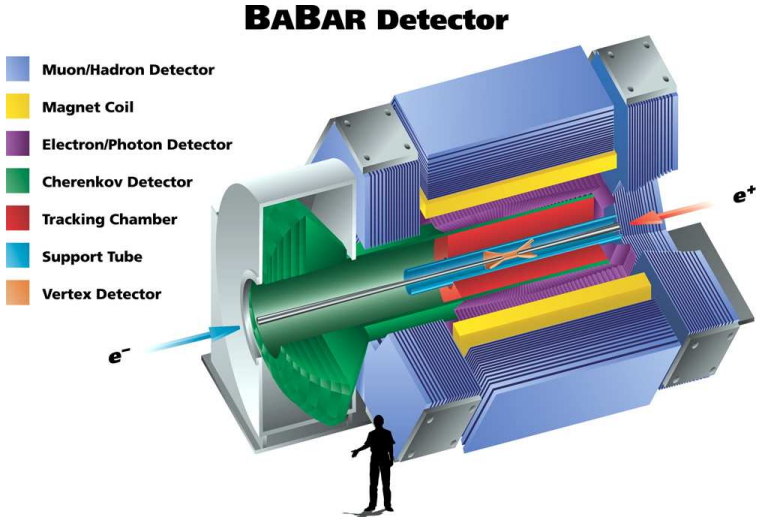

Figure 3.2: Layout of the *BABAR* detector and its components, which include the Silicon Vertex Tracker (orange), Drift Chamber (red), the support tube (light blue), Detector of Internally Reflected Cherenkov light (green), Electromagnetic Calorimeter (purple), the magnet coil (yellow) and Instrumented Flux Return (dark blue) [29]. The person is drawn for scale.

1. Silicon Vertex Tracker (SVT). Consisting of five concentric cylindrical layers of double-sided silicon microstrip detectors, the SVT provides information on the position of a charged particle based on the signals in the silicon strips as it traverses the component. If a neutral particle decays close to the e^+e^- collision beam spot, then the SVT can be used to determine the position of the decay vertex with high precision.

   The SVT provides precise angular information since the inner points are less affected by multiple scattering. It is also the only subsystem used in track reconstruction for charged particles with a transverse momentum less than 100 MeV/c, as the magnetic field prevents these particles from reaching the drift chamber (DCH). The performance properties are outlined in Table 3.2 [28, 29]. The dE/dx resolution of the SVT allows

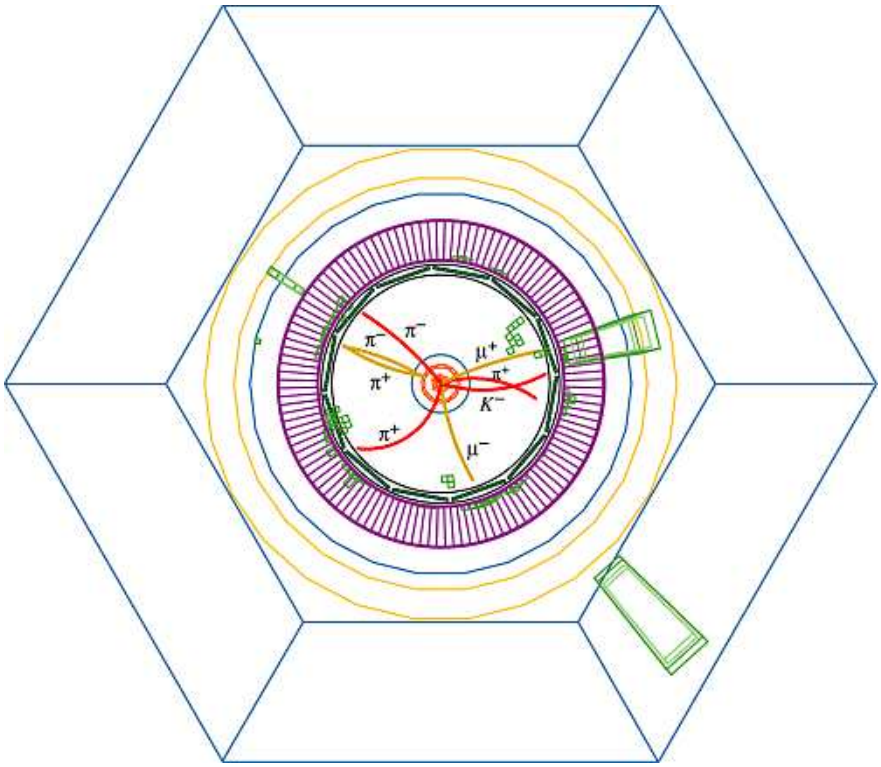

Figure 3.3: Display of an event in the *BABAR* detector. In this event, an e^+e^- pair travelling perpendicularly to the page produces $B^0\overline{B}^0$ after collision. One of the neutral B mesons decays into a pair of muons and a pair of pions (marked in gold) while the other decays into a kaon and three pions (marked in red). The reconstructed tracks in the SVT and DCH, as well as the energy deposits in the calorimeter (green) and the muon signal in the IFR, are displayed in the diagram. Image source: `http://www2.lns.mit.edu/~LQS/old_page/MIT%20Laboratory%20for%20Nuclear%20Science%20%20Lepton-Quark%20Studies%20Group.htm`

for a 95%-confidence separation between charged kaons and pions up to a momentum of 500 MeV/c, as well as kaons and protons below a momentum of 1 GeV/c.

2. Drift Chamber (DCH). This subsystem provides the primary momentum measurement for charged particles and energy loss measurements for particle identification. The chamber is filled with helium gas and contains axial field wires and sense wires. The field wires maintain an electric field in the chamber whereas the sense wires detect ionisation electrons. As a charged particle passes through the chamber, it ionises the gas along its trajectory, and the resulting electrons drift toward the sense wires. The

Property	Values
Angular coverage θ	$20.1^\circ < \theta < 150.2^\circ$
Point resolution	10–15 μm (inner layers)
	30–40 μm (outer layers)
dE/dx resolution (for MIP)	14%

Table 3.2: Performance properties of the Silicon Vertex Tracker (SVT) .

drift velocity of the electrons can be calculated from the known electric field and the properties of the gas. The position of the original ionising track can then be determined from the time for the ionisation electrons to travel to the sense wire.

The energy loss per unit length (dE/dx) as the charged particle traverses the chamber can be used to identify the particle. Fig. 3.4 shows dE/dx as a function of momentum. The measurement of the energy loss can be derived from the total charge collected in each drift cell.

The DCH is important in identifying decay vertices of long-lived particles that lie outside of the SVT. The K_S^0 meson, one of the particles in the final state of this study with a lifetime of $\tau = (0.8958 \pm 0.0005) \times 10^{-10} s$ and a decay length of $c\tau = 2.6842\,\mathrm{cm}$ [1], mainly decays in the DCH. Fig. 3.5 shows the mass of $\pi^+\pi^-$ and the decay length[2] of the K_S^0 meson decaying in the DCH for events selected in this work.

The SVT and DCH together form the tracking system. For tracks with the transverse momentum above $3\,\mathrm{GeV}/c$, the resolutions are measured to be [29]:

$$\sigma_{d_0} = 23\,\mu\mathrm{m} \quad \sigma_{\phi_0} = 0.43\,\mathrm{mrad}$$
$$\sigma_{z_0} = 29\,\mu\mathrm{m} \quad \sigma_{tan\lambda} = 5.3 \times 10^{-4}$$

where d_0 and z_0 are the distances of the point of closest approach of the track to the origin of the coordinate system in the transverse plane and along the z-axis, respectively. ϕ_0 is the azimuthal angle of the track. λ is the angle between the track momentum and the transverse plane.

[2]Decay length is the distance the particle travels from the point of production to the point where it decays.

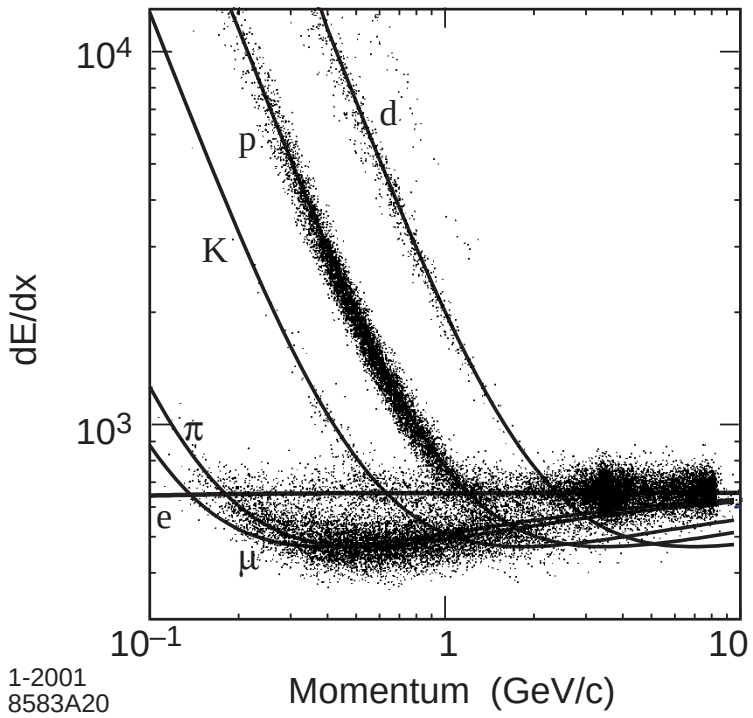

Figure 3.4: Energy loss of particles in the drift chamber as a function of momentum. The plot shows different relations between energy loss and the momentum of the particle depending on whether the particle is an electron (e), muon (μ), kaon (K), proton (p) or a deuteron (d) [29].

While the measurements near the interaction point are done in the SVT, the transverse momentum is measured primarily in the DCH. The resolution of the transverse momentum of a track p_t can be derived from cosmic muons[3], and the data are found to follow a linear relationship:

$$\sigma_{p_t}/p_t = (0.13 \pm 0.01)\% \cdot p_t + (0.45 \pm 0.03)\% \tag{3.1}$$

where the transverse momentum p_t is measured in GeV/c [29].

3. Detector of Internally Reflected Cherenkov light (DIRC). This detector is designed for charged hadron (π^-/K^-) particle identification. The DIRC determines the velocity of

[3]The upper and lower portions of the tracks from cosmic muons are fitted separately. Since the momentum should be the same, the measured values for the momenta of the two track fits should also be consistent. Any difference is taken as the uncertainty.

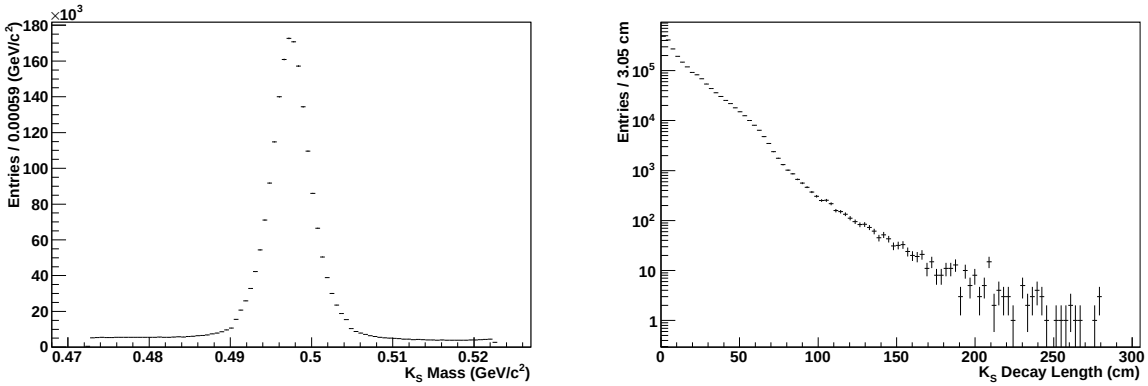

Figure 3.5: Plots of $\pi^+\ \pi^-$ invariant mass (left) and distance travelled from e^+e^- collision vertex to the K^0_S decay vertex (right) of the K^0_S meson in the *BABAR* detector. The sample consists of $K^0_S \to \pi^+\ \pi^-$ used in this work. Deviations from an exponential decay in the right-hand plot are due to detector effects.

a charged track from the Cherenkov light emitted as the particle traverses the DIRC. Cherenkov light is generated when a charged particle is travelling at a speed that is greater than the speed of light in the medium. The light is emitted along a cone, and the angle of the cone can be used to determine the velocity of the particle. The velocity, along with the momentum information obtained from the tracking chamber, can then be used to determine the mass of the particle, which in turn is used for particle identification. While π/K separation is based on dE/dx measurements in the SVT and DCH at low momentum, the DIRC is primarily responsible for distinguishing charged pions from charged kaons at high momentum. The DIRC can also help identify electrons and muons.

Fig. 3.6 depicts the relationship between the Cherenkov angle and the momentum of the particle in the laboratory frame. As shown in the plot, kaons and protons are well separated from pions, muons and electrons.

4. Caesium Iodide Electromagnetic Calorimeter (EMC). A calorimeter measures the energy and position of a particle. As an electron traverses the calorimeter, it can radiate

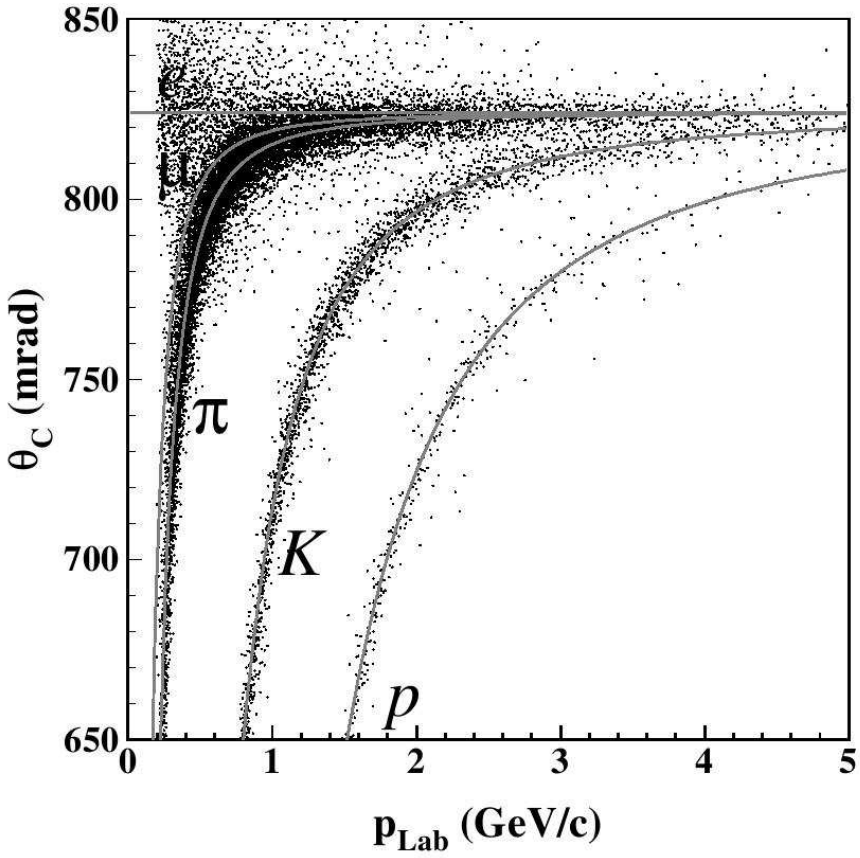

Figure 3.6: The Cherenkov angle of tracks as a function of momentum in the laboratory frame for different particles. From top to bottom, the grey lines represent the predicted values for the Cherenkov angles of electron (e), muon (μ), pion (π), kaon (K) and proton (p) [30].

photons by bremsstrahlung[4]. The photons, if they are energetic enough, can produce e^+e^- pairs. Depending on the energy of the e^+e^- pairs, they can also in turn emit more photons by bremsstrahlung (the positrons can also annihilate with an electron to produce photons). The result is a shower of particles being produced in the calorimeter, with the energy and momentum of the original particle being distributed among these new particles in the shower.

The EMC of the *BABAR* detector consists of a central component (barrel) and an endcap in the forward region. The thallium-doped caesium iodide (CsI(Tl)) crystals in the EMC are lined in such a way that they point towards the interaction point. Signals in the crystals are read out with silicon photodiodes [29]. The length of the crystals range from $16.0X_0$ to $17.5X_0$ [5], with length increasing in steps of $0.5X_0$ as one moves from the center of the barrel to the edge of the endcap.

The calorimeter can help identify the charged particle. The showers generated by electrons and photons are well-contained in the EMC typically; however, muons pass through the EMC while leaving only minimal energy in the subsystem. To see if the particle is charged or neutral, one must look for any charged track in the tracking system (SVT and DCH) that points at a cluster in the EMC. The main purpose of the EMC is to determine the position and energy of the electromagnetic particle, as well as separating electrons, photons and neutral pions. Its caesium iodide crystals provide high energy and angular resolution even in the low photon energy regime.

The energy resolution of the EMC is [29]:

$$\frac{\sigma_E}{E} = \frac{(2.32 \pm 0.30)\%}{\sqrt[4]{E}} \oplus (1.85 \pm 0.12)\% \tag{3.2}$$

and angular resolution is [29]:

$$\sigma_\theta = \sigma_\phi = \frac{3.87 \pm 0.07}{\sqrt{E}} mrad \tag{3.3}$$

[4]Bremsstrahlung can occur in principle for any charged particles, but the radiation power falls off as m^{-4} for particles with acceleration perpendicular to velocity, or as m^{-6} for particles with acceleration parallel to velocity. Since electron is the lightest charged particle, it is also the particle most probable to radiate by bremsstrahlung.

[5]X_0 is the radiation length, which is the mean distance a high electron energy travels before its energy is reduced by 1/e. For the CsI(Tl) crystals used in the EMC, X_0 is 1.85 cm [29].

In both Eqs. 3.2 and 3.3, energy E is measured in GeV and $\oplus$ signifies adding in quadrature. The first term in Eq. 3.2 is due to photon statistical fluctuations, whereas the latter is due to shower leakage.

5. A superconducting coil provides a 1.5 T solenoidal magnetic field pointing in the positive z-axis. Under the presence of a magnetic field, the trajectory of a charged particle bends. The charge of the particle determines the direction in which the trajectory bends, and the momentum of the particle determines the curvature of the track.

6. Instrumented Flux Return (IFR) is used for muon identification down to about 0.6 GeV/c and hadron identification. Low-energy muons can lose all energy due to ionisation and stop in the EMC whereas muons with momentum greater than 1 GeV/c pass through the EMC. The IFR is made of layers of iron and steel, with active detectors situated between each layer to detect the particles or the showers generated in the IFR layers. This IFR design can discriminate between muons and pions because muons can penetrate iron or steel more easily than pions. Fig. 3.7 shows the identification efficiency of muons and pions as a function of momentum in the laboratory frame [29].

3.3 Trigger

The e^+ and e^- bunches pass through each other millions of times per second. Periodically a pair of e^+ and e^- may collide and produce an event. The purpose of the trigger is to identify and record these events by "triggering" on some activity in the *BABAR* detector. The *BABAR* trigger consists of a hardware level known as Level 1 (L1) and a software level known as Level 3 (L3)[6]. The L1 trigger uses information from the DCH for charged particles, the EMC for the neutral particles, and the IFR for the cosmic trigger. The DCH and EMC will determine whether the event is due to an e^+e^- collision, and the IFR will determine whether the event is coming from cosmic ray background and will reject the event if it is the case. The information from these three detector components are fed to a Global Level Trigger (GLT), which passes the physics event to the next level of trigger.

The L3 trigger is designed to reduce the output rate of 2 kHz from the L1 trigger to the logging rate of about 120 Hz without compromising the efficiencies of selecting physics events

[6]There is no Level 2 in *BABAR*.

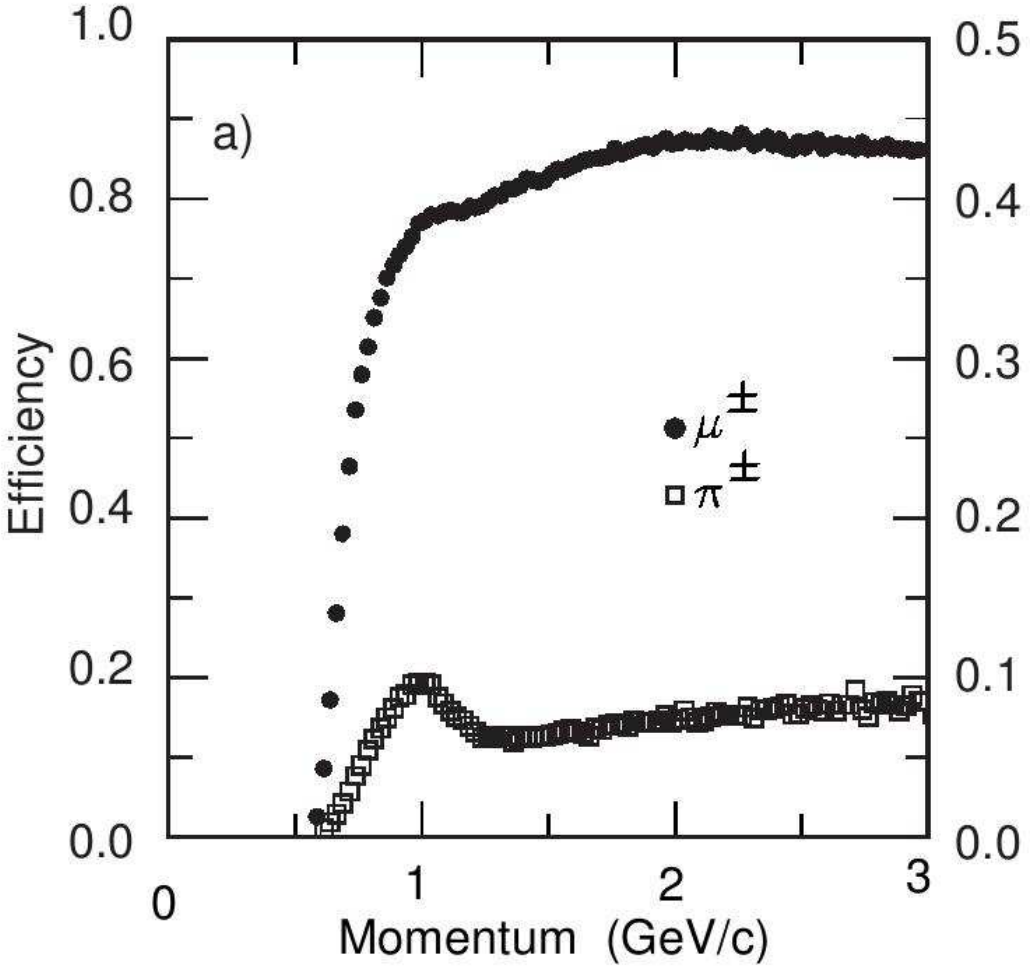

Figure 3.7: Identification efficiency of muons (scale on left) and pion misidentification probability (scale on right) in the IFR as a function of momentum in the laboratory frame [29].

[29]. It is an online application that partially reconstructs events based on information from the drift chamber and the calorimeter. This application is composed of reconstruction tools and filter modules. The L3 trigger can select $\tau^+\tau^-$, two photons, $B\overline{B}$ and $c\overline{c}$ events with high efficiency. The output of the L3 trigger is then stored for later analyses.

Chapter 4

Analysis

4.1 Analysis Strategy

The goal of this study is to measure the asymmetry between the decay rates of τ^+ and τ^-:

$$A_Q = \frac{N\left(\tau^+ \to \pi^+ K_S^0 \left(\geq 0\pi^0\right) \overline{\nu}_\tau\right) - N\left(\tau^- \to \pi^- K_S^0 \left(\geq 0\pi^0\right) \nu_\tau\right)}{N\left(\tau^+ \to \pi^+ K_S^0 \left(\geq 0\pi^0\right) \overline{\nu}_\tau\right) + N\left(\tau^- \to \pi^- K_S^0 \left(\geq 0\pi^0\right) \nu_\tau\right)} \tag{4.1}$$

The analysis uses the *BABAR* data sample, which contains 450 million τ pair events with approximately 1% of the τ leptons having a K_S^0 meson in the final state. The $K_S^0 \to \pi^+\pi^-$ decays with a branching fraction of $(69.20 \pm 0.05)\%$ and $K_S^0 \to \pi^0\pi^0$ with a branching fraction of $(30.69 \pm 0.05)\%$ [1].

Instead of selecting $\tau^- \to \pi^- K_S^0\, \nu_\tau$ decays exclusively, we select $\tau^- \to \pi^- K_S^0 \left(\geq 0\pi^0\right) \nu_\tau$ decays where any number of π^0 mesons in the final state are allowed. This has the benefit of enlarging the sample for analysis, which increases the sensitivity of the measurement. The presence of π^0 mesons in the final state does not affect the *CP* asymmetry.

Fig. 4.1 shows the topology of an event in the e^+e^- centre-of-mass frame. τ lepton pairs are produced back-to-back in the centre-of-mass frame. The decay products of each τ lepton can be easily separated by dividing the event into two hemispheres. One side of the event, called the signal hemisphere, contains a single track, a K_S^0 and any number of π^0 mesons. The other side of the event, called the tag hemisphere, is required to have a leptonic τ decay to suppress backgrounds from non-τ events. More details about the event selection are described in Sec. 4.3.

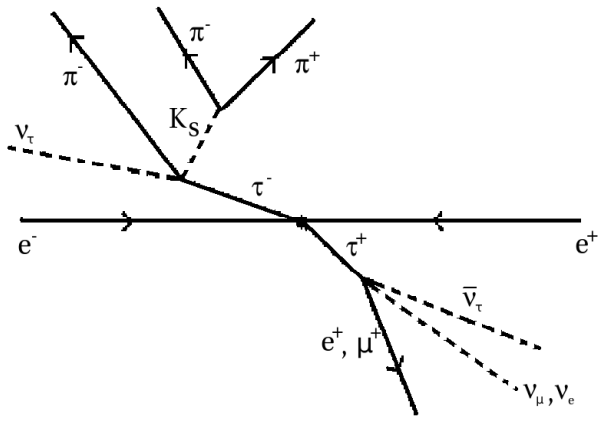

Figure 4.1: Schematic of $e^+e^- \to \tau^+\tau^-$, where a $\tau^- \to \pi^- K_S^0\, \nu_\tau$ decay ($K_S^0 \to \pi^+\pi^-$) in the signal hemisphere and a $\tau^- \to l^-\overline{\nu}_l\nu_\tau$ decay in the tag hemisphere. The definition of the hemispheres are defined in Sec. 4.3. Here $\ell^- = e^-, \mu^-$.

The τ leptons in the data are produced by the process $e^+e^- \to \tau^+\tau^-$. The *BABAR* sample is filtered with a set of selection criteria to maximize the number of signal events while minimizing the contribution from background events. Both on-peak and off-peak data are studied in this analysis, totalling to 476 fb^{-1} (see Table 4.1). On-peak data are events from e^+e^- collision at the $\Upsilon(4S)$ resonance (10.58 GeV) whereas off-peak data are recorded at a centre-of-mass energy of 10.54 GeV.

Sample type	Luminosity (fb^{-1})
Data	476
Monte Carlo	
$\tau^+\tau^-$	1014
uds	796
$c\overline{c}$	868
$\tau^\pm \to \pi^\pm K_S^0\, \pi^0\nu$	860

Table 4.1: Luminosities for data and Monte Carlo simulation.

The Monte Carlo sample consists of four sub-samples. The process $e^+e^- \to \tau^+\tau^-$ is modelled with kk2f [31], and Tauola is used to generate subsequent τ decays [32]. Monte Carlo sub-samples simulating $e^+e^- \to q\overline{q}$, where $q = u, d, s, c$, are generated using JETSET

[33] and are used for the study of $q\overline{q}$ background events. Final-state radiative effects are modelled with PHOTOS [34] and are included in all Monte Carlo sub-samples.

The signal modes are generated via $\tau^- \to K^{*-}\nu_\tau$ for the $\tau^- \to \pi^- K^0_S\ \nu_\tau$ decay and $\tau^- \to K_1(1270)^-\nu_\tau$ for the $\tau^- \to \pi^- K^0_S\ \pi^0\nu_\tau$. Other τ decay modes with K^0_S final states are modelled with a phase space distribution.

4.2 Preselection

A set of common selection criteria divides the data sample collected by *BABAR* into smaller samples suitable for different analyses by the entire collaboration. Two such sets of preliminary selection criteria are of particular importance for this study: the Tau11 and Tau1N selection criteria[1]. The Tau11 dataset is the nominal sample in this work whereas the Tau1N dataset is the control sample used for systematic studies. The labels 11 and 1N indicate there is one track in one hemisphere and either 1 or N (where $N = 3, 4, 5$) tracks in the other hemisphere. The hemispheres are divided according to the thrust axis[2]. Tracks originating from a displaced vertex, such as the pion tracks in $K^0_S \to \pi^+\ \pi^-$, are not counted in the skim definition (see Appendix B for the definition of the skims).

4.3 Selection

In this work the Tau11 sample is used, and additional selection criteria are applied in order to select events for this analysis. The following selections are applied to the sample:

1. Events are required to satisfy a set of selection criteria that are optimised to select decays with K^0_S in the final state, as well as to remove obvious sources of background

[1] Tau11 and Tau1N selection criteria are produced by the *BABAR* Tau/QED Analysis Working Group.

[2] The thrust axis is defined to be the axis parallel to the unit vector $\hat{A}$ that maximizes the quantity [35, 36]

$$\frac{\sum_{i=1}^{N} \left|\hat{A}\cdot\vec{P}_i\right|}{\sum_{i=1}^{N}\sqrt{\vec{P}_i\cdot\vec{P}_i}} \tag{4.2}$$

where P_i is the three-momentum of particle i to which the neutral cluster or the track is associated, and N is the number of neutral clusters and tracks in the event. This can give rise to a two-fold ambiguity because for any specific $\hat{A}$ that maximizes the quantity, so does $-\hat{A}$. By convention, the one with a positive z-component is taken to be $\hat{A}$. The magnitude of the thrust, or simply known as "thrust", is the maximum value of the expression given in Eq. 4.2.

events.

2. Two likelihood ratios are then used to further remove background events. The first likelihood ratio separates $e^+e^- \to q\overline{q}$ from $e^+e^- \to \tau^+\tau^-$ events and the second selects events with a K^0_S meson.

Particle identification is important in event selection, and is achieved through a set of particle selectors developed by the *BABAR* collaboration. The selectors for electrons, muons, charged kaons, K^0_S mesons and photon conversions used in the selection criteria are described in Appendix B.

4.3.1 Selection Criteria Prior to Likelihood

As described in Section 4.2, the hemisphere with a single track associated to the collision vertex and the K^0_S candidate is considered the signal hemisphere and the other side of the event is considered the tag hemisphere. The events in this analysis are tagged with an e or a μ lepton from a $\tau^- \to e^-\ \overline{\nu}_e\ \nu_\tau$ and $\tau^- \to \mu^-\ \overline{\nu}_\mu\ \nu_\tau$ decay, respectively (charge conjugation implied). They are referred to as the e-tag and μ-tag selected events.

Fig. 4.2 and 4.3 depict the distributions of the variables used in the selection criteria before the likelihood ratio selection criteria are applied[3]. Events included in the plots are required to satisfy all selection criteria except for the variable depicted. The red lines in the figures indicate the respective values of the selection criteria. For each variable, a plot with a linear vertical scale is shown on top and a semi-logarithmic plot is shown below. Although slight discrepancies between the data and Monte Carlo can be observed, they can be considered insignificant due to large errors in the branching fractions of some of the decay modes in this analysis [1]. The selection criteria prior to the likelihood ratio are listed below:

- Event:
  - The magnitude of the thrust of the event must be between 0.91 and 0.995 (see Fig. 4.2). The lower bound reduces $e^+e^- \to q\overline{q}$ backgrounds, and the upper bound eliminates Bhabha events from the sample, as the $e^+e^- \to \gamma\ e^+e^-$ events are highly back-to-back;

[3]All plots displayed in this chapter are for the e-tag sample unless specified otherwise. The plots for μ-tag can be found in Appendix D. Furthermore, the integrated luminosity of the Monte Carlo simulated sample is normalized to the data sample.

  - Topology: the event is divided into the tag and signal hemispheres using the 3-vector of the thrust. The signal hemisphere must contain three tracks – one track from a charged hadron, and two tracks from $K^0_S \to \pi^+ \pi^-$. The tag hemisphere must contain one track. (See Fig. 4.1 for a schematic of the topology);
  - Conservation of charge: all four tracks must have their electric charges added up to zero.

- Tag hemisphere:
  - Only one track is allowed;
  - The magnitude of the 3-momentum of the track in the centre-of-mass frame must be less than 4 GeV/c (see Fig. 4.2). This is to remove radiative Bhabha events and *uds* background;
  - The track must pass an electron or muon selector.

- Signal hemisphere:
  - None of the three tracks passes the electron selector selection criteria;
  - One $K^0_S \to \pi^+ \pi^-$ passes the K^0_S selector, after which the requirement on the invariant mass of the $\pi^+\pi^-$ system of the K^0_S candidate is tightened to be between 0.488 and 0.508 GeV/c^2 (see Fig. 4.3);
  - None of the oppositely charged pairs of tracks passes the photon conversion selector;
  - The number of neutral clusters in the signal hemisphere must be less than 9 (see Appendix B for a definition of neutral clusters);
  - The charged track associated to the e^+e^- collision vertex does not pass the charged kaon selector.

In addition to the above criteria, the mass of the hadronic final state ($\pi^- K^0_S \geq 0\pi^0$) is required to be less than the τ mass (1.8 GeV/c^2) to reduce $e^+e^- \to q\overline{q}$ background, especially background from charm resonances. The invariant mass of the hadronic system is calculated using the charged pion, the K^0_S meson and all π^0 mesons in the signal hemisphere. Figs. 4.4 and 4.5 show the invariant mass distributions for $\tau^- \to \pi^- K^0_S\,(\geq 0\pi^0)\,\nu_\tau$. Discrepancies

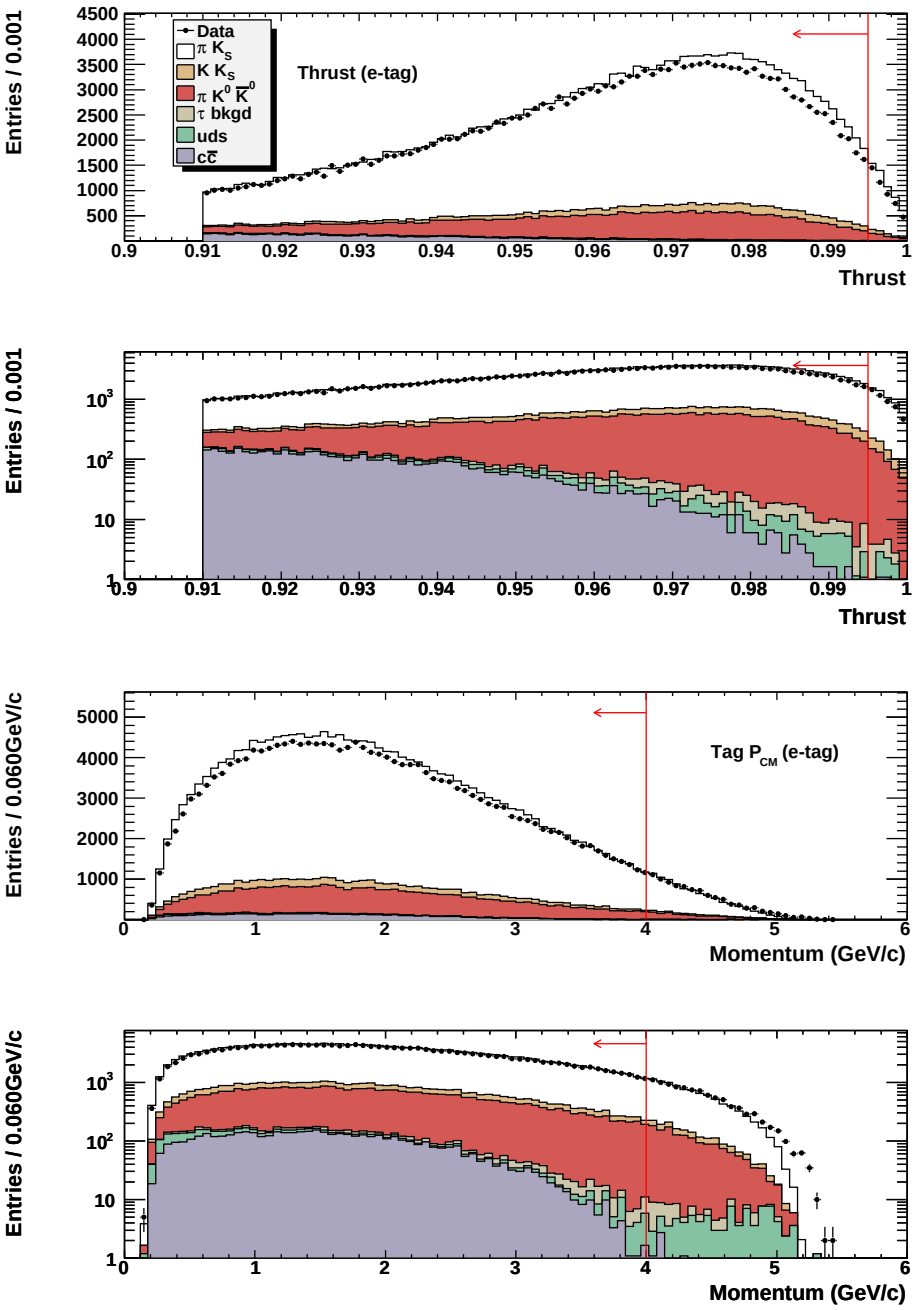

Figure 4.2: Thrust (top pair) and momentum of the tag particle in the tag hemisphere in the centre-of-mass frame (bottom pair) in the e-tag sample. Within both pairs of plots, the linear plot is displayed above and the semi-logarithmic plot is displayed below. Points represent data while the filled histograms represent Monte Carlo simulation, with white, orange and red representing the three signal modes. The red line indicates the value of the selection criterion, with the arrow indicating the region of the distribution kept for the analysis.

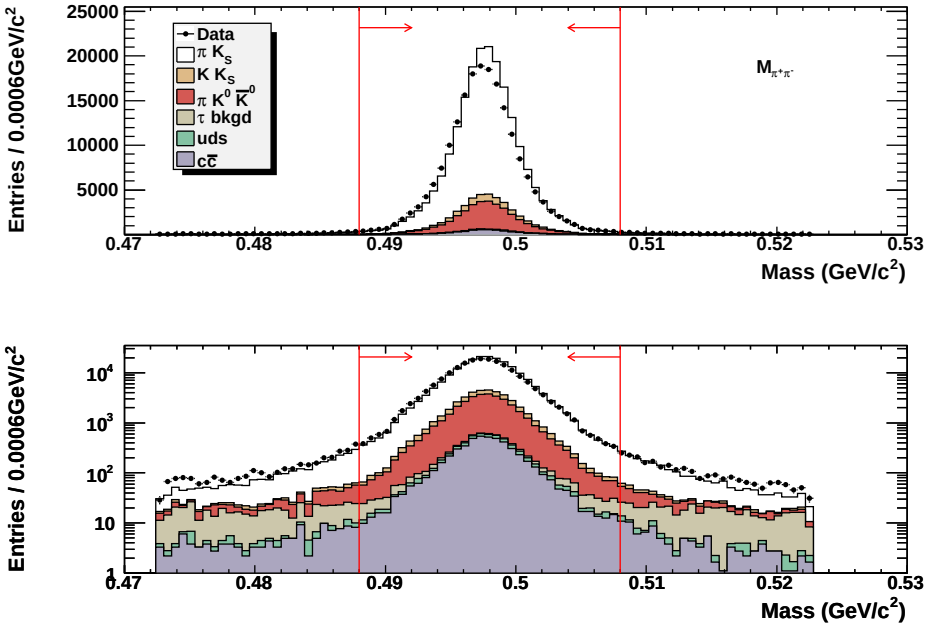

Figure 4.3: Invariant mass of $\pi^+\ \pi^-$ in $K^0_S \to \pi^+\ \pi^-$ in the e-tag sample. As in Fig. 4.2, the top plot is linear while the bottom plot is semi-logarithmic. The colour scheme of the histograms is the same as that in Fig. 4.2.

between data and Monte Carlo in the invariant mass distributions are due to resonances not included in the Monte Carlo. However, the discrepancies are found to be within the uncertainties of the corresponding branching fractions quoted in [1] and are hence statistically insignificant[4]. The number of π^0 mesons in the final state is counted with the following algorithm:

1. The invariant mass of all the pairs of neutral clusters in the signal hemisphere is calculated. Any pair is considered a π^0 candidate if the invariant mass of the two neutral clusters is between 0.115 and 0.150 GeV/c^2.

2. If there is more than one π^0 candidate, then the candidate with the invariant mass closest to that of a π^0 meson is considered the first π^0 in the signal hemisphere.

3. The neutral clusters used in the previous π^0 candidate are removed from the neutrals lists. The first two steps are repeated until there are no more π^0 candidates.

4. If there are more than three π^0 candidates reconstructed, only the first three π^0 meson candidates will go into the determination of the invariant mass of the hadronic system.

There is reasonable agreement between the data and MC for modes with a charged pion (see Fig. 4.4 and 4.5). There is no MC sample for the $\tau^- \to \pi^- K^0_S\ 2\pi^0\nu_\tau$ and $\tau^- \to \pi^- K^0_S\ 3\pi^0\nu_\tau$ decays as there is no evidence of these decay modes according to the PDG. The $\tau^- \to \pi^- K^0 \overline{K}^0 \nu_\tau$ decay contributes to the ($\pi^-\ K^0_S\ 2\pi^0$) invariant mass plot and this can be seen in Fig. 4.6 where we see evidence of the $K^0_S \to 2\pi^0$ decay. We also plotted the invariant mass of the $3\pi^0$ system in the ($\pi^-\ K^0_S\ 3\pi^0$) sample and see evidence for $\eta \to 3\pi^0$. There is no evidence for the $\tau^- \to \pi^- K^0_S \eta \nu_\tau$ from any other experiment.

4.3.2 Likelihood ratios

To further reduce the contamination from other τ decays and $e^+e^- \to q\overline{q}$ events, we have constructed two likelihood ratios. One likelihood ratio uses the properties of the K^0_S to identify events that contain a K^0_S. The second ratio uses the event properties to separate the $e^+e^- \to \tau^+\tau^-$ pair events from $e^+e^- \to q\overline{q}$ events.

[4]The difference in the shape of the distribution does not affect the measurement either, as the total number of events is counted, and the shape of the distribution does not come into play.

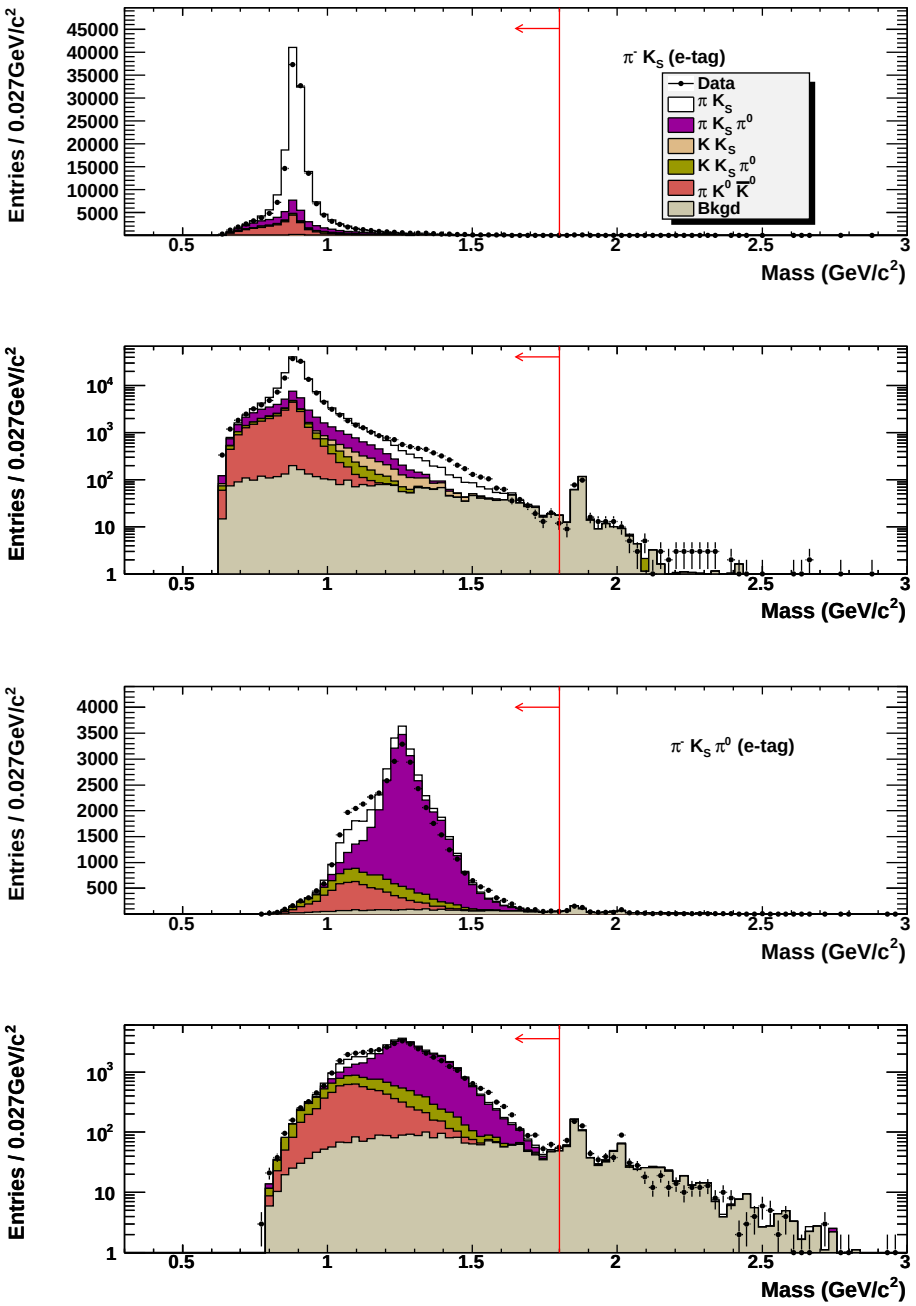

Figure 4.4: Invariant mass of the π^- K^0_S and π^- K^0_S π^0 systems for e-tagged events. Within each pair of plots, the top is the linear plot while the bottom is semi-logarithmic. All selection criteria except for the likelihood ratios have been applied.

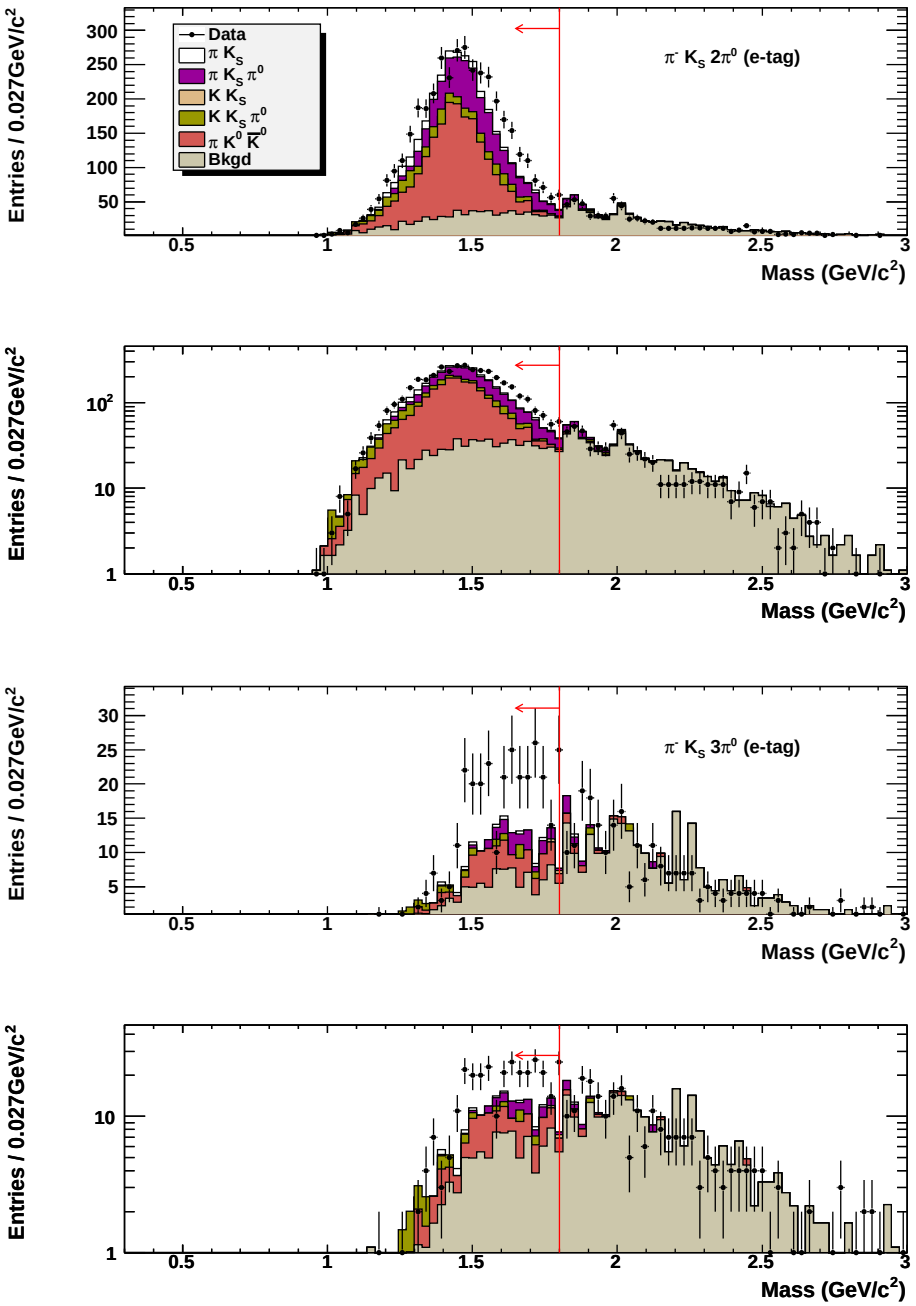

Figure 4.5: Invariant mass of the π^- K^0_S $2\pi^0$ and π^- K^0_S $3\pi^0$ systems for e-tagged events. Within each pair of plots, the top is the linear plot while the bottom is semi-logarithmic. All selection criteria except for the likelihood ratios have been applied.

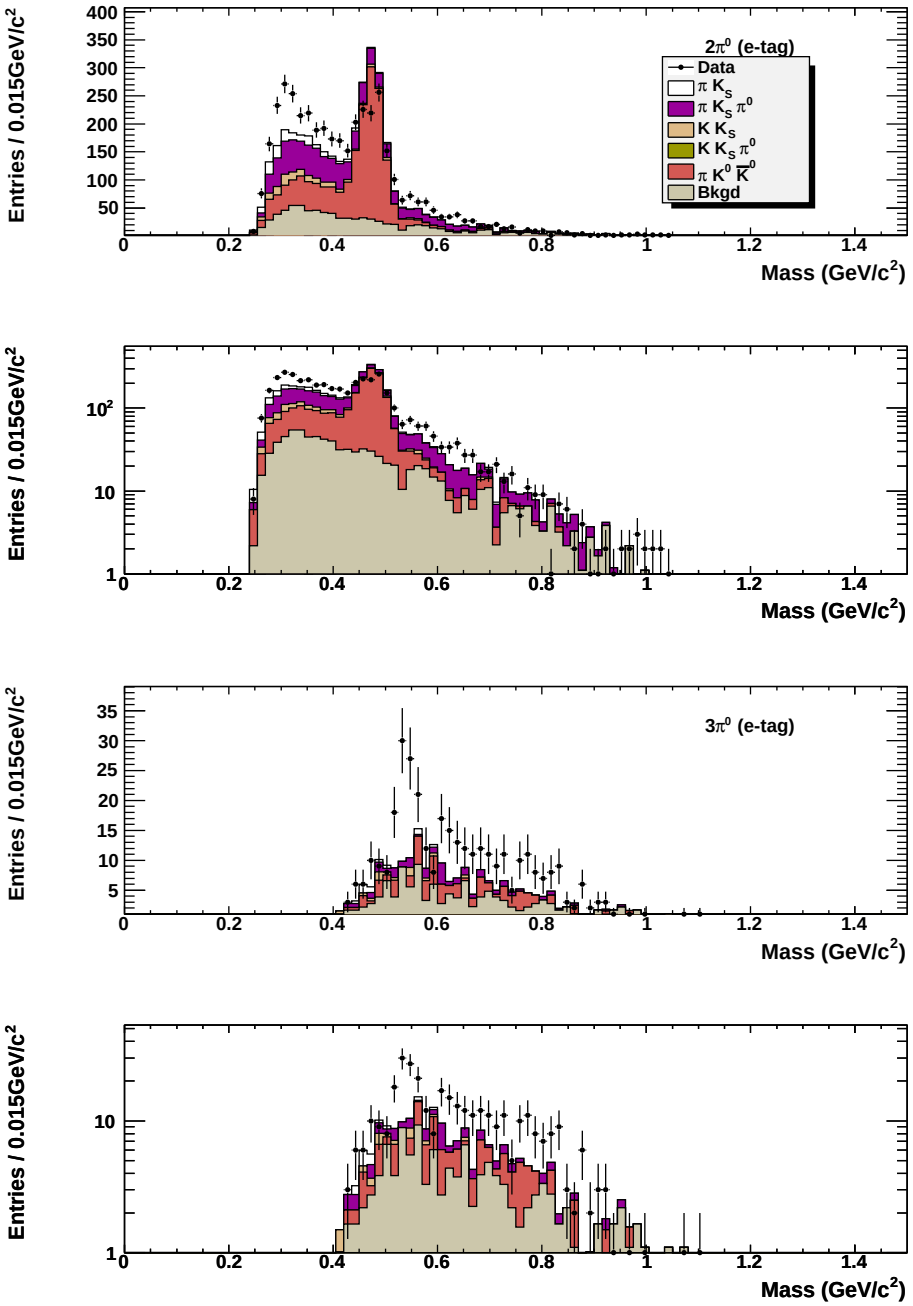

Figure 4.6: Invariant mass of the $2\pi^0$ in the decay $\tau^- \to \pi^- K_S^0\ 2\pi^0 \nu_\tau$ (top) and of the $3\pi^0$ in the decay $\tau^- \to \pi^- K_S^0\ 3\pi^0 \nu_\tau$ (bottom) for e-tagged events. All selection criteria except for the likelihood ratios have been applied.

We define an approximate likelihood as:

$$\mathcal{L}_{s(b)} = \prod_i p_{s(b)}\left(x_i\right) \tag{4.3}$$

where $p_{s(b)}\left(x_i\right)$ is the probability density function (PDF) for variable x_i for signal (background) events. The PDFs are generated using the Monte Carlo simulated events passing the previous selection criteria.

The probability of the event being a signal decay given measurement x_i, $P\left(sig|x_i\right)$, can be obtained through Bayes' Theorem:

$$\begin{aligned} P\left(sig|x_i\right) &= \frac{P\left(x_i|sig\right)P\left(sig\right)}{P\left(x_i\right)} \\ &= \frac{P\left(x_i|sig\right)P\left(sig\right)}{P\left(x_i|sig\right)P\left(sig\right)+P\left(x_i|bkg\right)P\left(bkg\right)} \\ &= \frac{P\left(x_i|sig\right)}{P\left(x_i|sig\right)+\frac{P(bkg)}{P(sig)}P\left(x_i|bkg\right)} \end{aligned} \tag{4.4}$$

We define a likelihood ratio function in terms of the approximate likelihoods:

$$y_{\mathcal{L}}\left(x_i\right) = \frac{\mathcal{L}_s\left(x_i\right)}{\mathcal{L}_s\left(x_i\right)+w\mathcal{L}_b\left(x_i\right)} \tag{4.5}$$

where w is the overall background-to-signal ratio estimated from Monte Carlo simulation. Note that $P(bkg)/P(sig)$ is replaced by w. This ratio obtained empirically is an estimate of the ratio between the prior probabilities of an event being a background $P(bkg)$ and it being a signal $P(sig)$.

The variables used to distinguish τ events from $e^+e^- \rightarrow q\overline{q}$ events are (see Figs. 4.7, 4.8 and 4.9):

- Number of neutral clusters in the tag hemisphere
- Number of neutral clusters in the signal hemisphere
- Magnitude of thrust
- Visible energy, defined as the sum of the energies associated with all neutral clusters and tracks of the event

- p_T of the event, calculated from all tracks and neutral clusters in both hemispheres

The variables used in the K_S^0 likelihood ratio are (see Figs. 4.10 and 4.11):

- Decay radius of the K_S^0, which is the distance from collision point to K_S^0 vertex projected in the plane transverse to the z-axis
- Invariant mass of the K_S^0
- 3-momentum of the K_S^0
- Cosine of the polar angle of the K_S^0

All variables used in the K_S^0 likelihood ratio are taken in the laboratory frame of reference.

A probability distribution function (PDF) is generated for each of the variables using the MC samples for τ signal decays and the background (other τ decays and $e^+e^- \to q\overline{q}$). The two likelihood ratios are constructed using the method described above. We require that events have the τ and K_S^0 likelihood ratios greater than 0.2 and 0.4, respectively (see Fig. 4.12), in order to optimize the purity of the sample and the data yield. The selection criteria on the likelihood ratios are varied around their nominal values, and no significant variation in the resulted asymmetry in the Monte Carlo simulated sample is found.

4.3.3 Results

The results after all selection criteria for e- and μ-tagged samples are applied are presented in Tables 4.2 and 4.3 respectively, where the errors are statistical only. The asymmetry is defined by the following:

$$A_Q = \frac{N_+ - N_-}{N_+ + N_-} \tag{4.6}$$

where N_+ (N_-) is the number of τ^+ (τ^-) decays. The asymmetry in the Monte Carlo simulation is expected to be zero, as *CP* violation is not included in the simulation. In addition, the asymmetries in data and Monte Carlo simulated samples as presented in Tables 4.2 and

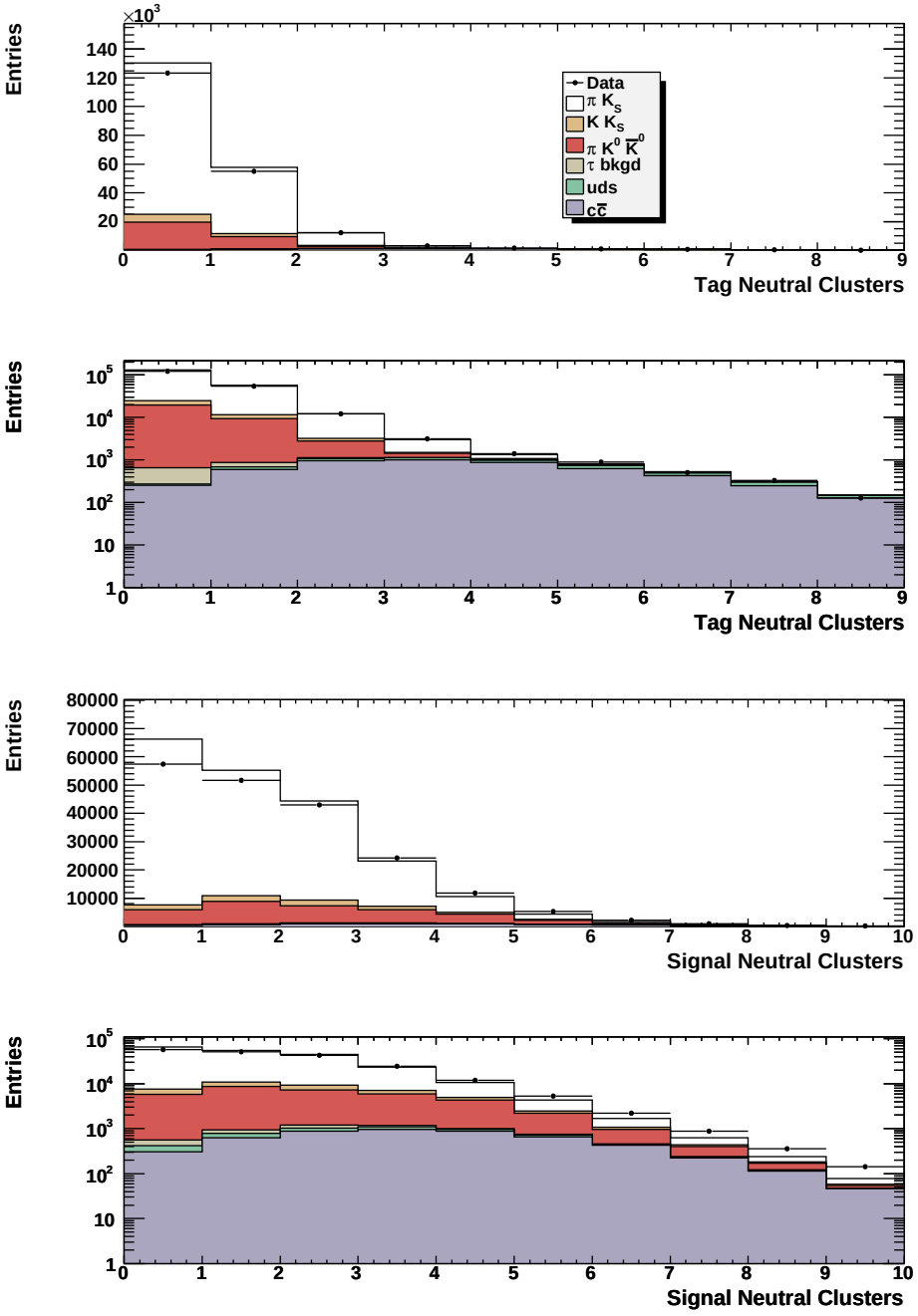

Figure 4.7: Numbers of neutral clusters in the tag and signal hemispheres in the e-tag sample. These two variables are used in the determination of the approximate likelihood separating $e^+e^- \to \tau^+\tau^-$ events from $e^+e^- \to q\overline{q}$ events. All selection criteria except for the likelihood ratios have been applied.

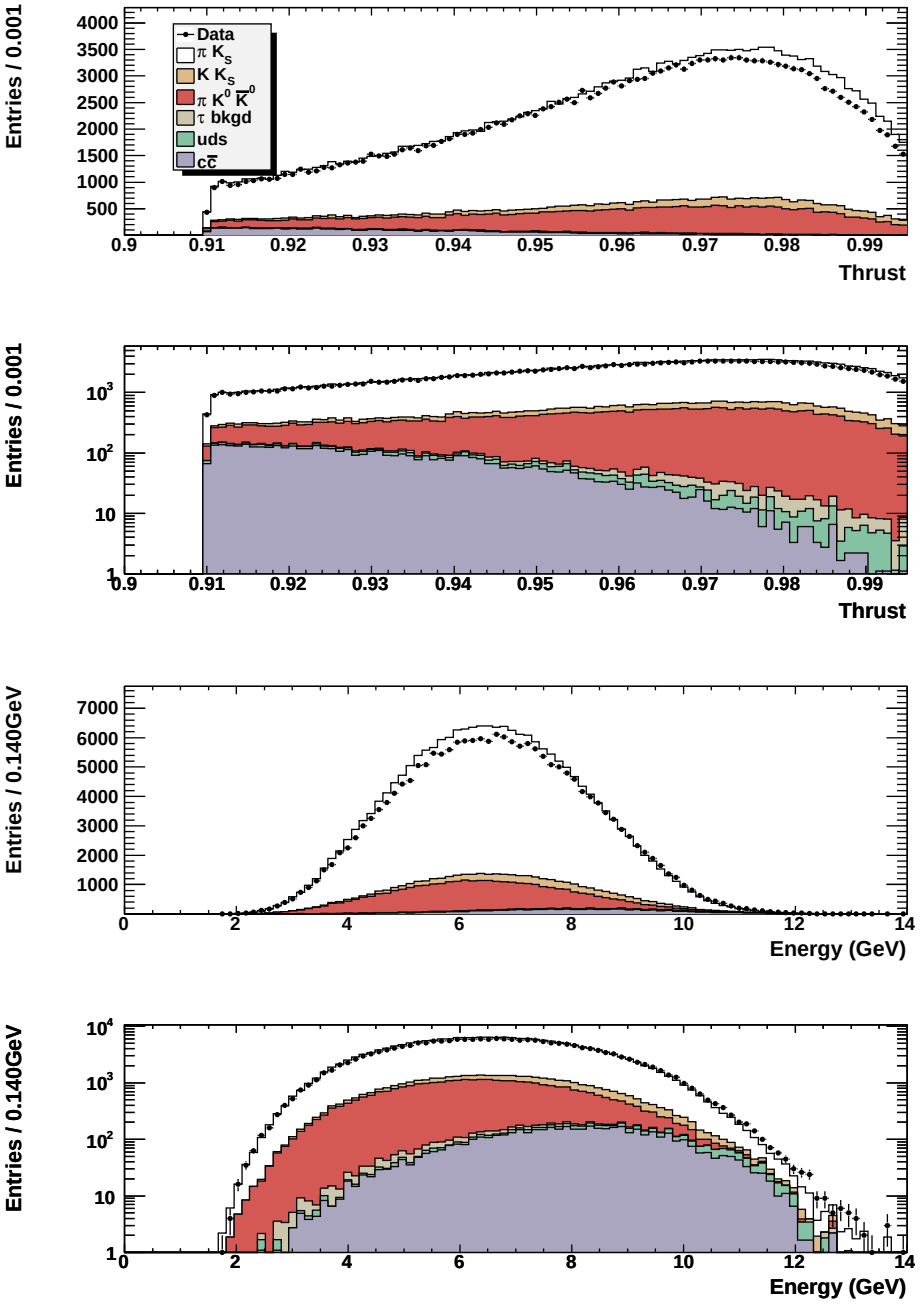

Figure 4.8: Event thrust and visible energy in the e-tag sample. These two variables are used in the determination of the approximate likelihood separating $e^+e^- \to \tau^+\tau^-$ events from $e^+e^- \to q\overline{q}$ events. All selection criteria except for the likelihood ratios have been applied.

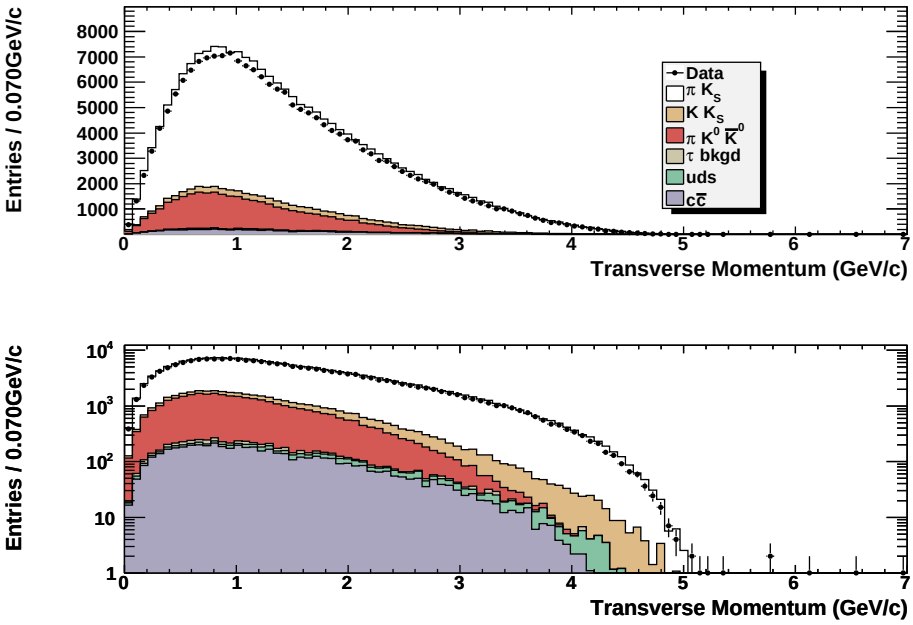

Figure 4.9: Transverse component of the total momentum of all tracks and neutral clusters in the e-tag sample. This variable is used in the determination of the approximate likelihood separating $e^+e^- \to \tau^+\tau^-$ events from $e^+e^- \to q\overline{q}$ events. All selection criteria except for the likelihood ratios have been applied.

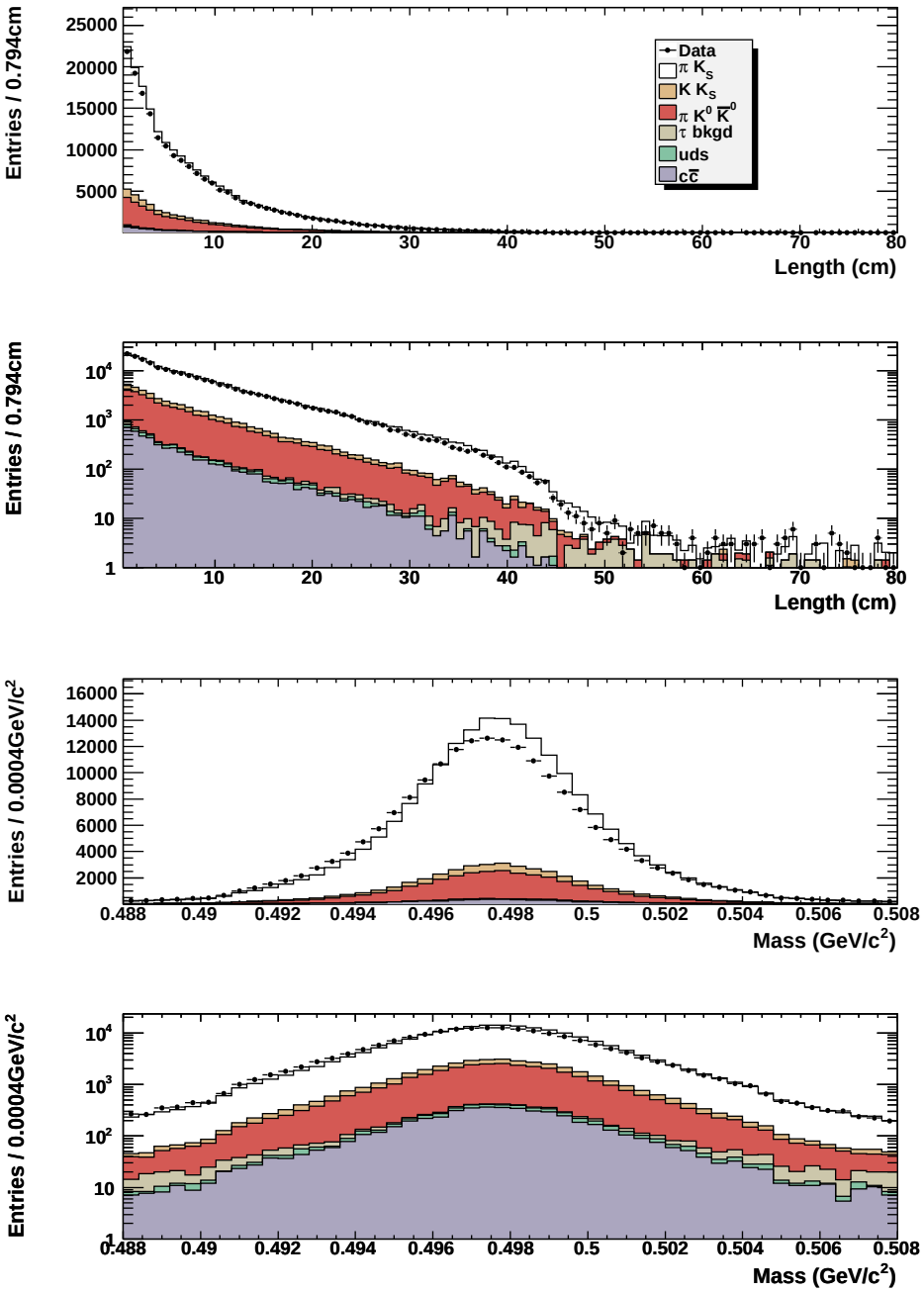

Figure 4.10: K^0_S decay length in the xy-plane and invariant mass of $\pi^+\,\pi^-$ in $K^0_S \to \pi^+\,\pi^-$ in the e-tag sample. These two variables are used in the determination of the approximate likelihood identifying events with K^0_S in the final state. All selection criteria except for the likelihood ratios have been applied.

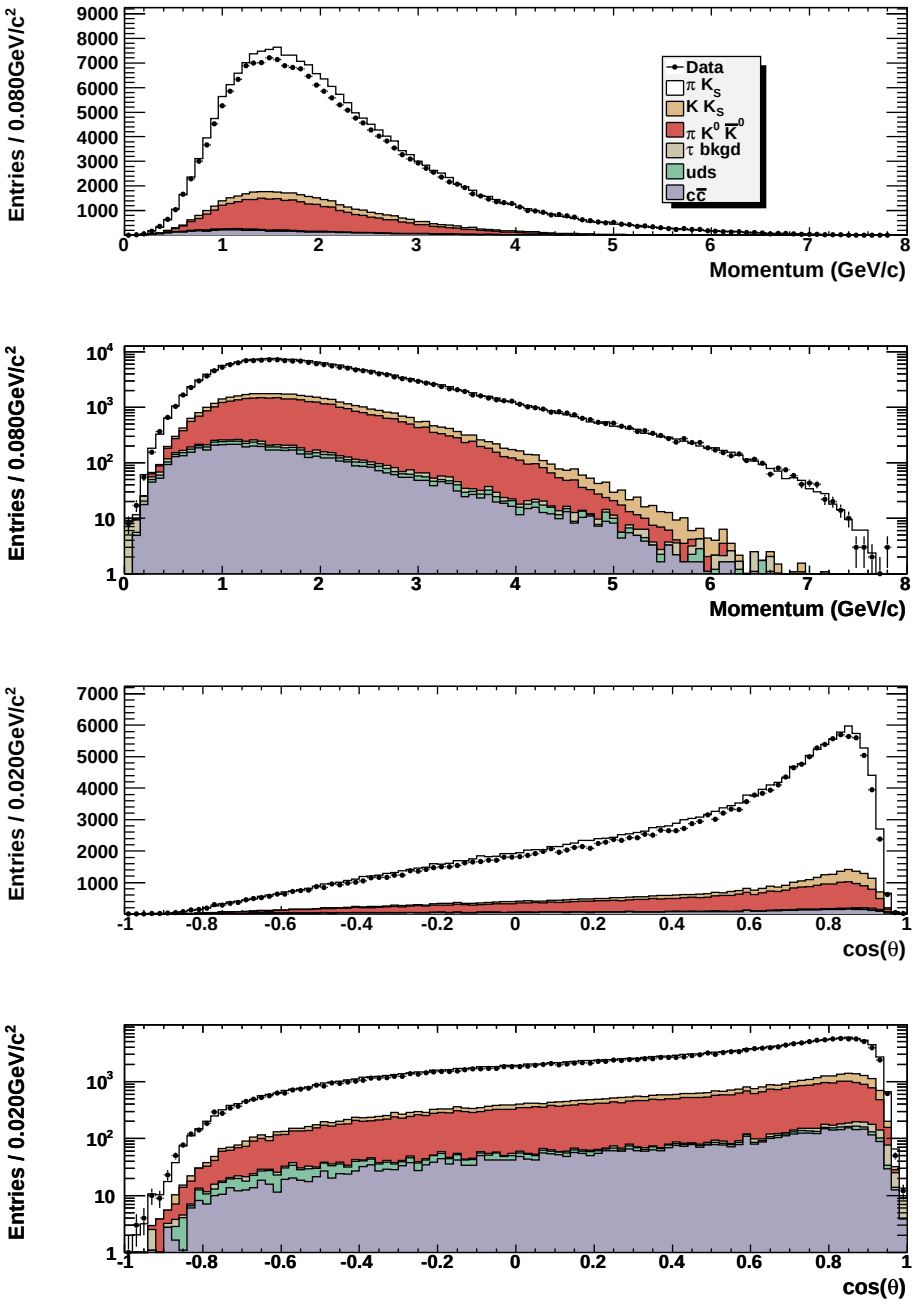

Figure 4.11: Momentum of the K_S^0 and cosine of the polar angle of the K_S^0, both in the laboratory frame in the e-tag sample. These two variables are used in the determination of the approximate likelihood identifying events with K_S^0 in the final state. All selection criteria except for the likelihood ratios have been applied.

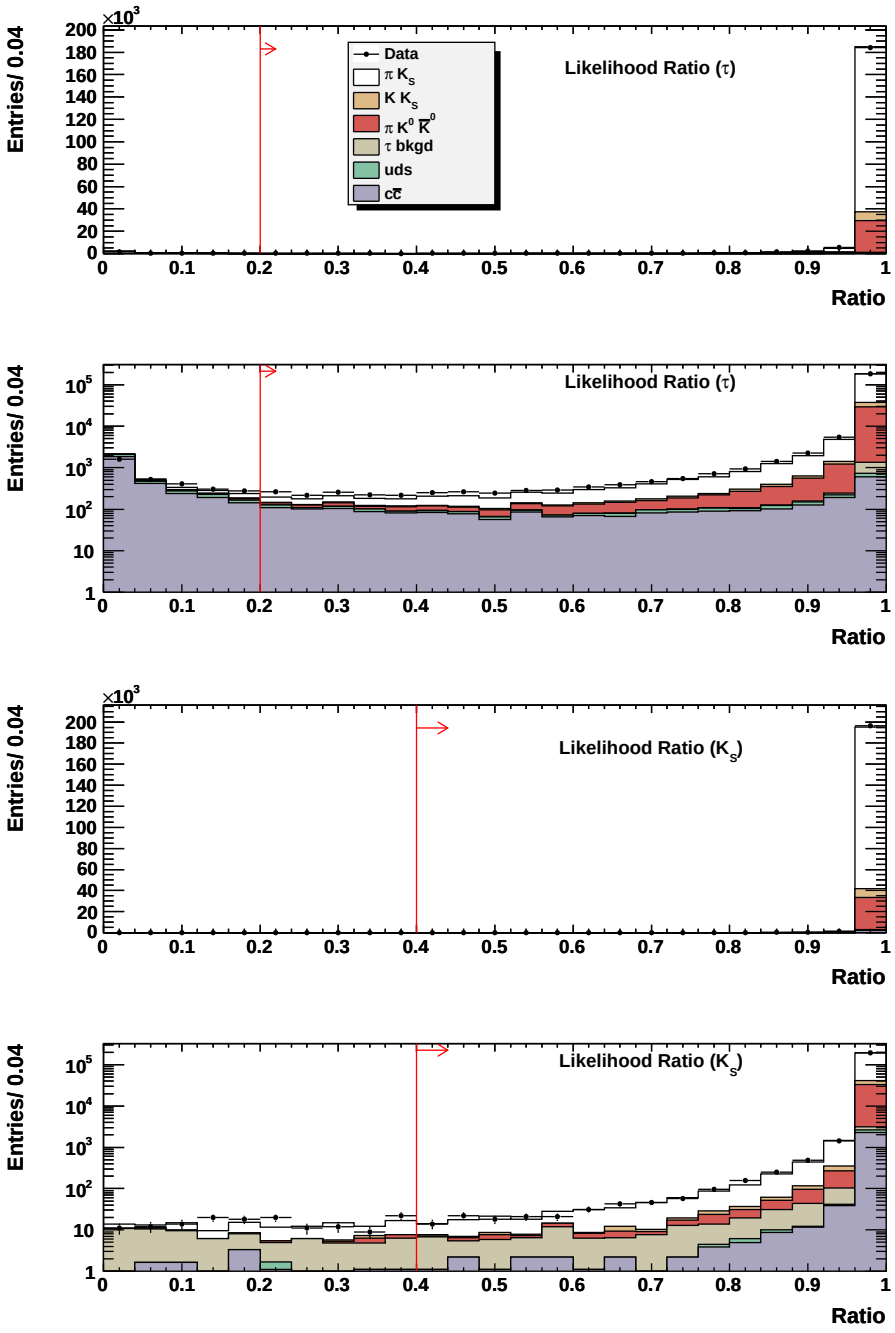

Figure 4.12: Likelihood ratios to distinguish τ events from $e^+e^- \to q\overline{q}$ events (top) and τ decays with K^0_S from those without (bottom) (e-tag sample).

4.3 are not background-corrected[5]. The treatment of background events will be explained in Chapter 5.

Type	Events	% of MC	Asymmetry (%)
Data	199064±446		-0.31±0.23
MC	196532±283	100	-0.16 ± 0.14
Signal	193122±279	98.3±0.2	
$\tau^- \to \pi^- K^0_S (\geq 0\pi^0)\, \nu_\tau$	154082±244	78.4±0.2	0.04 ± 0.16
$\tau^- \to K^- K^0_S (\geq 0\pi^0)\, \nu_\tau$	8300±62	4.22±0.03	-4.17 ± 0.75
$\tau^- \to \pi^- K^0 \overline{K}^0 \nu_\tau$	30740±121	15.64±0.07	-0.14 ± 0.39
Background	3411±43	1.74±0.02	
τ background	664±18	0.338±0.009	-4.0 ± 2.7
uds	398±15	0.203±0.008	-9.0 ± 3.9
$c\overline{c}$	2349±36	1.20±0.02	3.1 ± 1.5
Purity (%)		98.3±0.2	

Table 4.2: Numbers of events after all selections are applied to e-tag sample. The last column lists the asymmetries in different MC subsamples, with the asymmetry for "MC" being the overall asymmetry with all the subsamples combined. The data asymmetry does not have any corrections applied. Errors are statistical only.

[5]The errors for the Monte Carlo simulation in Tables4.2 and 4.3 are scaled with the luminosities, and so differ from the statistical uncertainty in the data despite their similar sizes

Type	Events	% of MC	Asymmetry (%)
Data	140602±375		-0.10±0.27
MC	138415±238	100	-0.02 ± 0.17
Signal	134443±233	97.1±0.2	
$\tau^- \to \pi^- K_S^0 (\geq 0\pi^0)\, \nu_\tau$	107104±203	77.4±0.2	0.18 ± 0.19
$\tau^- \to K^- K_S^0 (\geq 0\pi^0)\, \nu_\tau$	5568±51	4.02±0.04	-2.39 ± 0.91
$\tau^- \to \pi^- K^0 \overline{K}^0 \nu_\tau$	21771±102	15.73±0.08	0.22 ± 0.47
Background	3971±47	2.87±0.03	
τ background	419±14	0.30±0.01	3.4 ± 3.3
uds	1676±32	1.21±0.02	-8.5 ± 1.9
$c\overline{c}$	1877±32	1.36±0.02	-0.94 ± 1.71
Purity (%)		97.1±0.2	

Table 4.3: Numbers of events after all selections are applied to μ-tag sample. The last column lists the asymmetries in different MC subsamples, with the asymmetry for "MC" being the overall asymmetry with all the subsamples combined. The data asymmetry does not have any corrections applied. Errors are statistical only.

Chapter 5

Discussion

In Tables 4.2 and 4.3, the "raw" asymmetries were presented. These asymmetries, which are $(-0.31 \pm 0.23)\%$ for the e-tag and $(-0.10 \pm 0.27)\%$ for the μ-tag, are based on the total number of events that passed the selection criteria (the errors are purely statistical). However, these numbers need to be corrected for backgrounds and detector effects that are not modelled in the Monte Carlo simulation. Further, systematic errors need to be evaluated. The corrections and the determination of the systematic errors are performed in the order listed below. Each step is discussed in more detail in this section. The effect of each step on the measurement is summarized in Table 5.1.

1. Background correction: the small background components from $e^+e^- \to q\overline{q}$ and other τ decays are subtracted to obtain the asymmetry for the $\pi^- K^0_S \geq 0\pi^0$, $K^- K^0_S \geq 0\pi^0$ and $\pi^- K^0 \overline{K}^0$ modes. The size of the background components is estimated using Monte Carlo simulation.

2. K^0-$\overline{K}^0$ dilution correction factor: K^0 and $\overline{K}^0$ interact with the material in the detector at different rates due to the different nuclear interaction cross sections. The different rates can give rise to a charge asymmetry. This effect is not modelled in the Monte Carlo simulation and a correction is applied to the asymmetry.

3. Systematic errors: the uncertainties due to possible detector biases, background subtraction and the dilution correction factor are evaluated.

4. Average: a weighted average is used to combine the asymmetries measured in the e-tag and μ-tag samples.

5. Final result after "unfolding": the asymmetry obtained thus far is based on a sample including $\tau^- \to K^- K_S^0 (\geq 0\pi^0)\, \nu_\tau$ and $\tau^- \to \pi^- K^0 \overline{K}^0 \nu_\tau$ decays. To obtain the asymmetry pertaining to the $\tau^- \to \pi^- K_S^0 (\geq 0\pi^0)\, \nu_\tau$ decay mode alone, one must take into account how the $\tau^- \to K^- K_S^0 (\geq 0\pi^0)\, \nu_\tau$ and $\tau^- \to \pi^- K^0 \overline{K}^0 \nu_\tau$ modes affect the asymmetry.

Asymmetry	e-tag (%)	μ-tag (%)
Raw	-0.31±0.23(stat.)	-0.10±0.27(stat.)
Background correction	-0.32±0.22(stat.)	-0.05±0.27(stat.)
Dilution correction	-0.46±0.22(stat.)	-0.19±0.27(stat.)
Systematic errors	-0.46±0.23±0.13	-0.19±0.27±0.10
Average	-0.34±0.18±0.08	
Final result after "unfolding"	-0.45±0.24±0.11	

Table 5.1: Summary of asymmetries presented in the sequence in which the corrections are applied and the errors are included. "Raw" is the asymmetry obtained from the number of events passing selection criteria; "Background correction" is the asymmetry obtained after background events are subtracted; "Dilution correction" is the asymmetry after nuclear interaction effects of K^0 and $\overline{K}^0$ with the detector material is taken into account; "Systematic errors" is the inclusion of uncertainties due to detector effects and background subtraction; "Averaged" is the average of the e-tag and μ-tag results; and "Final result after 'unfolding' " is the asymmetry for the exclusive decay mode $\tau^- \to \pi^- K_S^0 (\geq 0\pi^0)\, \nu_\tau$. The uncertainties quoted in the first three rows are statistical only whereas the remaining three rows show both the statistical and systematic uncertainties.

5.1 Background subtraction

The selected sample has a small number of background events. The Monte Carlo simulation predicts the background to be dominated by $e^+e^- \to q\overline{q}$ events with a smaller component from $e^+e^- \to \tau^+\tau^-$ decays that do not contain a K_S^0 in the final state (see Tables 4.2 and 4.3). At this stage, the $\tau^- \to K^- K_S^0 (\geq 0\pi^0)\, \nu_\tau$ and $\tau^- \to \pi^- K^0 \overline{K}^0 \nu_\tau$ events are not considered to be background. These decays are treated separately in Section 5.7.

The background-subtracted asymmetry is given by:

$$A_{Q,sub} = \frac{(N_+ - B_+) - (N_- - B_-)}{(N_+ - B_+) + (N_- - B_-)} \tag{5.1}$$

where $N_\pm$ and $B_\pm$ are the number of $\tau^\pm$ decays in the data and the number of $\tau^\pm$ background events in the Monte Carlo simulation, respectively. N_+ for e-tag (μ-tag) is 99222 (70233) whereas N_- for e-tag (μ-tag) is 99842 (70369).

The background is estimated from the Monte Carlo simulation and the results are given in Tables 4.2 and 4.3. The accuracy of the background prediction of the Monte Carlo simulation is checked by comparing the number of data and MC events in rejected regions $(0 - 0.1)$ of the two likelihood ratios (see Figs. 4.12 and D.11), which is dominated by background events. The ratio of data to Monte Carlo events (data/MC ratio) for the likelihood ratio that separates $e^+e^- \to q\overline{q}$ events from $e^+e^- \to \tau^+\tau^-$ events is found to be 0.81±0.02 for e-tag and 0.49±0.01 for μ-tag (see Table 5.2). The same procedure is repeated for the likelihood ratio that selects K^0_S events and we find that the data/MC ratios are consistent with unity (with a large statistical uncertainty).

The overall data/MC ratios are used to correct the number of background events predicted by the Monte Carlo. The corrected background event numbers are $B^e_- = 1393 \pm 79$ ($B^\mu_- = 1120 \pm 65$) for τ^- decays and $B^e_+ = 1401 \pm 74$ ($B^\mu_+ = 1055 \pm 74$) for τ^+ decays in the e-tag (μ-tag) sample, where the errors include the statistical uncertainties in the Monte Carlo as well as the uncertainties in the data/MC ratios. The corrected background event numbers are then subtracted from number of events selected in the data sample. The background-corrected asymmetries are found to be (-0.32±0.22)% and (-0.05±0.27)% for e- and μ-tag, respectively, where the errors are statistical (see Table 5.1).

The systematic uncertainty on the asymmetry due to the background is estimated using the Monte Carlo statistical error (see Tables 4.2 and 4.3) and the uncertainty in the data/MC ratio (see Table 5.2). The statistical uncertainty in the Monte Carlo simulation only constitutes a small part of this error in the asymmetry ($\approx 0.02\%$ for both tags) whereas the uncertainty in the data/MC correction factor is much more significant. The correction factor was varied for each charge and the maximum change in the value of the asymmetry was taken as the systematic error. The total systematic error on the asymmetry due to the background is estimated to be 0.05% and 0.06% for the e-tag and μ-tag samples, respectively. The background-related systematic errors are combined with the other systematic errors in

Tag	Data to Monte Carlo Ratio		
	τ^- decays	τ^+ decays	Overall
$\tau - q\bar{q}$ Likelihood			
e	0.82±0.03	0.79±0.03	0.81±0.02
μ	0.53±0.02	0.47±0.02	0.49±0.01
K_S^0 Likelihood			
e	1.1±0.3	0.9±0.2	0.9±0.2
μ	1.0±0.4	1.0±0.4	1.0±0.3

Table 5.2: The ratios of data to Monte Carlo simulated events for the vetoed region of the likelihood ratios. The "τ-$q\overline{q}$ Likelihood" separates $e^+e^- \rightarrow q\overline{q}$ background events from $e^+e^- \rightarrow \tau^+\tau^-$ events whereas the "K_S^0 Likelihood" selects K_S^0 events.

Section 5.4.

5.2 K^0-$\overline{K}^0$ nuclear interaction

It has been suggested [37] that there can be a "dilution" effect to the asymmetry due to the difference in nuclear interaction cross sections for K^0 and $\overline{K}^0$ [1]. This is because the measurement of the charge asymmetry is intrinsically linked with the asymmetry of a τ lepton decaying into a K^0 or a $\overline{K}^0$ meson:

$$A = \frac{\Gamma\left(\tau^+ \to \pi^+ K^0 \left(\geq 0\pi^0\right) \nu_\tau\right) - \Gamma\left(\tau^- \to \pi^- \overline{K}^0 \left(\geq 0\pi^0\right) \nu_\tau\right)}{\Gamma\left(\tau^+ \to \pi^+ K^0 \left(\geq 0\pi^0\right) \nu_\tau\right) + \Gamma\left(\tau^- \to \pi^- \overline{K}^0 \left(\geq 0\pi^0\right) \nu_\tau\right)} \tag{5.2}$$

If the K^0 and $\overline{K}^0$ mesons are detected with different efficiencies, then the asymmetry measurement will be affected. A correction factor needs to be applied to the asymmetry measurement to account for this effect.

The asymmetry due to the interaction of neutral kaons with detector material (A_D) is described in full detail in Appendix E and is calculated to be:

$$A_D = \frac{P_{\overline{K}^0} - P_{K^0}}{2}$$

where $P_{K^0}(P_{\overline{K}^0})$ is the probability of a K^0 ($\overline{K}^0$) interacting with the detecting material. The probabilities are dependent on the nuclear interaction cross section of the neutral kaon at a specific momentum, the amount of detector material the kaon traverses before decaying, and the polar angle of the trajectory of the kaon. A_D is determined on an event-by-event basis to be $(0.135 \pm 0.013 \pm 0.026)\%$ for the e-tag and $(0.137 \pm 0.015 \pm 0.017)\%$ for the μ-tag, where the first error is statistical and the second is systematic. The statistical uncertainty is due to the fact that the interaction probability is evaluated on an event-by-event basis whereas the systematic uncertainty is dominated by uncertainties in the kaon-nucleon interaction cross sections. This "dilution" asymmetry has to be subtracted from the measurement. The total error on A_D is included in the systematic errors (see Table 5.3).

[1] This effect is not accounted for in the Monte Carlo simulation because the Monte Carlo simulation projects the neutral kaon onto the K_S^0/K_L^0 eigenspace at the production point [37].

5.3 Detector uncertainties

It is necessary to establish that there are no charge-dependent detector or selection criteria that would result in a bias in the asymmetry measurement. Biases can arise from a charge asymmetry in the interactions of particles from the decay with the detector material. Fortunately there is a sample of $\tau^- \to \pi^-\pi^-\pi^+\nu_\tau$ decays, which is approximately 30 times larger than the signal sample. The $\tau^- \to \pi^-\pi^-\pi^+\nu_\tau$ sample contains a negligible number of K^0_S mesons that decay to a π^+ π^- pair, as the three tracks are required to originate from the e^+e^- beam spot. The 3-prong τ decays are not expected to give rise to any *CP* asymmetry induced by new physics processes (see, for example, [38] and [39]).

Appendix C contains more details regarding the control sample study. The selection criteria for the control sample are similar to those used to select the signal sample. However, one of the key differences between the control sample and the signal sample is the requirement in the former that the three tracks in the signal hemisphere originate from the e^+e^- collision vertex. As a result, K^0_S decays are highly suppressed in the control sample due to its displaced decay vertex, and any K^0_S selection criteria in the signal sample are not implemented in the control sample.

One of the challenges with the e-tag control sample is the contamination of radiative Bhabha events, where a photon converts to an e^+e^- pair. This can give rise to a spurious source of charge asymmetry due to the asymmetric e^+e^- beam energies. Specifically, the e^- beam will be more likely to radiate a photon that is energetic enough to produce a detectable pair of particles. The pair of charged particles will then travel preferentially in the direction of the e^- beam, resulting in the e^- being more likely to be identified as the tag particle. In principle radiative dimuon events can give the same effect in the μ-tag sample, but since the radiative power for bremsstrahlung is inversely proportional to m^4 (for particles with $d\vec{v}/dt \perp \vec{v}$) or m^6 (for particles with $d\vec{v}/dt \parallel \vec{v}$), the effect is suppressed. The radiated photon has a low invariant mass, so the K^0_S invariant mass window is effective in excluding radiative Bhabha events in the nominal sample. However, no mass cut is applied in the control sample. Therefore, additional selection criteria are applied to the control sample to suppress background of Bhabha events.

The detector uncertainty is taken to be the difference in the asymmetries between the data and the Monte Carlo simulation control samples. The asymmetries in the e-tag data and Monte Carlo simulated control samples are $(-0.065 \pm 0.039)\%$ and $(0.061 \pm 0.029)\%$,

respectively. The asymmetries in the data and Monte Carlo simulation are slightly inconsistent with each other. Rather than taking the uncertainties of the asymmetries as the systematic error, we take the difference (0.12%) as the systematic error. Since the asymmetries in the data and Monte Carlo simulated control samples are consistent with each other for the μ-tag sample ($(0.115 \pm 0.044)\%$ and $(0.105 \pm 0.033)\%$ respectively), the sum of the statistical uncertainties (0.08%) is taken to be the systematic uncertainty.

5.4 Systematic uncertainties

A summary of the systematic uncertainties of this study is presented in Table 5.3. Luminosity, tracking efficiency and particle identification do not introduce additional systematic uncertainties. Luminosity enters in both the numerator and the denominator in the expression for asymmetry and will hence cancel out, so uncertainties in the luminosity do not contribute to the uncertainty in the asymmetry. Tracking efficiency does not introduce additional systematic uncertainties because there are four tracks in the events, two for each charge. Any biases introduced by particle identification will also be present in the control sample, so uncertainties due to particle identification are not included to avoid double-counting.

Source	Uncertainty	
	e-tag	μ-tag
Background	0.05	0.06
K^0-$\overline{K}^0$ Nuclear Interaction	0.03	0.02
Detector Uncertainty	0.12	0.08
Total	0.13	0.10

Table 5.3: Systematic Uncertainties. Uncertainties are in the same units as the asymmetry.

5.5 Average asymmetry

The e-tag and μ-tag asymmetries are combined by a weighted average. Since the asymmetries in the two samples are expected to have the same central value, a weighted average based

on the uncertainties in the two asymmetries can be used. The average asymmetry A_{avg} can be determined from the asymmetries of the two samples A_i $(i = 0, 1)$ and the corresponding uncertainties σ_i by the following (see, for example, [40]):

$$A_{avg} = \frac{\sum_i A_i/\sigma_i^2}{\sum_i 1/\sigma_i^2} \tag{5.3}$$

while the uncertainty in the average is related to the uncertainties in the individual samples by the following:

$$\frac{1}{\sigma_{avg}^2} = \sum_i \frac{1}{\sigma_i^2} \tag{5.4}$$

The systematic errors for the e-tag and μ-tag samples are uncorrelated, except for uncertainties in the dilution factor attributed to kaon-nucleon interaction cross sections. However, the uncertainty from kaon-nucleon interaction cross sections only constitutes a small part of the overall systematic uncertainty, and their correlations can hence be neglected.

5.6 Cross-checks

A series of cross-checks have been performed to ensure that there are no selection biases or detector effects that need to be taken into account.

5.6.1 Asymmetry from $e^+e^- \to q\overline{q}$ background

To check whether the $q\overline{q}$ background events would introduce any asymmetry, one can look at the events in the vetoed region of the τ-$q\overline{q}$ likelihood ratio. It is found that the asymmetry in the vetoed region (likelihood ratio between 0 and 0.2 in the top plot in Fig. 4.12) for the e-tag is consistent with zero in both data $((0.6 \pm 1.7)\%)$ and MC samples $((0.4 \pm 1.2)\%)$. The same is found for the μ-tag: $(-4.8 \pm 2.0)\%$ and $(-1.3 \pm 1.1)\%$ for the data and Monte Carlo simulated samples, respectively.

The value of the likelihood ratio cut does not seem to have a significant impact on the asymmetry. The value of the cut is varied by 0.1 around where it is applied, and a maximum deviation of 0.07% (0.03%) is seen for the $e(\mu)$-tag sample. This is less than the statistical uncertainty associated with the $e^+e^- \to q\overline{q}$ background and can be neglected.

5.6.2 Asymmetry from $e^+e^- \to \tau^+\tau^-$ background

Since the τ background constitutes only (0.338±0.009)% of the e-tag sample and (0.30±0.01)% of the μ-tag sample after all selection criteria have been applied, its impact on the overall charge asymmetry is limited. No systematic uncertainty due to the $e^+e^- \to \tau^+\tau^-$ background asymmetry is assigned. Furthermore, variations in the cut value at the K^0_S likelihood ratio do not seem to produce any significant impact on the overall asymmetry: the maximum deviation in the overall asymmetry due to these variations is found to be 0.06% and 0.003% for the e- and μ-tag samples, respectively.

5.6.3 Forward-backward asymmetry

The $e^+e^- \to \tau^+\tau^-$ events has a slight forward-backward asymmetry (A_{FB}). This could manifest itself into an asymmetry if there is a difference in the selection efficiencies between the forward and backward regions of the detector. However, this effect is modelled in the Monte Carlo simulation and is also present in the control sample. Any asymmetry induced by A_{FB} will have already been taken into account by the control sample.

5.7 Unfolded Asymmetry

In addition to $\tau^- \to \pi^- K^0_S\,(\geq 0\pi^0)\,\nu_\tau$ decays, the sample also contains a $\tau^- \to K^- K^0_S\,(\geq 0\pi^0)\,\nu_\tau$ component as well as a $\tau^- \to \pi^- K^0 \overline{K}^0 \nu_\tau$ component. The $\tau^- \to K^- K^0_S\,(\geq 0\pi^0)\,\nu_\tau$ component is due to the K^- failing the charged kaon selector and being misidentified as the π^- meson. The $\tau^- \to \pi^- K^0 \overline{K}^0 \nu_\tau$ component arises when one of the neutral kaons decays by $K^0_S \to \pi^0\pi^0$, and is then reconstructed as a $\tau^- \to \pi^- K^0_S\, 2\pi^0 \nu_\tau$ candidate.

The two decays have an impact of the overall asymmetry measurement since the SM asymmetry from $\tau^- \to K^- K^0_S\,(\geq 0\pi^0)\,\nu_\tau$ is equal and opposite to the $\tau^- \to \pi^- K^0_S\,\nu_\tau$ asymmetry. This is because the K^0_S in the $\tau^- \to \pi^- K^0_S\,(\geq 0\pi^0)\,\nu_\tau$ mode is produced by a $\overline{K}^0$, whereas the K^0_S in the $\tau^- \to K^- K^0_S\,(\geq 0\pi^0)\,\nu_\tau$ mode is produced by a K^0. The asymmetry from $\tau^- \to \pi^- K^0 \overline{K}^0 \nu_\tau$ is expected to be zero, which in turn dilutes the overall asymmetry. The branching fractions as published by the Particle Data Group (PDG) [1] and predicted SM asymmetry of the three signal modes are given in Table 5.4.

Quantitatively, if f_1 is the fraction of the $\tau^- \to \pi^- K^0_S\,(\geq 0\pi^0)\,\nu_\tau$ decays in the background-corrected sample, and f_2 and f_3 are the fractions of the $\tau^- \to K^- K^0_S\,(\geq 0\pi^0)\,\nu_\tau$ and

Decay mode	B_{PDG}	A_Q (%)
$\tau^- \to \pi^- K^0_S (\geq 0\pi^0)\, \nu_\tau$	$(11.6 \pm 1.1) \times 10^{-3}$	0.33 ± 0.01
$\tau^- \to K^- K^0_S (\geq 0\pi^0)\, \nu_\tau$	$(3.1 \pm 0.2) \times 10^{-3}$	-0.33 ± 0.01
$\tau^- \to \pi^- K^0 \overline{K}^0 \nu_\tau$	$(1.7 \pm 0.4) \times 10^{-3}$	0

Table 5.4: Decay modes and their respective branching ratios [1] and SM asymmetries

$\tau^- \to \pi^- K^0 \overline{K}^0 \nu_\tau$ decays, respectively, then the asymmetry of the overall sample A_{all} is expected to be related to the asymmetry due to the $\tau^- \to \pi^- K^0_S (\geq 0\pi^0)\, \nu_\tau$ mode A_{SM} by the following:

$$A_{all} = \frac{f_1 - f_2}{f_1 + f_2 + f_3} A_{SM} \tag{5.5}$$

The f_i will depend on the efficiency of the selection criteria for each mode. The values of f_1, f_2 and f_3 are (78.4 $\pm$ 4.0)%, (4.2 $\pm$ 0.3)% and (15.6 $\pm$ 3.7)% respectively for e-tag[2], and (77.4 $\pm$ 4.0)%, (4.0 $\pm$ 0.3)% and (15.7 $\pm$ 3.7)% respectively for μ-tag based on the numbers in Tables 4.2 and 4.3. The errors quoted here also include the uncertainties due to the branching fractions as given in the PDG [1]. The result obtained in this study can then be compared with the prediction of Bigi and Sanda by dividing the measured asymmetry of $(-0.34 \pm 0.18 \pm 0.08)\%$ by $(f_1 - f_2)/(f_1 + f_2 + f_3) = 0.75 \pm 0.04$ (the correction is identical for the e-tag and μ-tag samples). The uncertainty on the correction includes the statistical uncertainty and uncertainties in the branching fractions.

5.8 Final result

The average asymmetry due to the $\tau^- \to \pi^- K^0_S (\geq 0\pi^0)\, \nu_\tau$ mode is measured to be $A_Q = (-0.45 \pm 0.24 \pm 0.11)\%$, where the first error is statistical and the second systematic. The result is 3σ from the SM prediction of (0.33$\pm$0.01)% [12].

[2]The values of f_i depend on the charged kaon particle identification inefficiency. However, the uncertainties in the particle identification efficiency are of the order of a few percent – negligible compared to the uncertainties in the branching fractions.

Chapter 6

Conclusions

The analysis of the decay mode $\tau^- \to \pi^- K^0_S\,(\geq 0\pi^0)\,\nu_\tau$ reveals a decay rate asymmetry of:

$$A_Q = (-0.45 \pm 0.24 \pm 0.11)\,\%$$

where the first error is statistical and the second systematic. The systematic uncertainties are due to detector effects, background subtraction, and the uncertainties in the kaon nuclear interaction cross sections. The measured asymmetry is consistent with the Standard Model prediction of (0.33±0.01)% within three standard deviations.

This is the first measurement of the decay rate asymmetry using $\tau^- \to \pi^- K^0_S\,(\geq 0\pi^0)\,\nu_\tau$ decays[1]. Studies of *CP* violation using τ decays have been carried out by Belle [41] and by CLEO [42], both studying the angular distribution of $\tau^- \to \pi^- K^0_S\ \nu_\tau$ decays. None of the three studies (including the one presented in this dissertation) has yielded any evidence for *CP* violation induced by new physics. In a related study on the decay $D^\pm \to K^0_S\pi^\pm$ by *BABAR* [43], the *CP* asymmetry is found to be consistent with the Standard Model prediction.

A measurement that confirms the Standard Model prediction would be an important result. A new high-luminosity B factory (SuperB) is being constructed in Italy with collisions expected in five to ten years. It is expected that the data sample would be over 100 times the size of the dataset used in this work [44]. This would reduce the statistical uncertainty by one order of magnitude, making it possible to confirm the Standard Model prediction, or to find evidence of new physics.

[1] A draft of a journal paper of this work is under final review by the *BABAR* Collaboration and will be submitted to Physical Review D (Rapid Communication).

Appendix A

Mixing of K^0 and $\overline{K}^0$ states

In Chapter 2 the coefficients for the admixtures of $|K^0\rangle$ and $|\overline{K}^0\rangle$ in *CP* eigenstates $|K_1\rangle$ and $|K_2\rangle$ were presented. However, since *CP* symmetry is violated in the kaon sector, different admixtures of $|K^0\rangle$ and $|\overline{K}^0\rangle$ make up the mass eigenstates $|K_S^0\rangle$ and $|K_L^0\rangle$. The derivation for the new admixtures is described in [4] and is presented below.

Consider the basis $\{|K^0\rangle, |\overline{K}^0\rangle\}$. They span a two-dimensional vector space. One can represent $|K^0\rangle$ with the vector $\begin{pmatrix} 1 \\ 0 \end{pmatrix}$ and $|\overline{K}^0\rangle$ with $\begin{pmatrix} 0 \\ 1 \end{pmatrix}$. An arbitrary linear combination of $|K^0\rangle$ and $|\overline{K}^0\rangle$ can then be represented in the following manner:

$$\alpha|K^0\rangle + \beta|\overline{K}^0\rangle = \begin{pmatrix} \alpha \\ \beta \end{pmatrix} \tag{A.1}$$

The time-dependent Schrödinger Equation can be expressed as:

$$i\hbar\frac{d}{dt}\begin{pmatrix} \alpha \\ \beta \end{pmatrix} = \hat{X}\begin{pmatrix} \alpha \\ \beta \end{pmatrix} \tag{A.2}$$

where $\hat{X} = \mathbf{M} - i\mathbf{\Gamma}/2$, $\mathbf{M}$ and $\mathbf{\Gamma}$ are Hermitian matrices known as the mass and decay matrices, respectively. Note that $\hat{X}$ is not Hermitian in general. The matrix representation of $\hat{X}$ in the basis of $|K^0\rangle$ and $|\overline{K}^0\rangle$, $\hat{X}_{ij}$, is:

$$\hat{X}_{ij} = \begin{bmatrix} \langle K^0|\hat{X}|K^0\rangle & \langle K^0|\hat{X}|\overline{K}^0\rangle \\ \langle \overline{K}^0|\hat{X}|K^0\rangle & \langle \overline{K}^0|\hat{X}|\overline{K}^0\rangle \end{bmatrix} \tag{A.3}$$

With the assumption of CPT invariance, the masses and decay times for K^0 and $\overline{K}^0$ are identical; therefore, $\langle K^0|\hat{X}|K^0\rangle = \langle \overline{K}^0|\hat{X}|\overline{K}^0\rangle$. The matrix $\hat{X}_{ij}$ is then of the following form:

$$\hat{X}_{ij} \sim \begin{bmatrix} x & a \\ b & x \end{bmatrix} \tag{A.4}$$

To find the eigenstates, which will be known as $|K_S^0\rangle$ and $|K_L^0\rangle$, one needs to find the eigenstates. The eigenvalues can be obtained by diagonalizing the matrix, i.e. to solve for λ in the characteristic equation:

$$\begin{aligned} det\left(\hat{X}_{ij} - \lambda\mathbf{I}\right) &= 0 \qquad (A.5) \\ \Rightarrow (x-\lambda)^2 - ab &= 0 \\ \Rightarrow \lambda^2 - 2x\lambda + \left(x^2 - ab\right) &= 0 \\ \Rightarrow \lambda &= \frac{2x \pm \sqrt{4x^2 - 4\left(x^2 - ab\right)}}{2} \\ &= x \pm \sqrt{ab} \qquad (A.6) \end{aligned}$$

For the eigenvalue $\lambda_+ \equiv x + \sqrt{ab}$, the corresponding eigenstate (eigenvector) is the nullspace of $X_{ij} - \lambda_+\mathbf{I}$:

$$\begin{aligned} \begin{bmatrix} x-\lambda_+ & a \\ b & x-\lambda_+ \end{bmatrix} &= \begin{bmatrix} -\sqrt{ab} & a \\ b & -\sqrt{ab} \end{bmatrix} \\ &\rightarrow \begin{bmatrix} -\sqrt{ab} & a \\ 0 & 0 \end{bmatrix} \end{aligned} \tag{A.7}$$

where "$\rightarrow$" represents row reduction. The nullspace of $\hat{X}_{ij} - \lambda_- \mathbf{I}$ is hence spanned by $\begin{pmatrix} \sqrt{a} \\ \sqrt{b} \end{pmatrix}$.

Similarly, for the eigenvalue $\lambda_- \equiv x - \sqrt{ab}$:

$$\begin{aligned} \begin{bmatrix} x - \lambda_- & a \\ b & x - \lambda_- \end{bmatrix} &= \begin{bmatrix} \sqrt{ab} & a \\ b & \sqrt{ab} \end{bmatrix} \\ &\rightarrow \begin{bmatrix} \sqrt{ab} & a \\ 0 & 0 \end{bmatrix} \end{aligned} \tag{A.8}$$

The nullspace is hence spanned by $\begin{pmatrix} \sqrt{a} \\ -\sqrt{b} \end{pmatrix}$. Therefore, the two eigenstates are:

$$\begin{aligned} |K_S^0\rangle &\propto \sqrt{a}|K^0\rangle + \sqrt{b}|\overline{K}^0\rangle \\ |K_L^0\rangle &\propto \sqrt{a}|K^0\rangle - \sqrt{b}|\overline{K}^0\rangle \end{aligned} \tag{A.9}$$

where the proportionality constant is chosen such that the eigenstates are normalized. The proportionality constant for both eigenstates is thus $\frac{1}{a+b}$. Define $p \equiv \frac{\sqrt{a}}{a+b}$ and $q \equiv \frac{\sqrt{b}}{a+b}$, and one recovers the form in Chapter 2:

$$\begin{aligned} |K_S^0\rangle &= p|K^0\rangle + q|\overline{K}^0\rangle \\ |K_L^0\rangle &= p|K^0\rangle - q|\overline{K}^0\rangle \end{aligned}$$

Appendix B

BABAR Terminology

The *BABAR* terminology mentioned in this work is defined in this appendix. The criteria in defining the following terms are not exclusive to this work; rather, they are used in all *BABAR* analyses.

Basic components

- Tracks: Tracks are reconstructed in the SVT/DCH detectors, as outlined in Section 3.2. The tracks are put into different lists with varying levels of selection criteria.

  The GoodTrackVeryLoose list is used in this work. A track in the GoodTrackVeryLoose list must satisfy the following criteria:

  - Polar angle θ between 0.410 and 2.54 radians, which corresponds to -0.824< $cos(\theta)$ <0.917 in the laboratory frame;
  - Momentum p is less than 10 GeV/c in the laboratory frame;
  - Maximum distance of closest approach from the interaction point (DOCA) in the transverse plane d_0 is 1.5 cm; and
  - The z-coordinate of DOCA z_0 must be between -10 cm and 10 cm.

- Neutral clusters: Energy deposits in the calorimeter that are not associated with any reconstructed tracks are assumed to originate from photons in the decay. In this work, the neutral clusters are used to reconstruct π^0 in the decay $\pi^0 \to \gamma\gamma$.

The list used in this work is CalorNeutral, which consists of energy deposits not associated with any tracks. In addition, a cluster in the CalorNeutral list must satisfy the following criteria:

- Energy associated with the cluster must be greater than 30 MeV;
- The lateral moment must be between 0 and 0.6[1]; and
- The number of crystals hit in the calorimeter must be greater than 3.

List definitions

- Conversion list: Photons can convert to produce two oppositely charged tracks when they interact with material in the detector. The conversion list used in this work is gammaConversionDefault. This list requires that a pair of oppositely charged tracks satisfy the following criteria:
  - The invariant mass of the two tracks is less than $30\,\mathrm{MeV}/c^2$, assuming the tracks are electrons;
  - The distance between the decay vertex and the e^+e^- interaction point in the xy-plane must be between 0 cm and 27 cm; and
  - The quality of the vertex reconstruction must be good, as measured by χ^2.
- Muon selector (muNNTight): The muon selector used in the analysis, muNNTight, is a selector based on a neural net determined by the following variables:
  - Energy in the EMC;
  - Number of IFR hit layers in a cluster;
  - Number of interaction lengths traversed by the particle;
  - Difference between the expected and measured number of interaction lengths traversed;

[1]The lateral moment of the shower in the calorimeter (LAT) is defined as:

$$LAT = \frac{\sum_{i=3}^{N} E_i r_i^2}{\sum_{i=1}^{N} E_i r^2} \tag{B.1}$$

where E_i is the energy deposited in a crystal in the cluster; r_i is the distance of the crystal to the cluster centre; and r is the length scale of a crystal, 5 cm [45]. E_i are listed in decreasing order.

  - $\chi^2/D.O.F.$ of a polynomial fit of the cluster compared with the IFR hit strips;
  - $\chi^2/D.O.F.$ of the track extrapolation compared with the IFR hit strips;
  - A variable T_c related to track continuity, determined from the ratio of the total number of IFR hit layers in cluster to the total number of IFR layers spanned by the cluster. T_c should peak at 1 for continuous tracks; and
  - Average and standard deviation of the distribution of the multiplicity of hit strips per layer in a cluster.

- KM particle selector lists: The electron, pion and kaon lists – eKMTight, piKMTight and kKMTight respectively – are derived according to outcomes from an Error-Correcting Output Code (ECOC) [46]. The algorithm compares the particle with a training sample and determines whether it is an electron, a charged pion, a charged kaon or a proton. The algorithm uses variables such as kinematic properties of the track, energy loss and recorded hits in the SVT and DCH, patterns in the DIRC, and energy deposits in the EMC. The efficiencies for the KM particle selector lists are 95% for electrons and charged pions above $1\,\mathrm{GeV}/c$, and above 80% for charged kaons less than $3\,\mathrm{GeV}/c$ [47].

- K_S^0 selector (KsTight): The K_S^0 selector list used in this work is KsTight. The criteria are as follows:

  - The K_S^0 decays into two oppositely charged tracks;
  - The mass of the K_S^0 candidate is between $0.47267\,\mathrm{GeV}/c^2$ and $0.52267\,\mathrm{GeV}/c^2$;
  - After vertex reconstruction, the mass is required to be between $0.45\,\mathrm{GeV}/c^2$ and $0.55\,\mathrm{GeV}/c^2$;
  - The χ^2 probability given in the track fit algorithm is greater than 0.001; and
  - The distance between the e^+e^- interaction vertex to the K_S^0 decay vertex is more than three times its uncertainty.

Appendix C

Control sample studies

The control sample uses the Tau1N skim, which consists of $\tau^- \to \pi^-\pi^-\pi^+(\geq 0\pi^0)\nu_\tau$ decays (and the charge conjugate decays) tagged with a $\tau^+ \to \ell^+\nu_\ell\overline{\nu}_\tau$ decay in the opposite hemisphere. The K^0_S contamination is suppressed due to requirement in the Tau1N skim that the three tracks originate at the collision vertex (see Figs. C.1–C.7).

In the Standard Model, there is no *CP* violation in the $\tau^- \to \pi^-\ \pi^-\ \pi^+\ \nu_\tau$ decay mode and searches have found no evidence for *CP* violation. *CP* violation only arises through the K^0_S through which the τ decays. The control sample should have no asymmetry under the Standard Model. In other models (such as SUSY), the control sample is not expected to show a charge asymmetry at the present level of sensitivity ([38], [39]).

The control sample uses the same preselection criteria as the nominal selection. Fig. C.1 displays thrust (top) and momentum of tag particle in the centre-of-mass frame (bottom) in the e-tag control sample after the preselection criteria are applied. The same plots for the μ-tag control sample are shown in Fig. C.2. In addition, it is required that the invariant mass of the three particle system be less than 1.8 GeV/c^2 (see Figs. C.4 and C.5).

Additional cuts are imposed on the e-tag control sample to ensure that radiative Bhabha events are vetoed:

- The selection criterion on the thrust is changed from 0.995 to 0.99;
- The z-component of the thrust vector must be less than 0.9 (Fig. C.3); and
- The sum of the momenta of the two lower-momentum signal tracks must be greater than 1 GeV/c (Fig. C.3).

The charge asymmetries observed in both the control data and control MC samples are summarised in Table C.1. We show the results for both the e-tag and μ-tag samples. The composition of the control Monte Carlo sample is shown in Table C.2 for e-tag and Table C.3 for μ-tag.

The e-tag sample is more challenging due to the impact of radiative Bhabha events generating photons, which then convert into an e^+e^- system in the detector. Radiative Bhabha events are not included in the Monte Carlo simulation. Even with the photon conversion rejection requirements, we observe significant discrepancies between the data and MC for the $\tau^- \to \pi^- \pi^- \pi^+ \nu_\tau$ sample whereas the samples with one or more π^0 mesons are in better agreement. Radiative Bhabhas are not present in the μ-tag sample, so we compare the e-tag and the μ-tag samples to see the extent and the impact of Bhabha contamination (See Figs. C.6 and C.7 for the mass plots for 3π decay in the μ-tag sample). The discrepancy in the tail of the $(\pi^- \pi^- \pi^+)$ mass spectrum is most likely caused by radiative Bhabhas, as similar discrepancy is not observed in the μ-tag sample.

The charge asymmetries for data and MC differ by 0.12% in the e-tag sample. We include this as a systematic error (see Section 5.4). The charge asymmetries for data and MC in the μ-tag sample, on the other hand, are consistent within the quoted uncertainties. The sum of the data and MC statistical errors in the μ-tag control sample is 0.08% and is included as a systematic error.

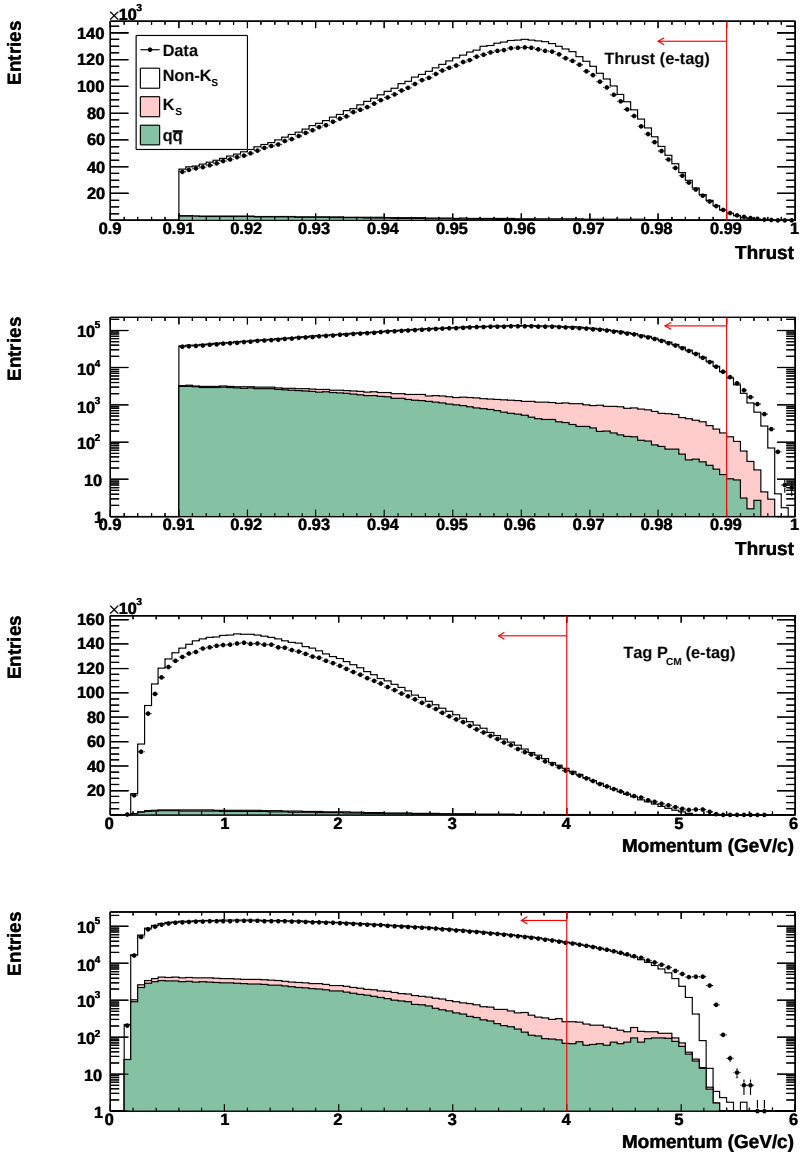

Figure C.1: Thrust (top) and momentum of the tag track in the centre-of-mass frame (bottom) for the e-tag control sample. All selection criteria except for the variable depicted in the distribution have been applied. The selection criterion on the thrust has been tightened from 0.995 to 0.99 to veto Bhabha contamination. The red lines indicate the selection criteria.

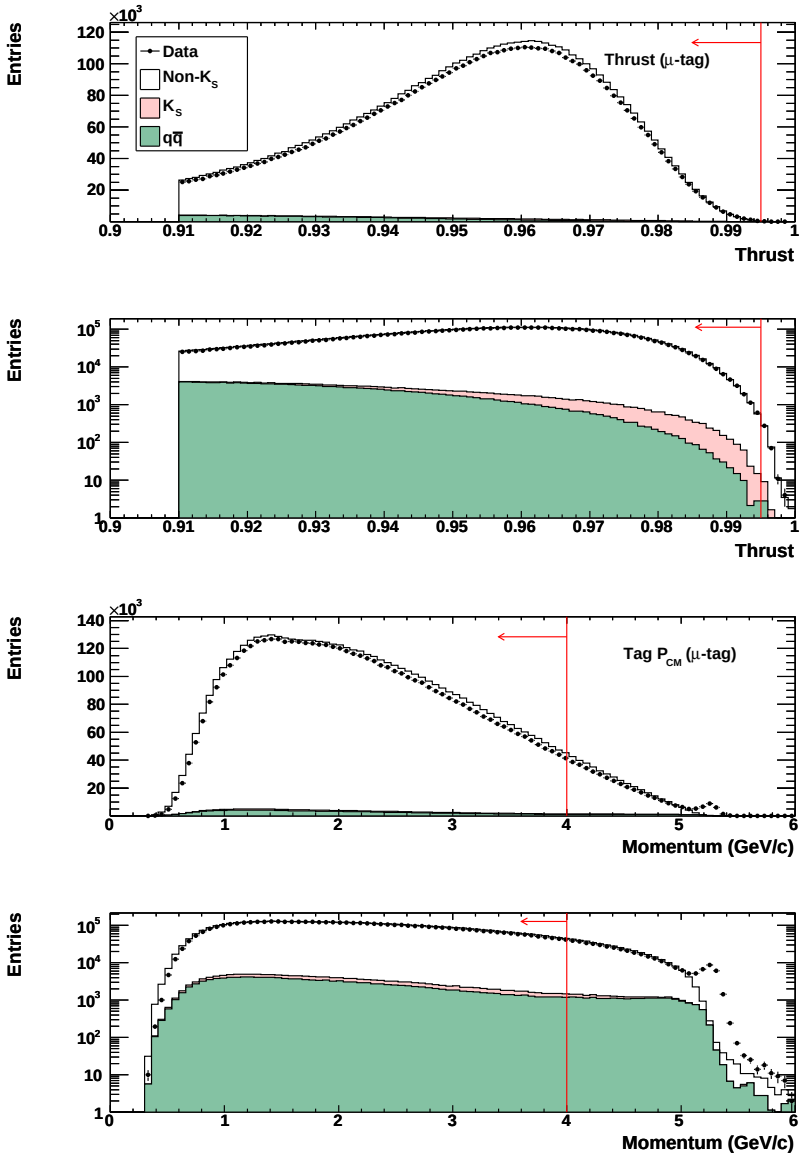

Figure C.2: Thrust (top) and momentum of the tag track in the centre-of-mass frame (bottom) for the μ-tag control sample. All selection criteria except for the variable depicted in the distribution have been applied. The red lines indicate the selection criteria.

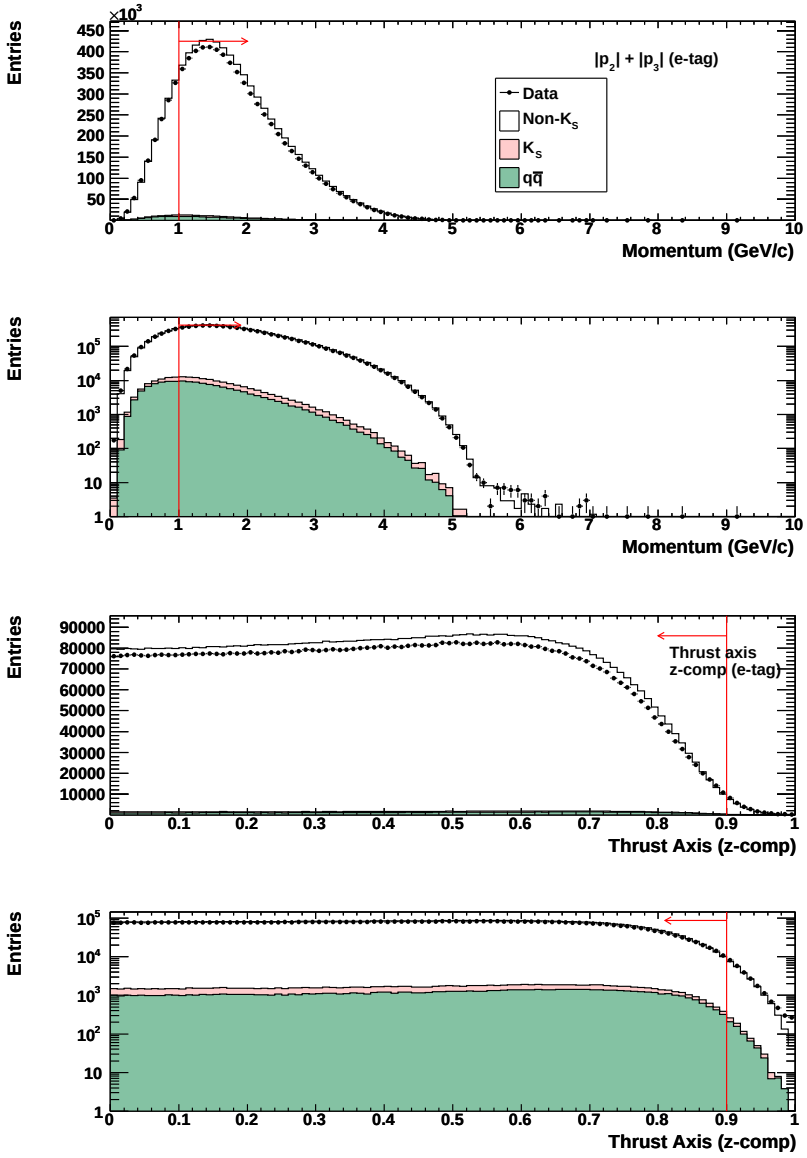

Figure C.3: The sum of momenta of the two lower-momentum tracks (top) and the z-component of the thrust vector (bottom) for the e-tag control sample. These selection criteria are imposed to veto Bhabha contamination in the e-tag control sample. The red lines indicate the selection criteria.

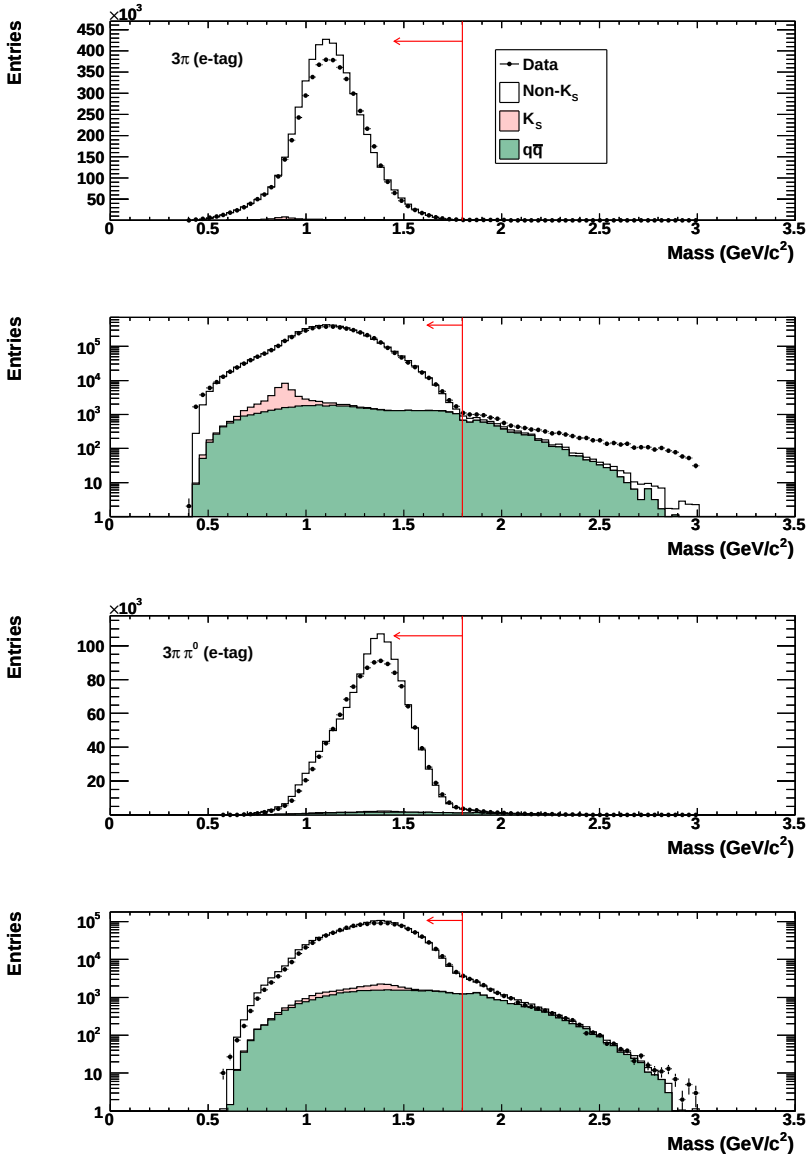

Figure C.4: Invariant mass of 3π (top) and $3\pi\pi^0$ (bottom) in the signal hemisphere in the e-tag control sample. The discrepancy between Monte Carlo simulation and data in the 3π invariant mass plot is due to Bhabha contamination. The red lines indicate the selection criteria.

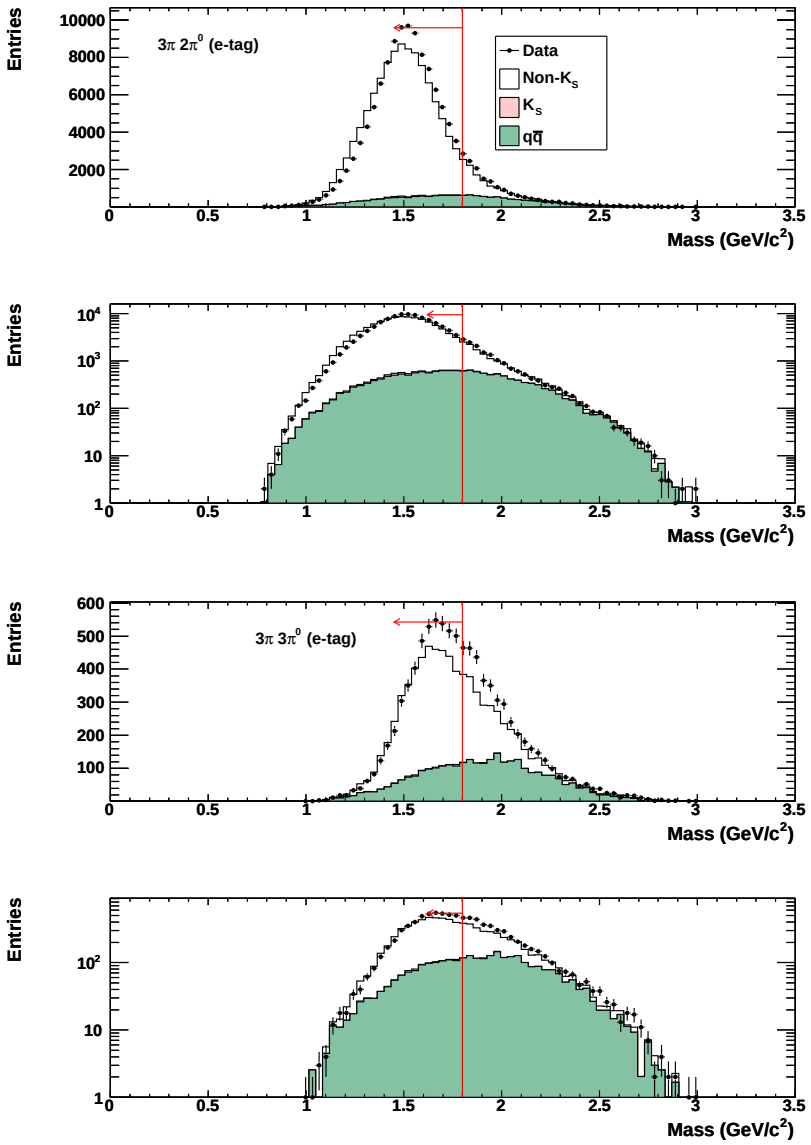

Figure C.5: Invariant mass of $3\pi 2\pi^0$ (top) and $3\pi 3\pi^0$ (bottom) in the signal hemisphere in the e-tag control sample. The red lines indicate the selection criteria.

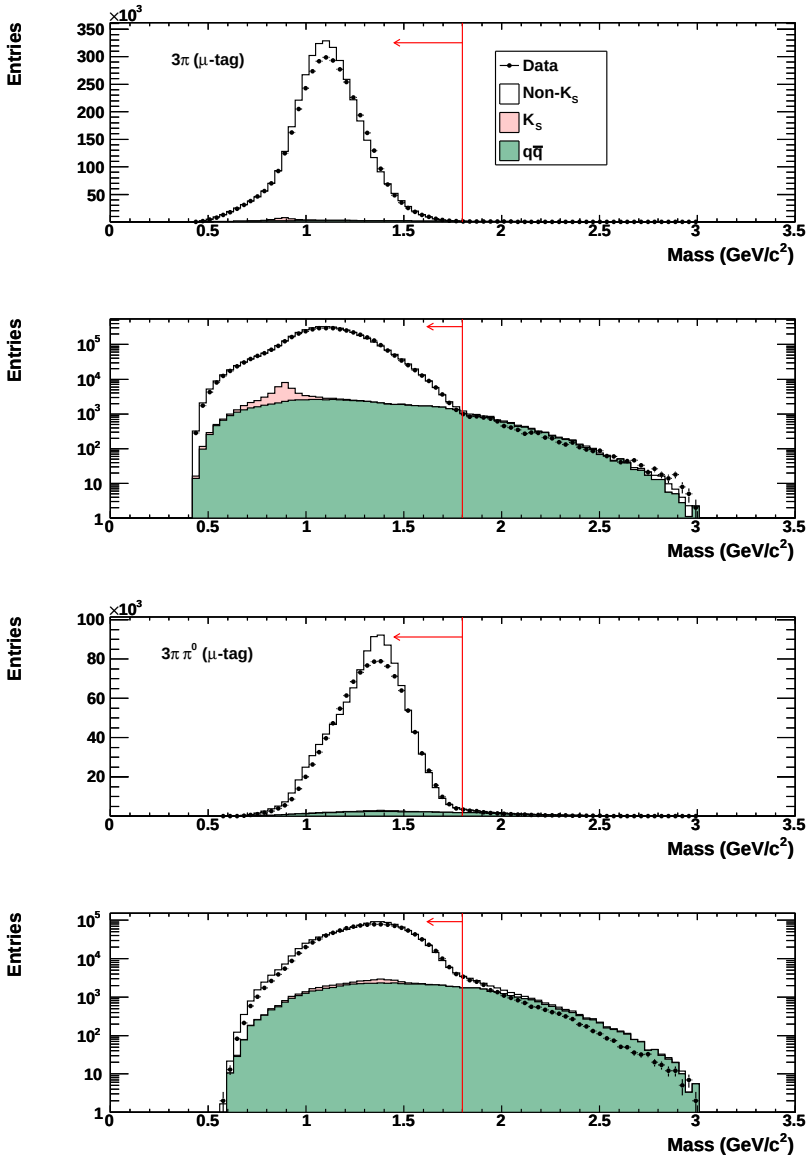

Figure C.6: Invariant mass of 3π (top) and $3\pi\pi^0$ (bottom) in the signal hemisphere in the μ-tag control sample. The red lines indicate the selection criteria.

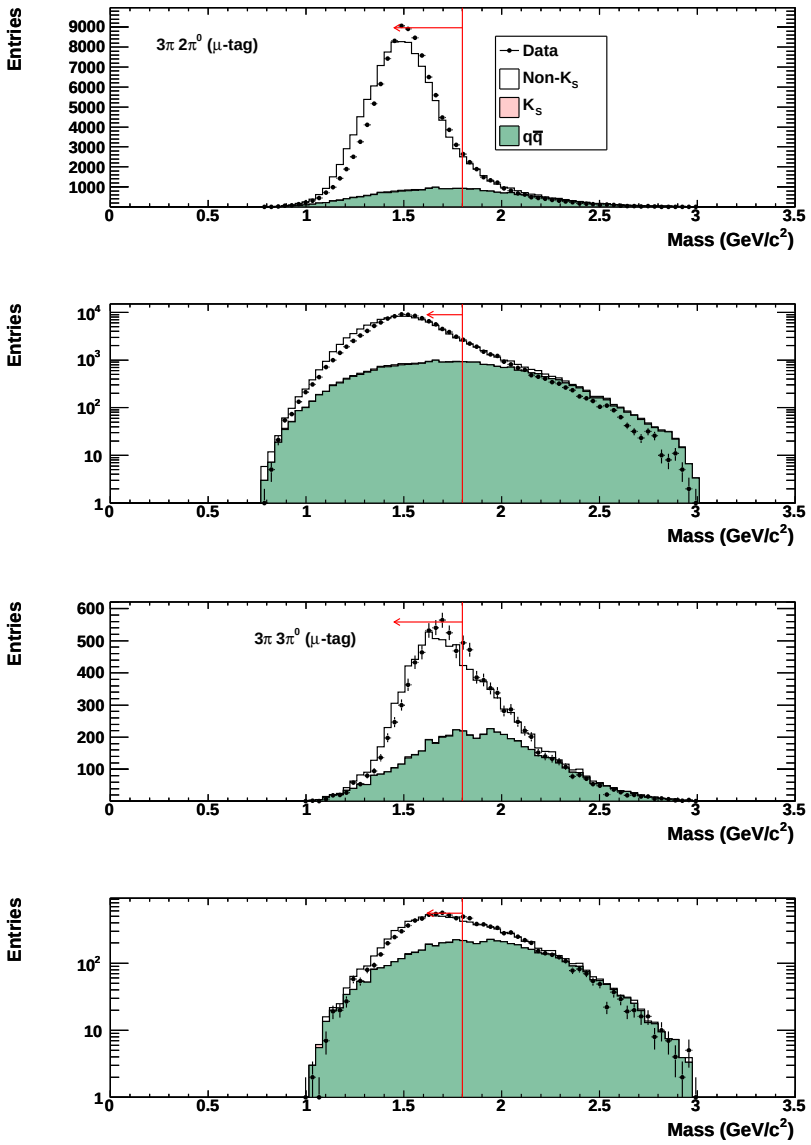

Figure C.7: Invariant mass of $3\pi 2\pi^0$ (top) and $3\pi 3\pi^0$ (bottom) in the signal hemisphere in the μ-tag control sample. The red lines indicate the selection criteria.

Sample	Positive Tag	Negative Tag	A_Q
Data (e-tag)	3207678 ± 1791	3203527 ± 1790	$(-0.065 \pm 0.039)\%$
MC (e-tag)	3368353 ± 1396	3372450 ± 1397	$(0.061 \pm 0.029)\%$
Data (μ-tag)	2608240 ± 1615	2614261 ± 1617	$(0.115 \pm 0.044)\%$
MC (μ-tag)	2720567 ± 1255	2726283 ± 1256	$(0.105 \pm 0.033)\%$

Table C.1: Asymmetries measured in the control samples for data and Monte Carlo simulation.

Type	Events	% of MC
Data	6411205 ± 2532	
MC	6740802 ± 1975	100
τ non-K_S decays	6599205 ± 1968	97.90 ± 0.04
Background	141597 ± 273	2.101 ± 0.004
$\pi^- K_S$ background	31722 ± 136	0.471 ± 0.002
$K^- K_S$ background	7771 ± 67	0.1153 ± 0.0010
uds	15232 ± 92	0.226 ± 0.001
$c\overline{c}$	86872 ± 208	1.289 ± 0.003

Table C.2: Results for e-tag control sample after selection criteria. Errors are statistical only.

Type	Events	% of MC
Data	5222501 ± 2285	
MC	5446850 ± 1775	100
τ non-K_S decays	5262142 ± 1758	96.61 ± 0.05
Background	184708 ± 314	3.391 ± 0.006
$\pi^- K_S$ background	27500 ± 126	0.505 ± 0.002
$K^- K_S$ background	5992 ± 59	0.110 ± 0.001
uds	68971 ± 196	1.266 ± 0.004
$c\overline{c}$	82245 ± 202	1.510 ± 0.004

Table C.3: Results for μ-tag control sample after selection criteria. Errors are statistical only.

Appendix D

μ-tag Results

The distributions for the kinematic variables used in the selection criteria are observed to be similar for e-tag and μ-tag samples. Distributions of the variables for μ-tag are presented here. The e-tag plots are presented in Section 4.3.

D.1 Selection Prior to Likelihood

Figs. D.1 and D.2 show the magnitude of the thrust of the event, the magnitude of the momentum of the tag particle in the centre-of-mass frame, and the invariant mass of $\pi^+\,\pi^-$ pair in $K^0_S \to \pi^+\,\pi^-$ candidates. Figs. D.3 and D.4 show the invariant mass of the hadronic system in the decay $\tau^- \to \pi^- K^0_S\,(\geq 0\pi^0)\,\nu_\tau$ in the signal hemisphere. A K^0_S peak can be observed in the invariant mass spectrum of the $2\pi^0$ mesons in the decay $\tau^- \to \pi^- K^0_S\;2\pi^0\nu_\tau$ (see Fig. D.5), which is also observed in the e-tag sample. A similar peak at $\sim 500\,\mathrm{MeV}/c^2$ can be observed in the invariant mass spectrum of the $3\pi^0$ mesons in the decay $\tau^- \to \pi^- K^0_S\;3\pi^0\nu_\tau$ in the μ-tag (also in Fig. D.5), although the peak is less pronounced than the case found in the e-tag.

D.2 Approximate Likelihood Ratio

The distributions shown in Figs. D.6, D.7 and D.8 are the variables used in the approximate likelihood separating $e^+e^- \to q\overline{q}$ events from $e^+e^- \to \tau^+\tau^-$ events whereas Figs. D.9 and D.10 display the distributions of the variables of the approximate likelihood used to identify

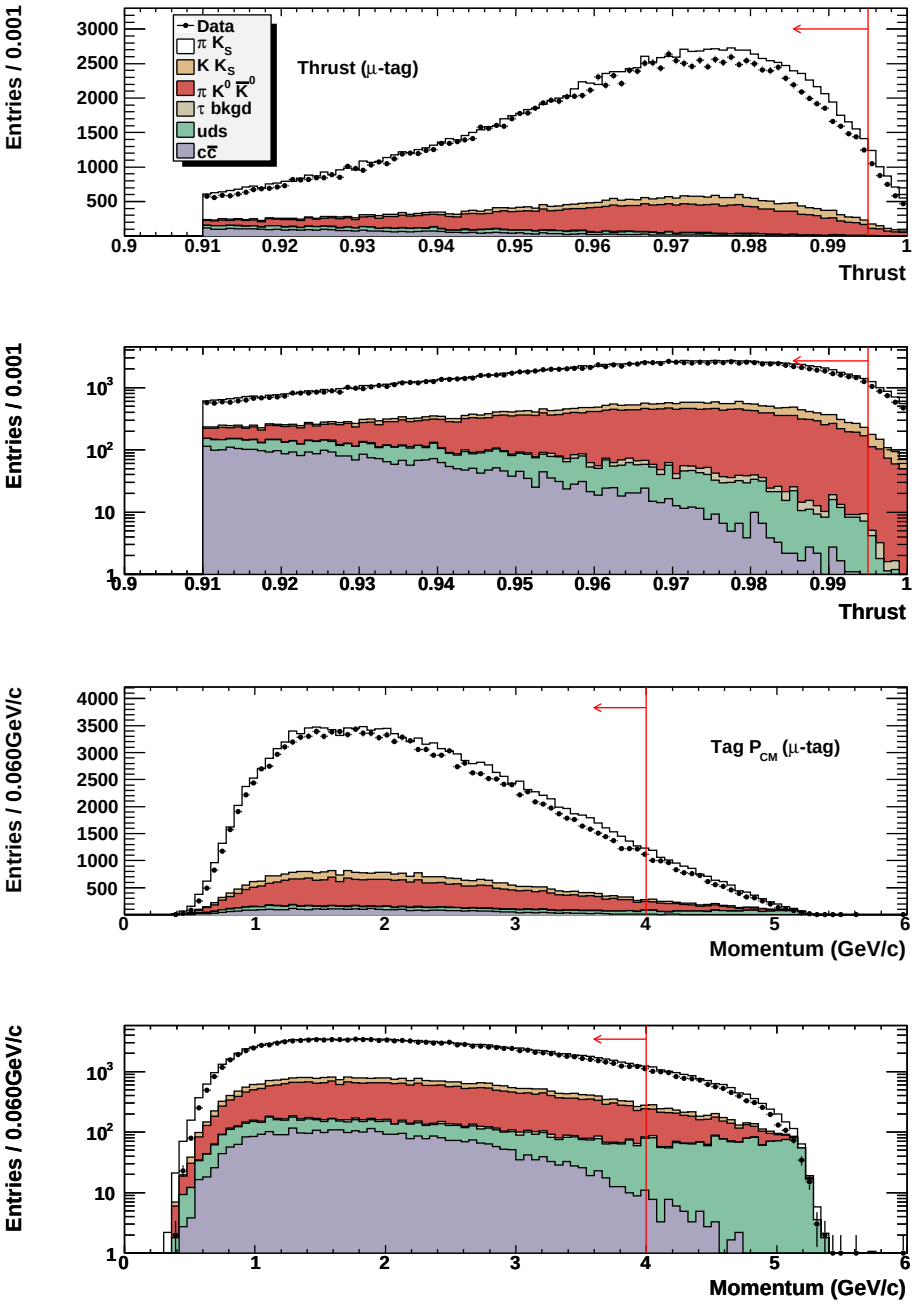

Figure D.1: Thrust (top pair) and momentum of the tag particle in the tag hemisphere in the centre-of-mass frame (bottom pair) in the μ-tag sample. Within both pairs of plots, the linear plot is displayed above and the semi-logarithmic plot is displayed below. Points represent data while the filled histograms represent Monte Carlo simulation, with white, orange and red representing the three signal modes. The red line indicates the value of the selection criterion, with the arrow indicating the region of the distribution kept for the analysis.

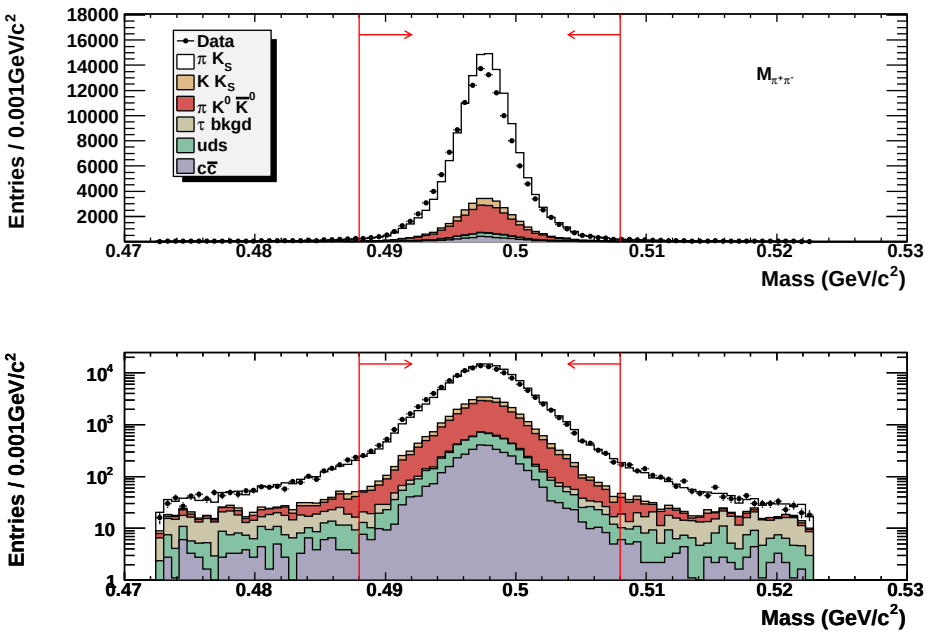

Figure D.2: Invariant mass of $\pi^+\ \pi^-$ in $K^0_S \to \pi^+\ \pi^-$ in the μ-tag sample. As in Fig. D.1, the top plot is linear while the bottom plot is semi-logarithmic. The colour scheme of the histograms is the same as that in Fig. D.1.

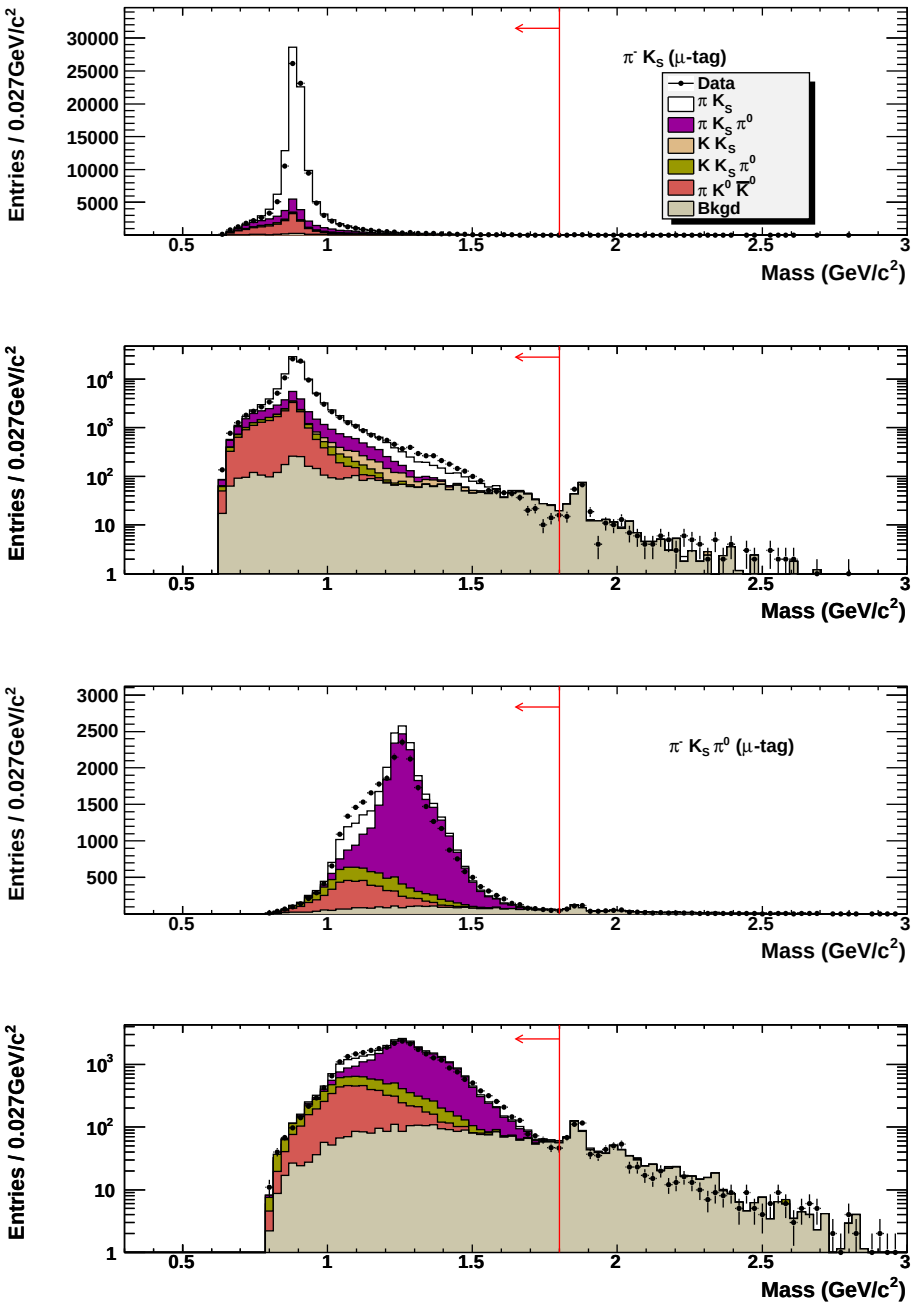

Figure D.3: Invariant mass of the π^- K^0_S (top pair) and π^- K^0_S π^0 (bottom pair) systems for μ-tagged events. Within each pair of plots, the top is the linear plot while the bottom is semi-logarithmic. All selection criteria except for the likelihood ratios and the invariant mass criteria have been applied.

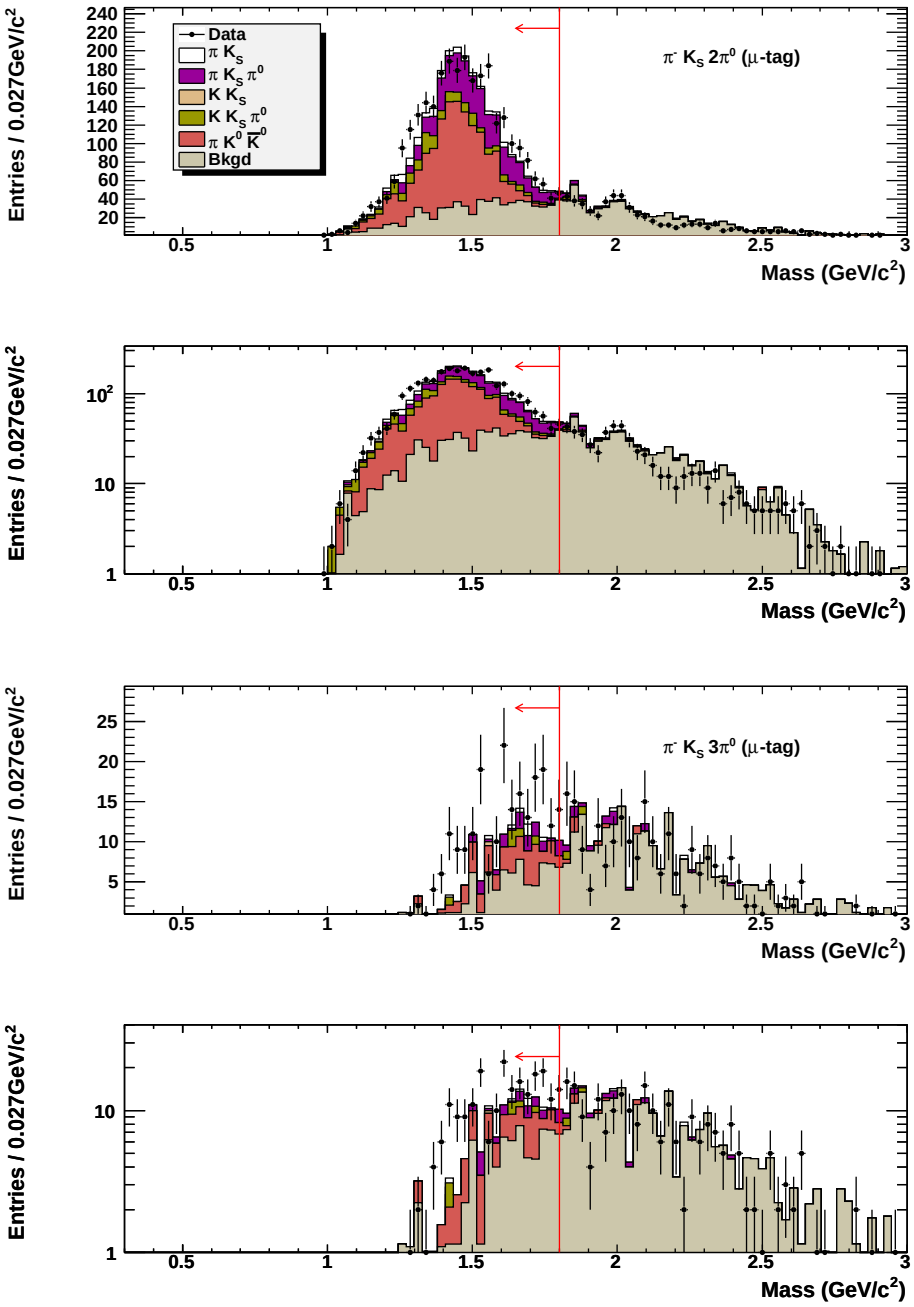

Figure D.4: Invariant mass of the π^- K^0_S $2\pi^0$ (top pair) and π^- K^0_S $3\pi^0$ (bottom pair) systems for μ-tagged events. Within each pair of plots, the top is the linear plot while the bottom is semi-logarithmic. All selection criteria except for the likelihood ratios and the invariant mass criteria have been applied.

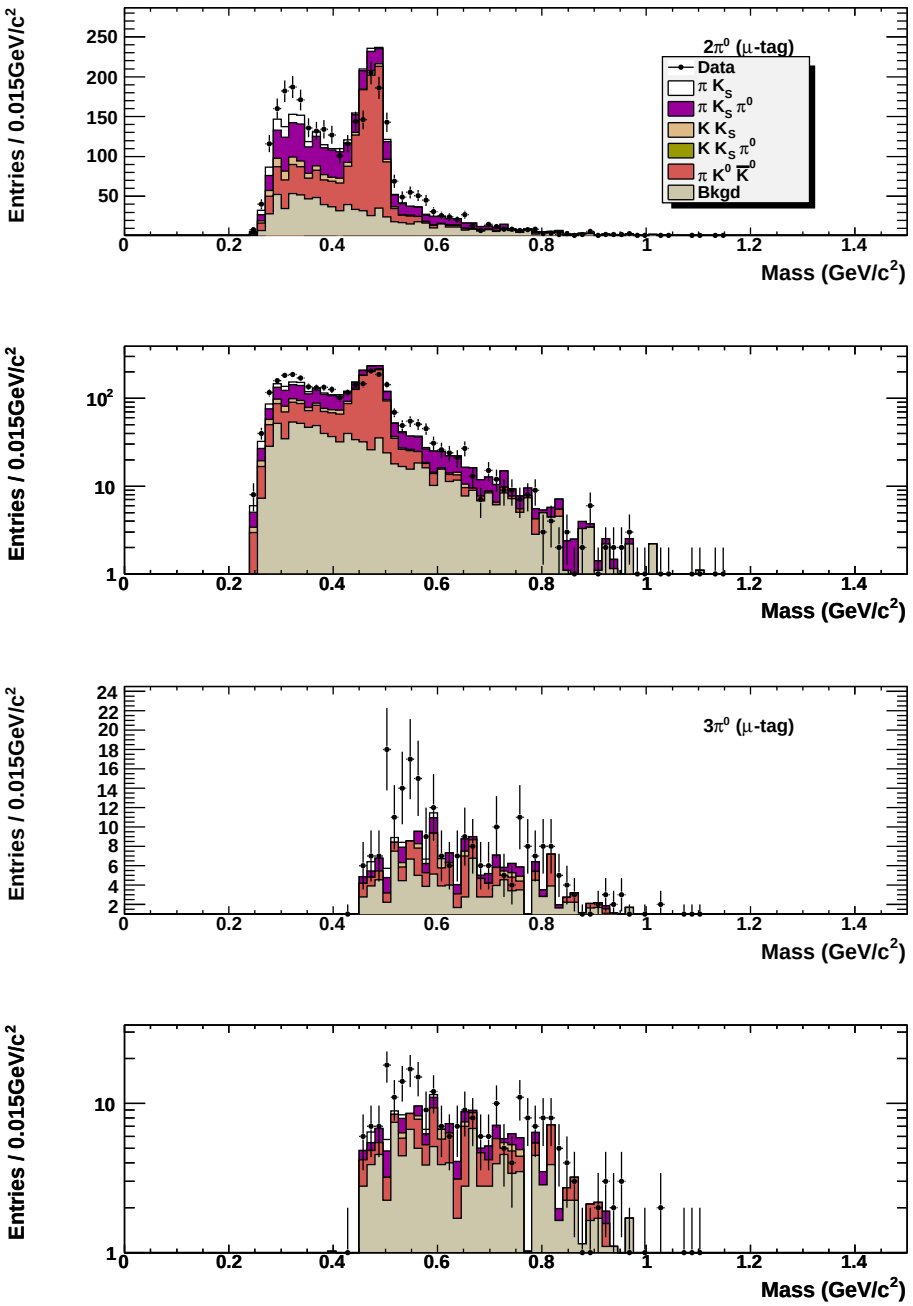

Figure D.5: Invariant mass of the $2\pi^0$ in the decay $\tau^- \to \pi^- K_S^0\ 2\pi^0\nu_\tau$ (top pair) and of the $3\pi^0$ in the decay $\tau^- \to \pi^- K_S^0\ 3\pi^0\nu_\tau$ (bottom pair) for μ-tagged events. All selection criteria except for the likelihood ratios have been applied.

events with a K_S^0 meson.

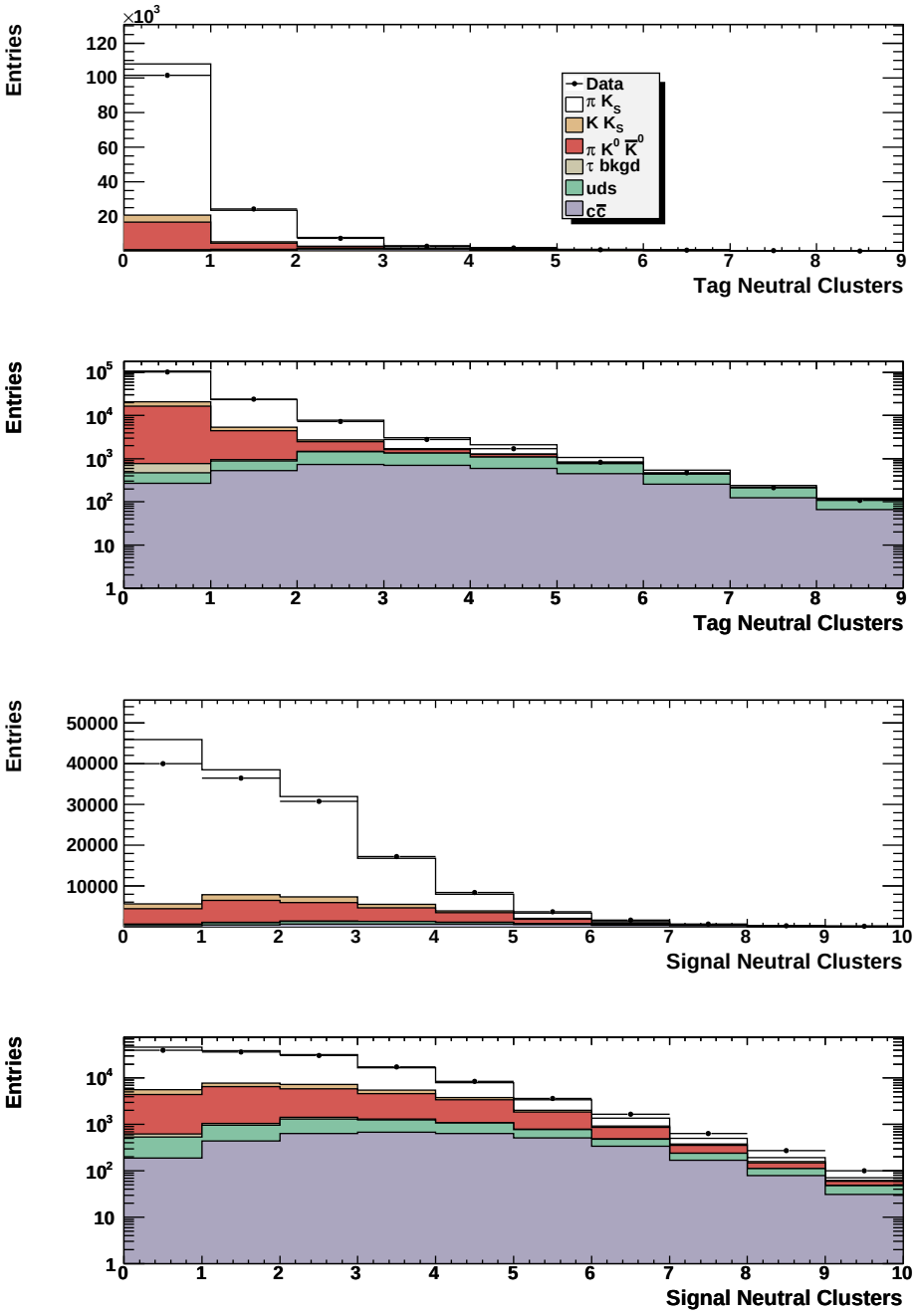

Figure D.6: Numbers of neutral clusters in the tag (top pair) and signal (bottom pair) hemispheres in the μ-tag sample. These two variables are used in the determination of the approximate likelihood separating $e^+e^- \to \tau^+\tau^-$ events from $e^+e^- \to q\overline{q}$ events. All selection criteria except for the likelihood ratios have been applied.

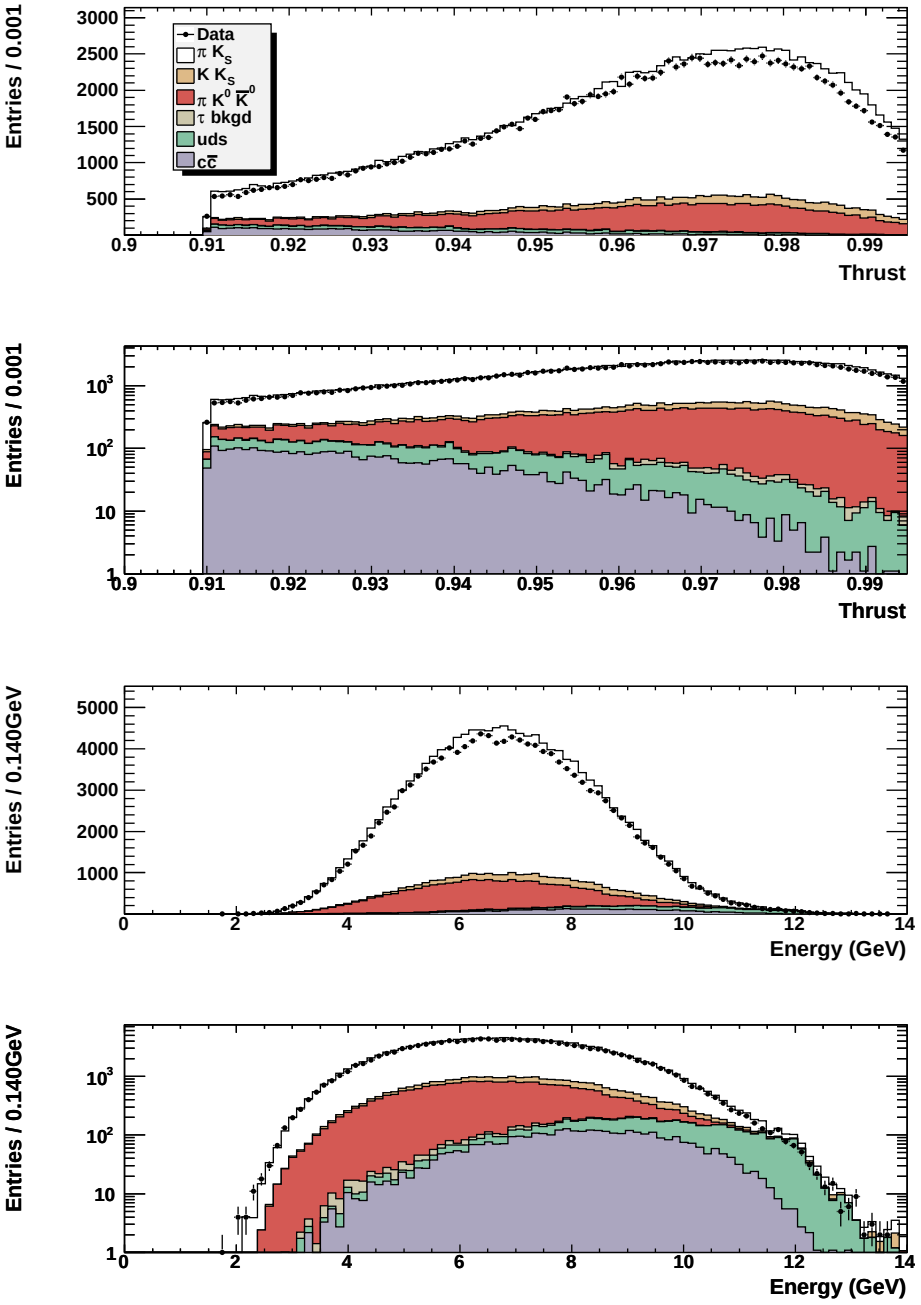

Figure D.7: Event thrust (top pair) and visible energy (bottom pair) in the μ-tag sample. These two variables are used in the determination of the approximate likelihood separating $e^+e^- \to \tau^+\tau^-$ events from $e^+e^- \to q\overline{q}$ events. All selection criteria except for the likelihood ratios have been applied.

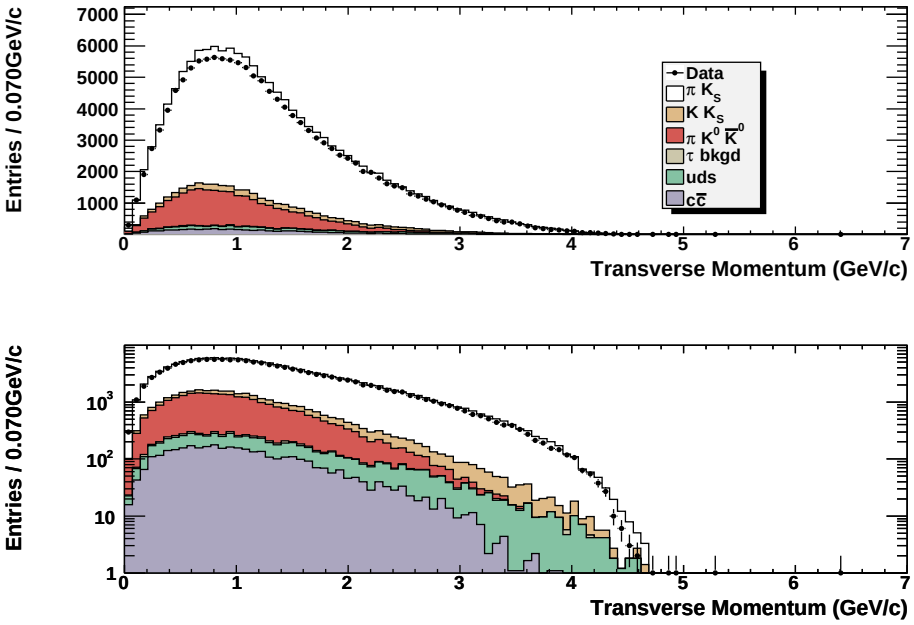

Figure D.8: Transverse component of the total momentum of all tracks and neutral clusters in the μ-tag sample. This variable is used in the determination of the approximate likelihood separating $e^+e^- \to \tau^+\tau^-$ events from $e^+e^- \to q\overline{q}$ events. All selection criteria except for the likelihood ratios have been applied.

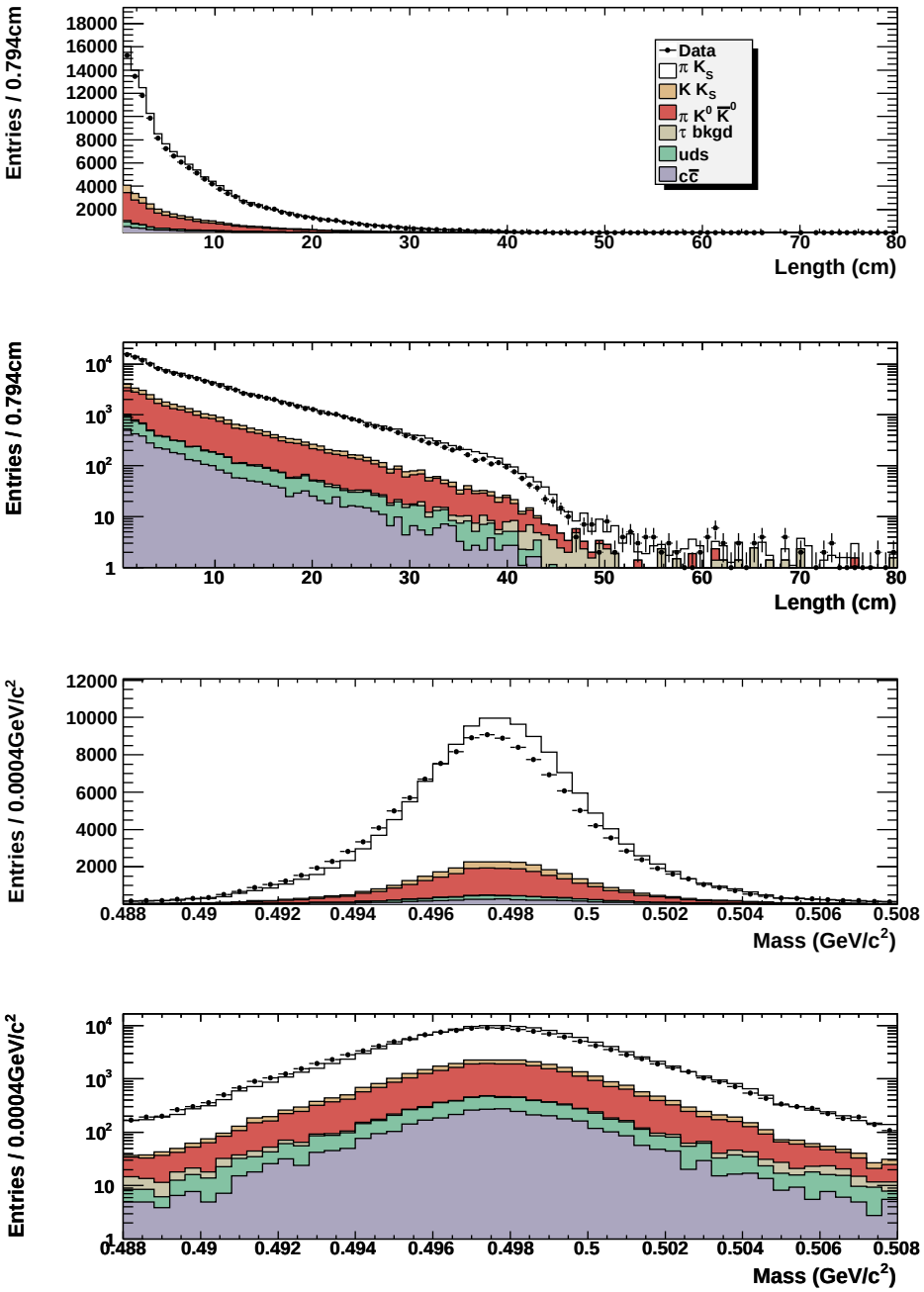

Figure D.9: K^0_S decay length in the xy-plane (top pair) and invariant mass of $\pi^+\pi^-$ in $K^0_S \to \pi^+\,\pi^-$ (bottom pair) in the μ-tag sample. These two variables are used in the determination of the approximate likelihood identifying events with K^0_S in the final state. All selection criteria except for the likelihood ratios have been applied.

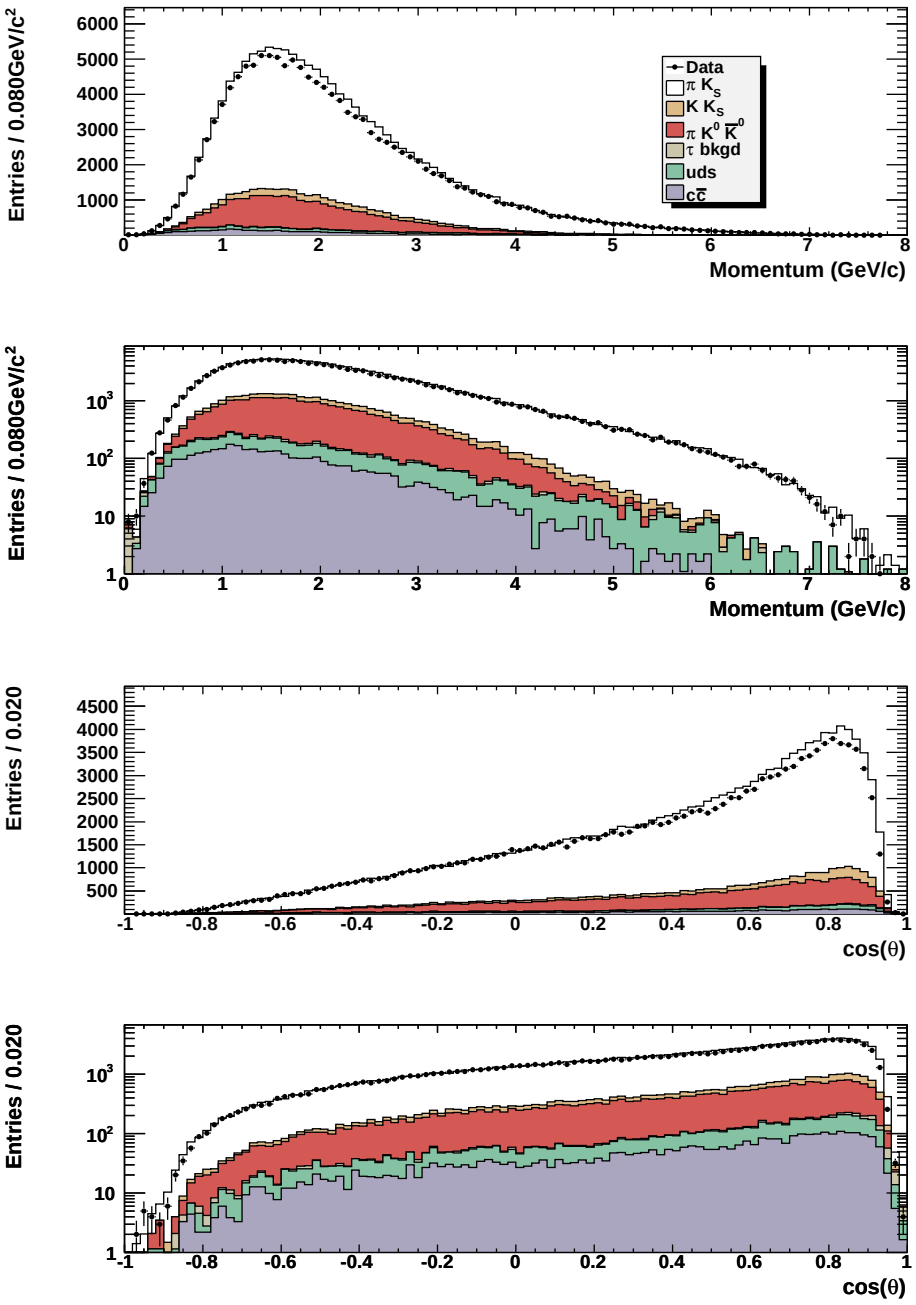

Figure D.10: Momentum of the K_S^0 (top pair) and cosine of the polar angle of the K_S^0 (bottom pair), both in the laboratory frame in the μ-tag sample. These two variables are used in the determination of the approximate likelihood identifying events with K_S^0 in the final state. All selection criteria except for the likelihood ratios have been applied.

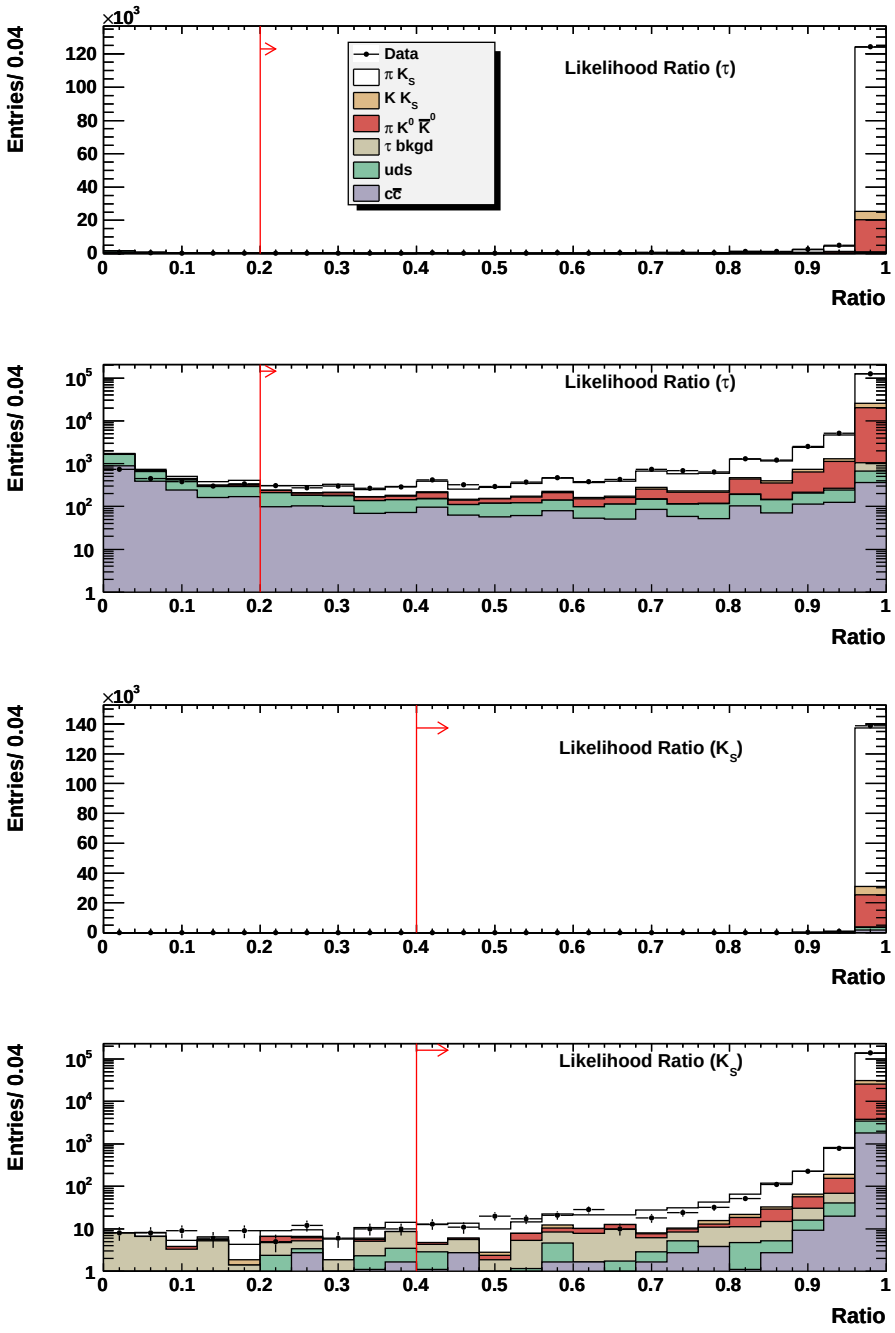

Figure D.11: Likelihood ratios to distinguish τ events from $e^+e^- \to q\overline{q}$ events (top pair) and τ decays with K_S^0 from those without (bottom pair) (μ-tag sample).

Appendix E

Asymmetry correction due to K_S^0 interaction in the detector material

It was noted by Ko et al [37] that neutral kaons have a non-zero probability of interacting with the material in the beam pipe and the silicon vertex detectors. Further, the difference in the K^- and K^+ nucleon cross sections would suggest that the K^0 and $\overline{K}^0$ mesons will interact differently by isospin symmetry. The different interaction probability for K^0 and $\overline{K}^0$ mesons will in turn affect the decay rate asymmetry measurement. A correction for this effect should therefore be applied.

The decay rate asymmetry is defined to be

$$A = \frac{\Gamma\left(\tau^+ \to \pi^+ K^0 \left(\geq 0\pi^0\right) \nu_\tau\right) - \Gamma\left(\tau^- \to \pi^- \overline{K}^0 \left(\geq 0\pi^0\right) \nu_\tau\right)}{\Gamma\left(\tau^+ \to \pi^+ K^0 \left(\geq 0\pi^0\right) \nu_\tau\right) + \Gamma\left(\tau^- \to \pi^- \overline{K}^0 \left(\geq 0\pi^0\right) \nu_\tau\right)} = \frac{\Gamma_+ - \Gamma_-}{\Gamma_+ + \Gamma_-} \tag{E.1}$$

where we define $\Gamma_+ = \Gamma(\tau^+ \to \pi^+ K^0 \left(\geq 0\pi^0\right) \nu_\tau)$ and $\Gamma_- = \Gamma(\tau^- \to \pi^- \overline{K}^0 \left(\geq 0\pi^0\right) \nu_\tau)$. If we define the probability of a K^0 or a $\overline{K}^0$ meson interacting in the material of the detector to be P_{K^0} and $P_{\overline{K}^0}$, respectively, then the measured asymmetry can be written as

$$A_M = \frac{\Gamma_+(1 - P_{K^0}) - \Gamma_-(1 - P_{\overline{K}^0})}{\Gamma_+(1 - P_{K^0}) + \Gamma_-(1 - P_{\overline{K}^0})} \sim \frac{\Gamma_+ - \Gamma_-}{\Gamma_+ + \Gamma_-} - \frac{\Gamma_+ P_{K^0} - \Gamma_- P_{\overline{K}^0}}{\Gamma_+ + \Gamma_-} \tag{E.2}$$

where we use the fact that the the values of P_{K^0} and $P_{\overline{K}^0}$ are small (less than 0.01) so that we can ignore their impact in the denominator of the asymmetry given above.

The ratios $\Gamma_\pm/(\Gamma_+ + \Gamma_-) \approx 1/2$, so this allows one to rewrite the measured asymmetry

as

$$A_M = \frac{\Gamma_+ - \Gamma_-}{\Gamma_+ + \Gamma_-} + \frac{P_{\overline{K}^0} - P_{K^0}}{2} = A + A_D \tag{E.3}$$

where the asymmetry correction, or the dilution, is denoted as $A_D = (P_{\overline{K}^0} - P_{K^0})/2$ following the convention in the Ko paper. As a result we need to subtract the correction from the measured asymmetry to get the asymmetry we can compare with the SM prediction.

To estimate the probability of a K^0 or $\overline{K}^0$ meson interacting in the detector, we use a list of the materials in the detector and the relevant cross sections. Table E.1 outlines the materials used in the beampipe and the vertex detector of *BABAR*.

The K^0 ($\overline{K}^0$) nucleon cross section is assumed to correspond to the K^- (K^+) nucleon cross section by isospin invariance. One can take the analogy in the pion sector, where:

$$\sigma\left(\pi^+ p\right) = \sigma\left(\pi^- n\right)$$

while recognizing that:

$$\begin{pmatrix} K^+ \\ K^0 \end{pmatrix} \quad \text{and} \quad \begin{pmatrix} \overline{K}^0 \\ K^- \end{pmatrix}$$

form two doublets in the isospin space. Consequently, one can obtain the following relations:

$$\begin{aligned} \sigma\left(K^+ p\right) &= \sigma\left(K^0 n\right) \\ \sigma\left(K^- n\right) &= \sigma\left(\overline{K}^0 p\right) \\ \sigma\left(K^+ n\right) &= \sigma\left(K^0 p\right) \\ \sigma\left(K^- p\right) &= \sigma\left(\overline{K}^0 n\right) \end{aligned}$$

The cross sections are taken from the PDG [1] and shown in Fig. E.1. We reduce the cross section data to 20 bins in the neutral kaon momentum between 0 and 8 GeV (the momentum of the neutral kaons in this work is plotted in Fig. E.2). The systematic errors on the cross sections are estimated to be 0, 5%, 5% and 20% for the (K^- p), (K^- n), (K^+ p) and (K^+ n) cross sections [1], respectively.

The probability of a neutral kaon interacting with the material per unit thickness is given

Component	Radius (cm)	Material	Thickness (cm)	Z	A	Density ($g/\,\mathrm{cm}^3$)	$dN_p/dS(\times 10^{22})$	$dN_n/dS(\times 10^{22})$
Beampipe	2.5056	Au	0.0004	79	197	19.3	0.186	0.278
	2.506	Be	0.083	4	9	1.848	4.11	5.13
	2.589	Water	0.148	10	18	1.000	4.95	3.96
	2.737	Be	0.053	4	9	1.848	4.11	5.13
SVT	3.3							
	4.0							
	5.9	Si	0.03	14	28	2.33	2.10	2.10
	12.2							
	14.2							

Table E.1: Configurations of *BABAR* beampipe and vertex detector .

by

$$p_{K^0} = \sigma(K^0 p)\frac{dN_p}{dS} + \sigma(K^0 n)\frac{dN_n}{dS} \quad \text{(E.4)}$$

$$p_{\overline{K}^0} = \sigma(\overline{K}^0 p)\frac{dN_p}{dS} + \sigma(\overline{K}^0 n)\frac{dN_n}{dS} \quad \text{(E.5)}$$

where $\frac{dN_p}{dS}$ and $\frac{dN_n}{dS}$ are the number of protons and neutrons per unit area in the detector element. They can be calculated as follows:

$$\frac{dN_p}{dS} = \frac{\rho Z N_A}{M} \quad \text{(E.6)}$$

$$\frac{dN_n}{dS} = \left(\frac{A-Z}{Z}\right)\frac{dN_p}{dS} \quad \text{(E.7)}$$

where ρ is the density, Z is the atomic number, N_A is Avogadro's number, and M is the molar mass.

As pointed out by Ko et al [37], one must also take into account the time evolution of the neutral kaon which includes both the lifetime and mixing (The mixing is a relatively minor effect and could be ignored [$\Delta m = 0$] in the calculation of the dilution). For example,

$$\left|\left\langle \overline{K}^0 | K^0(t)\right\rangle\right|^2 = \left|\frac{q}{p}\right|^2 \left[\frac{1}{4}e^{-\frac{t}{\tau_S}} + \frac{1}{4}e^{-\frac{t}{\tau_L}} - \frac{1}{2}e^{-\frac{1}{2}(\frac{1}{\tau_S}+\frac{1}{\tau_L})t}\cos(t\Delta m)\right] \quad \text{(E.8)}$$

$$\left|\left\langle K^0 | K^0(t)\right\rangle\right|^2 = \left[\frac{1}{4}e^{-\frac{t}{\tau_S}} + \frac{1}{4}e^{-\frac{t}{\tau_L}} + \frac{1}{2}e^{-\frac{1}{2}(\frac{1}{\tau_S}+\frac{1}{\tau_L})t}\cos(t\Delta m)\right] \quad \text{(E.9)}$$

with

$$\left|\left\langle \overline{K}^0 | \overline{K}^0(t)\right\rangle\right|^2 = \left|\left\langle K^0 | K^0(t)\right\rangle\right|^2 \quad \text{(E.10)}$$

$$\left|\frac{q}{p}\right|^4 \left|\left\langle K^0 | \overline{K}^0(t)\right\rangle\right|^2 = \left|\left\langle \overline{K}^0 | K^0(t)\right\rangle\right|^2 \quad \text{(E.11)}$$

where τ_S and τ_L are the lifetimes of the K_S^0 and K_L^0, $\Delta m = m_L - m_S$. We use $1 - |q/p| = 3.3 \times 10^{-3}$ [1]. However, since the K_L^0 leaves the detector without decaying, one can take $\tau_L \to \infty$ in the above expression. Furthermore, the K_S^0 lifetime is already contained in the event information. One should then neglect the K_S^0 lifetime in determining the mixing. The

expressions then reduce to[1]:

$$\left|\left\langle \overline{K}^0 | K^0(t)\right\rangle\right|^2 \sim \left|\frac{q}{p}\right|^2 \left[\frac{1}{2}\left(1-\cos(\Delta m t)\right)\right] \quad \text{(E.12)}$$

$$\left|\left\langle K^0 | K^0(t)\right\rangle\right|^2 \sim \frac{1}{2}\left(1+\cos(\Delta m t)\right) \quad \text{(E.13)}$$

The probability for an interaction is given by

$$P_{\overline{K}^0} = \int_0^{t_0} p_{K^0} \left|\left\langle K^0 | \overline{K}^0(t)\right\rangle\right|^2 v dt + \int_0^{t_0} p_{\overline{K}^0} \left|\left\langle \overline{K}^0 | \overline{K}^0(t)\right\rangle\right|^2 v dt \quad \text{(E.14)}$$

$$P_{K^0} = \int_0^{t_0} p_{K^0} \left|\left\langle K^0 | K^0(t)\right\rangle\right|^2 v dt + \int_0^{t_0} p_{\overline{K}^0} \left|\left\langle \overline{K}^0 | K^0(t)\right\rangle\right|^2 v dt \quad \text{(E.15)}$$

where p_{K^0} and $p_{\overline{K}^0}$ are functions of t as the particle traverses different components of the detector. Velocity v of the neutral kaon can be calculated from its momentum. The probability of interaction is zero if the neutral kaon decays before reaching the first layer of the beampipe. The integration is carried out over the time of flight of the neutral kaon before it decays.

We determine the asymmetry correction (A_D) on an event-by-event basis. We calculate the probability of an event interacting with the detector material before the K^0_S decays using the momentum, cosine of the polar angle in the laboratory frame, and the decay length of the K^0_S meson. The K^0_S decay length in the transverse plane of the detector is shown in Fig. E.3, and the $cos(\theta)$ of the K^0_S in the laboratory frame is shown in Fig. E.4. The probabilities are averaged for each τ lepton charge to obtain a final estimation of A_D. A_D is found to be $(0.135 \pm 0.013)\%$ and $(0.137 \pm 0.015)\%$ for the e- and μ-tag, respectively, where the errors are statistical only. In Fig. E.5 we present A_D as a function of the laboratory momentum of the K^0_S meson for the e-tag and μ-tag samples.

To estimate the systematic uncertainty in A_D, we vary individually the cross sections by their corresponding systematic errors. The deviations resulted from the variation in each cross section are added together in quadrature. As a result, the systematic uncertainty for the e-tag sample is 0.026% whereas for the μ-tag sample it is 0.017%. To verify how rigorously isospin invariance holds in our signal decay, we refer to the cross sections for $e^+e^- \to \pi^+\pi^-$ and $\tau^- \to \pi^-\pi^0\nu_\tau$. The difference in the two cross sections is a consequence

[1]Natural units are adopted throughout this chapter, where $c = \hbar = 1$.

Changes to the sample	A_D
e-tag	
Nominal result	(0.135±0.013)%
Increasing the momentum of K^0_S by 10%	(0.126±0.013)%
Decreasing the decay radius of K^0_S by 1 cm	(0.116±0.012)%
Decreasing the decay radius of K^0_S by 2 cm	(0.101±0.011)%
Changing K^0 into $\overline{K}^0$ and vice versa	(0.136±0.013)%
μ-tag	
Nominal result	(0.137±0.015)%

Table E.2: Effects of changes to the K^0_S kinematics on A_D. Errors are statistical only.

of broken symmetry in isospin. The discrepancy is observed to be less than 5%, which is well within the errors in the cross sections we have assigned above.

A series of cross-checks of the dilution factor has also been performed to ensure that the results for A_D are reasonable:

1. A_D for e-tag and μ-tag are the same, which is expected because the results should only depend on the neutral kaon on the signal side.

2. Furthermore, a reduction of the decay radius is observed to result in a reduction in the asymmetry (A_D). This is expected, as the decrease of the decay radius will mean that the neutral kaon is less likely to pass through all layers of material in the detector. Less layers trasversed by the particle means less interactions and hence a smaller A_D because it is the nuclear interaction corss section that generates A_D.

3. The momentum is also increased by 10% in order to study the dependence of A_D on the momentum of the kaon. As expected, A_D decreases as momentum increases.

4. Flipping the flavour of the neutral kaon in the decay (i.e. changing a K^0 in a decay into a $\overline{K}^0$ and vice versa) is not expected to result in any changes in A_D, as the momentum and angular distributions of the K^0_S for τ^+ and τ^- decays are expected to be the same.

Table E.2 presents the values of A_D with respect to each of the cross-checks.

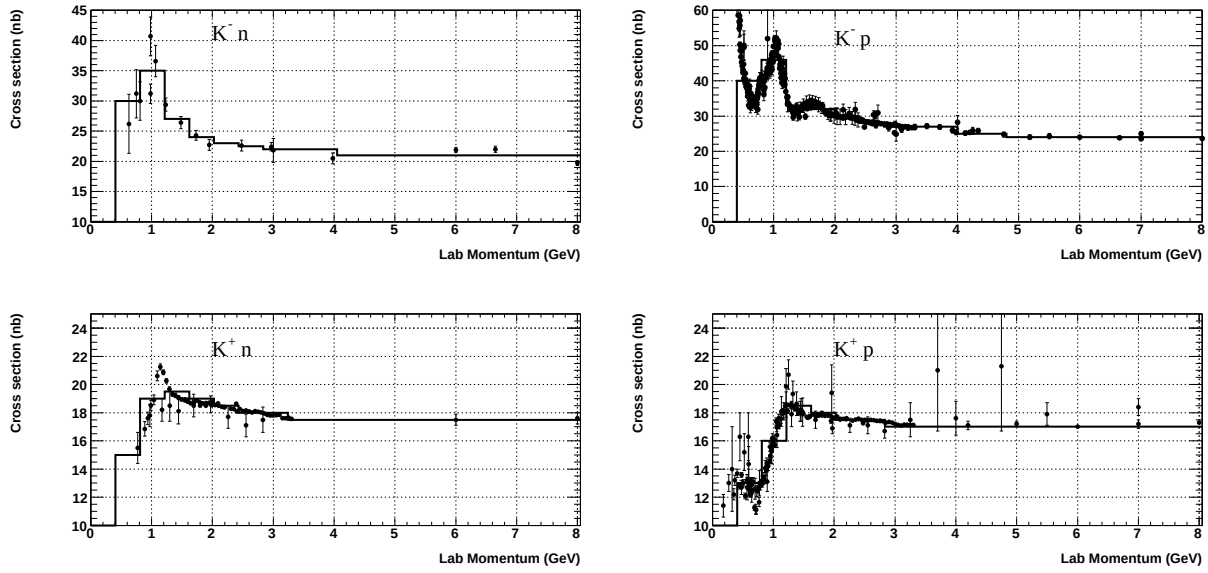

Figure E.1: The K^- and K^+ nucleon total cross sections reproduced from [1]. The lines are the representation of the cross section in bins of 0.4 MeV/c^2.

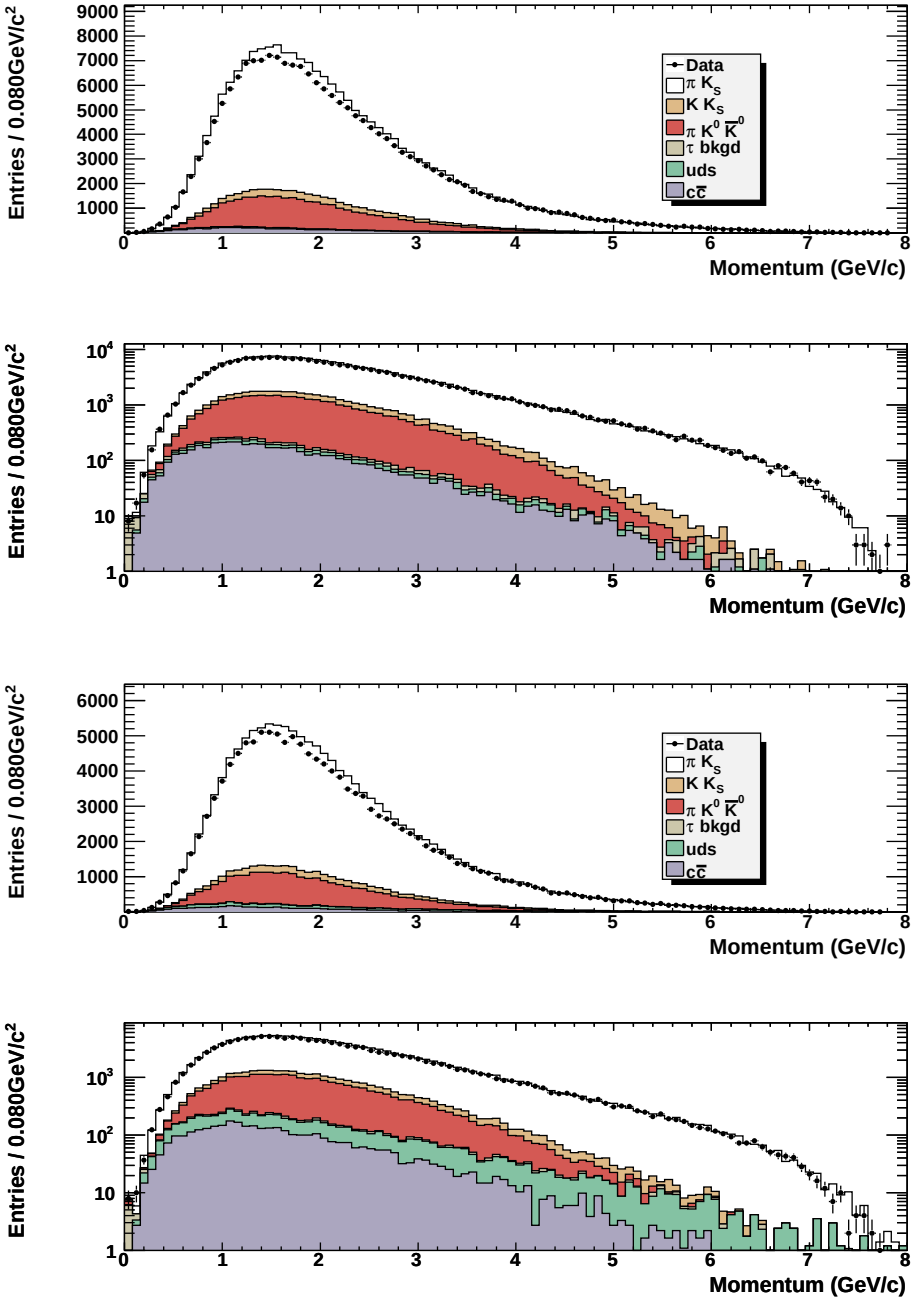

Figure E.2: K_s^0 momentum distributions for e-tag (top) and μ-tag (bottom).

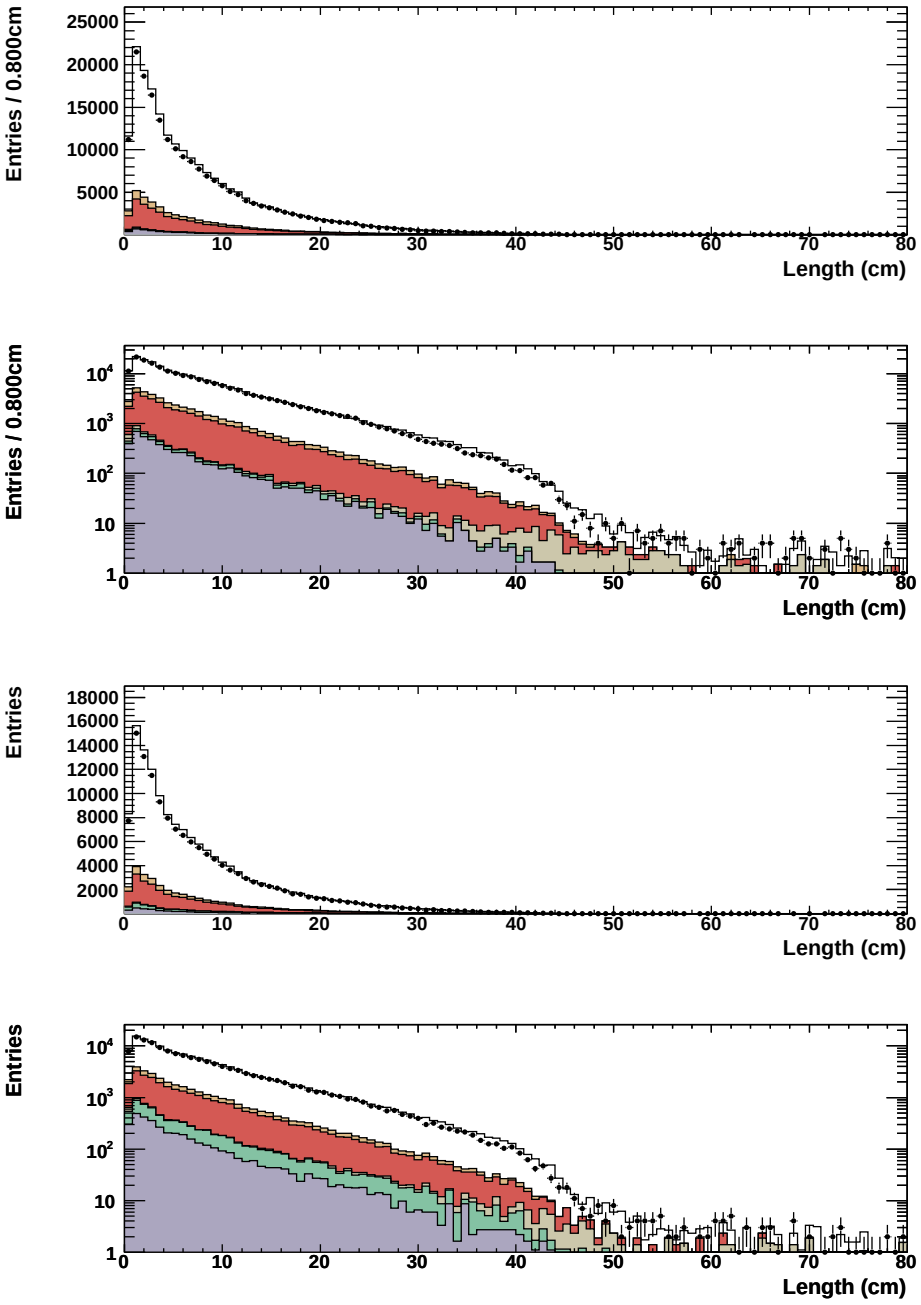

Figure E.3: Distribution of the component of the K_S^0 decay length in the transverse plane for e-tag (top) and μ-tag (bottom).

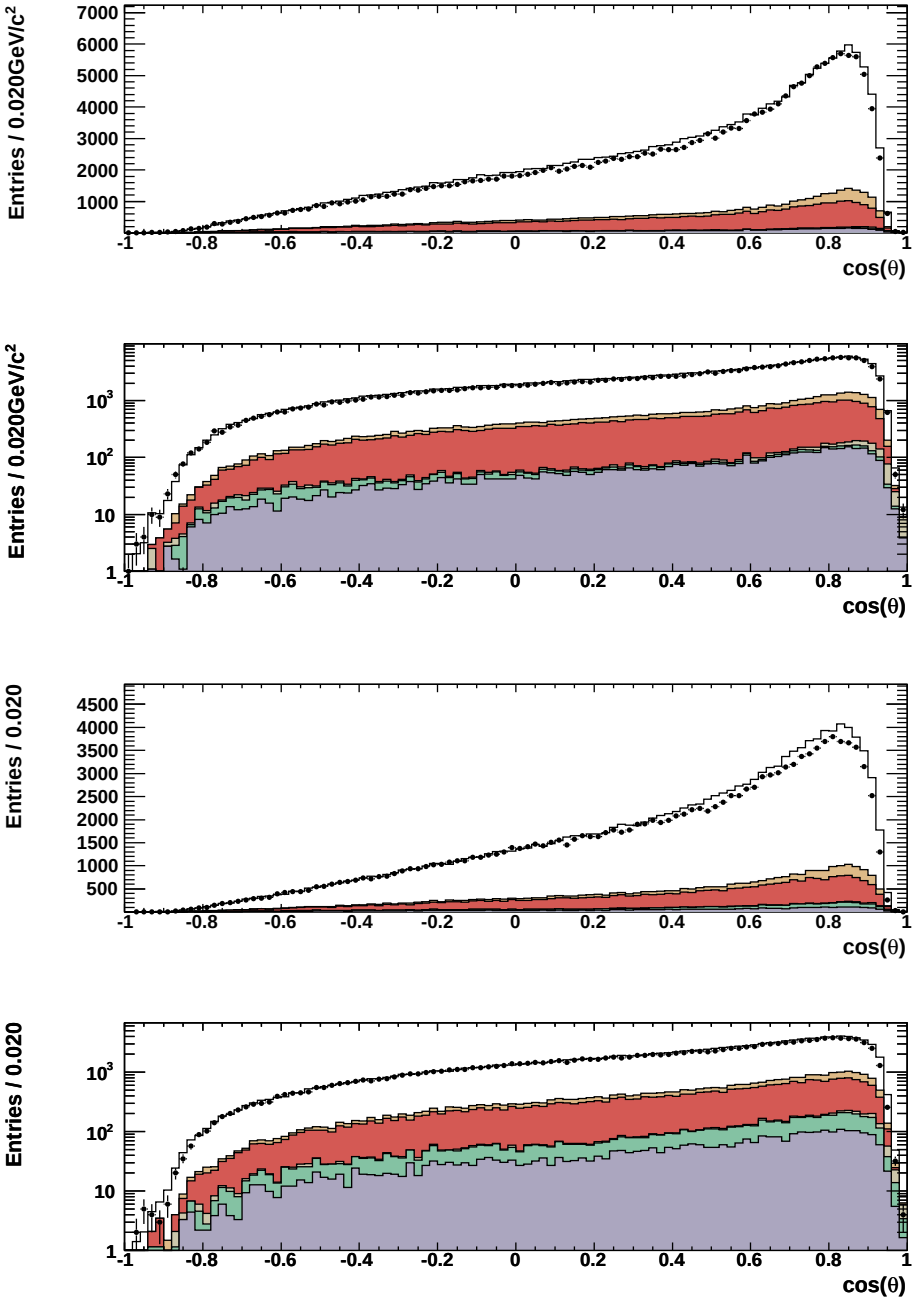

Figure E.4: Distribution of $cos(\theta)$ of the K_S^0 for e-tag (top) and μ-tag (bottom).

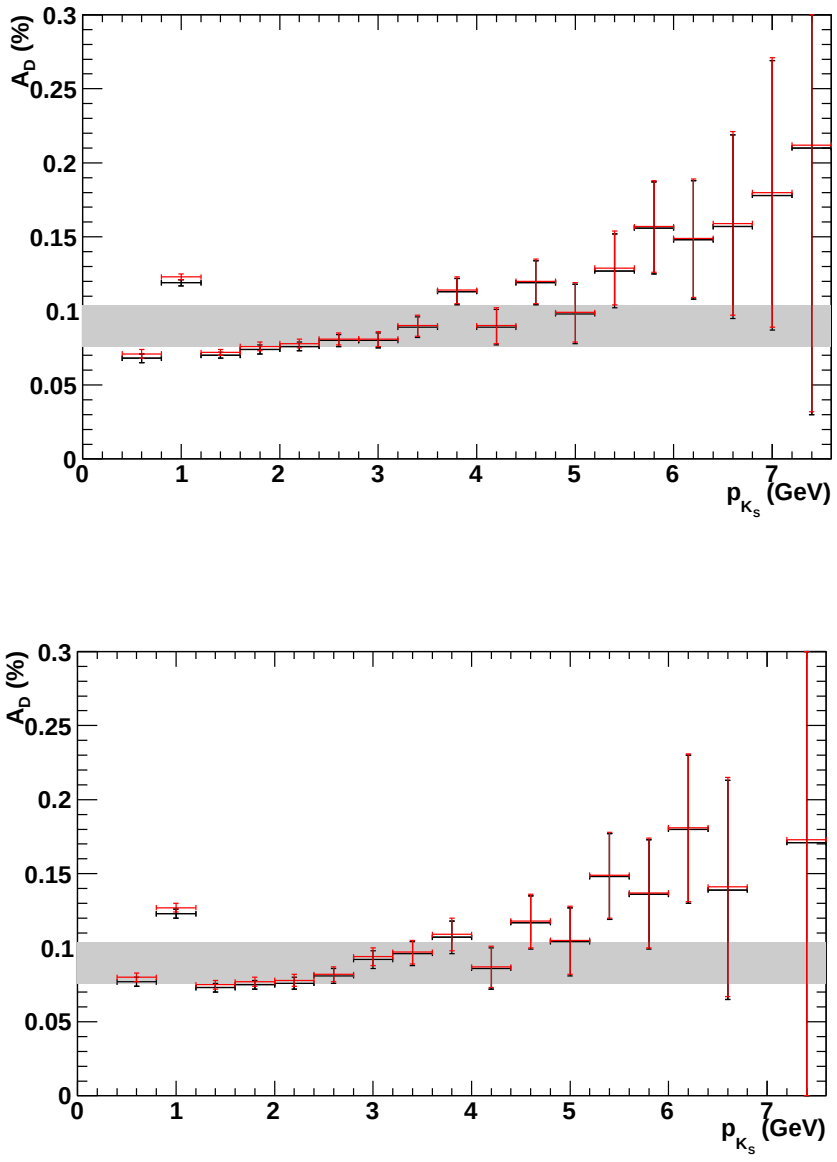

Figure E.5: The asymmetry correction factor A_D as a function of the laboratory momentum of the K^0_S meson in the e-tag (top) and μ-tag (bottom) samples. The black points represent A_D calculated with no assumption whereas the red points represent A_D calculated with the assumption that there is no oscillation. The gray band indicates the overall asymmetry correction factor, with the thickness representing the statistical uncertainty.

Bibliography

[1] K. Nakamura et al., *(Review of Particle Properties) J. Phys. G* **37**, 075021 (2010).

[2] J. A. Peacock, *Cosmological Physics*, Cambridge University Press, 1999.

[3] A. D. Sakharov, *Soviet Physics Uspekhi* **34**, 392 (1991).

[4] K. Kleinknecht, *Uncovering CP Violation: Experimental Clarification in the Neutral K Meson and B Meson Systems*, Springer, 2003.

[5] S. Barr et al., *Phys. Rev. D* **20**, 10 (1979).

[6] C. Massa, *Astr. Space Sci.* **286**, 313 (2003).

[7] Y. Fukuda et al., *Phys. Rev. Lett.* **81**, 1158 (1998).

[8] Q. R. Ahmad et al., *Phys. Rev. Lett.* **87**, 071301 (2001).

[9] H. P. Nilles, *Phys. Rep.* **110**, 1 (1984).

[10] H. E. Haber and G. L. Kane, *Phys. Rep.* **117**, 75 (1985).

[11] C.-S. Huang, T. Li, L. Wei, and Q.-S. Yan, *Eur. Phys. J. C* **23**, 195 (2002).

[12] I. I. Bigi and A. I. Sanda, *Phys. Lett. B* **625**, 47 (2005).

[13] S. Glashow, *Nucl. Phys.* **22**, 579 (1961).

[14] S. Weinberg, *Phys. Rev. Lett.* **19**, 1264 (1967).

[15] A. Salam, *Rev. Mod. Phys.* **52**, 525 (1980).

[16] P. Higgs, *Phys. Rev. Lett.* **13**, 508 (1964).

[17] C. Giunti and C. W. Kim, *Fundamentals of Neutrino Physics and Astrophysics*, Oxford University Press, 2007.

[18] N. Cabibbo, *Phys. Rev. Lett.* **10**, 531 (1963).

[19] M. Kobayashi and T. Maskawa, *Prog. Theor. Phys.* **49**, 652 (1973).

[20] J. H. Christenson et al., *Phys. Rev. Lett.* **13** (1964).

[21] R. P. Feynman and M. Gell-Mann, *Phys. Rev.* **109**, 193 (1958).

[22] C. O. Dib and B. Guberina, *Phys. Lett. B* **255**, 113 (1991).

[23] V. L. Fitch et al., *Phys. Rev. Lett.* **31**, 1524 (1973).

[24] C. Geweniger et al., *Phys. Lett. B* **48**, 483 (1974).

[25] R. Piccioni et al., *Phys. Rev. Lett.* **29**, 1412 (1972).

[26] H. H. Williams et al., *Phys. Rev. Lett.* **31**, 1521 (1973).

[27] D. Kimura, K. Y. Lee, T. Morozumi, and K. Nakagawa, *arXiv:hep-ph/0905.1802v2* (2009).

[28] P. F. Harrison et al., *BABAR Physics Book*, *BABAR* Experiment, 1996.

[29] B. Aubert et al., *Nucl. Instrum. Meth. A* **479**, 1 (2002).

[30] I. Adam et al., *Nucl. Instrum. Meth. A* **538**, 281 (2005).

[31] B. F. Ward, S. Jadach, and Z. Was, *Nucl. Phys. Proc. Suppl.* **116**, 73 (2003).

[32] S. Jadach, Z. Was, R. Decker, and J. H. Kühn, *Comput. Phys. Commun.* **76**, 361 (1993).

[33] T. Sjostrand, *Comput. Phys. Commun.* **82**, 74 (1994).

[34] E. Barberio and Z. Was, *Comput. Phys. Commun.* **79**, 291 (1994).

[35] S. Brandt, C. Peyrou, R. Sosnowski, and A. Wroblewski, *Phys. Lett.* **12**, 57 (1964).

[36] E. Farhi, *Phys. Rev. Lett.* **39**, 1587 (1977).

[37] B. R. Ko, E. Won, B. Golob, and P. Pakhlov, *arXiv:hep-ex/1006.1938v1* (2010).

[38] K. Kiers et al., *Phys. Rev. D* **78**, 113008 (2008).

[39] A. Datta et al., *Phys. Rev. D* **75**, 074007 (2007).

[40] L. Lyons, *Statistics for nuclear and particle physicists*, Cambridge University Press, 1992.

[41] M. Bischofberger et al., *BELLE Preprint* **2010-27** (2010).

[42] G. Bonvicini et al., *Phys. Rev. Lett.* **88**, 111803 (2002).

[43] P. del Amo Sanchez et al., *Phys. Rev. D* **83**, 071103 (2011).

[44] J. M. Roney, *Nucl. Phys. B (Proc. Suppl.)* **169**, 379 (2007).

[45] A. Khan, K. Schofield, and D. Wright, *IEEE Nuclear Science Symposium Conference Record* (2005).

[46] T. G. Dietterich and G. Bakiri, *JAIR* **2**, 263 (1995).

[47] B. Aubert et al., *Phys. Rev. Lett.* **99**, 021603 (2007).